Internal Annular Flow Condensation and Flow Boiling: Context, Results, and Recommendations

51

Amitabh Narain, Hrishikesh Prasad Ranga Prasad, and Aliihsan Koca

Contents

A. Narain (✉) · H. P. Ranga Prasad · A. Koca
Michigan Technological University, Houghton, MI, USA
e-mail: narain@mtu.edu; hrangapr@mtu.edu; akoca@mtu.edu

F. A. Kulacki (ed.), *Handbook of Thermal Science and Engineering*,
https://doi.org/10.1007/978-3-319-26695-4_51

Abstract

This chapter reviews in-tube boiling and condensing flows, a subset of the area of phase-change heat transfer, with emphasis on their annular regime realizations in innovative devices. This review, in the light of numerous and excellent existing books and reviews, is also relevant because of recently reported experimental and technological approaches that make it feasible for annular/stratified regimes to cover the entire lengths of millimeter-scale flow-boilers and flow-condensers. The review chapter's content also relates to new ways of addressing challenges that have emerged in the area of high heat-flux (500–1000 W/cm^2 or greater) cooling of data centers, super computers, laser weapons, and other devices. The chapter summarizes current knowledge base and provides a design example each for steady annular operations of flow-boilers and flow-condensers. Furthermore, the chapter deals with some recent breakthroughs in the simulation of annular boiling/condensing flows and how such approaches can be extended – in conjunction with well-planned and parallel experiments – to further develop the science and innovative applications associated with steady or pulsatile operations of annular flow-boilers and flow-condensers.

Nomenclature

A	Cross-sectional area (m^2)
Bl	Boiling number $\left(\overline{q}_w^{''}/Gh_{fg}\right)$
$\widetilde{Bl}$	Alternate boiling number $\left(q_w^{''}\cdot D_h/\left(\mu_L\cdot h_{fg}\right)\right)$
Bo	Bond number $(g(\rho_L - \rho_V)D^2/\sigma)$
C	Lockhart-Martinelli constant
C_p	Specific heat (J/kg-K)
CHF	Critical heat-flux
D_h	Hydraulic diameter (m)
f	Friction factor
fr_P	Heated perimeter fraction (P_H/P_F)
Fr_x	Froude number in x-direction $(\lvert g_x\rvert\ D_h/U^2)$
Fr_y	Froude number in y-direction $(\lvert g_y\rvert\ D_h/U^2)$
G	Mass flux (kg/m^{2}s)
g_x	Gravity component in x-direction (m/s^2)
g_y	Gravity component in y-direction (m/s^2)
h	Height of the channel (m)
h_{fg}	Heat of vaporization (J/kg)

Ja	Liquid Jakob number ($C_{pL}\Delta T/h_{fg}$)
k	Conductivity (W/m-K)
L	Length of the channel or test section (m)
$\dot{M}_{in}$	Total mass flow rate (kg/m^2-s)
$\dot{M}_L$	Liquid mass flow rate (kg/m^2-s)
$\dot{M}_v$	Vapor mass flow rate (kg/m^2-s)
p_0 or p_{in}	Steady inlet pressure (also p_{in}) (kPa)
P	Mechanical power (W)
Pr_L	Liquid Prandtl number ($\mu_L C_{pL}/k_L$)
$\overline{q}''_w$	Mean wall heat-flux (W/m^2)
Re_T	Reynolds number representing nondimensional (GD_h/μ_V)
S	Suppression factor
Su	Suratman number ($\sigma\rho_V D_h/\mu_V^2$)
t	Time
$\overline{T}_w$	Mean wall temperature (°C)
$T_{sat}(p_0)$	Saturation temperature at pressure p_0 (°C)
u	Velocity (m/s)
We	Liquid Weber number ($\rho_L U^2 D_h/\sigma$)
X	Vapor quality
$\hat{x}$	Nondimensional distance ($\equiv x/D_h$)
x_A	Nondimensional length of the annular regime
X_{tt}	Lockhart-Martinelli parameter

Greek Symbols

μ	Viscosity (kg/m-s)
ρ	Density (kg/m^3)
ϵ	Void fraction
Φ_g	Two-phase multiplier
σ	Surface tension (kg/s^2)
Δ	Physical value of liquid film thickness (m)
Ψ_q	Nondimensional heat-flux
θ_w	Nondimensional temperature

Subscripts

cb	Represents macroscale convective boiling
CHF1	Represents dry-out instability
CHF2	Represents inverted annular flow related instability
cr	Represents "critical value"
L	Represents liquid phase of the flow variable
nb	Represents macro-scale nucleate boiling
V	Represents vapor phase of the flow variable

1 Introduction

In-tube boiling and condensing flows have been a subject of scientific studies – involving experiments, modeling, computations, and analysis – since the early 1900s. As engineering support for boiler and condenser operations in macroscale applications (as in power generations sector, heating ventilation and air conditioning refrigeration, waste heat recovery, steam generation, etc.) has matured, new challenges have emerged in the area of high heat-flux (500–1000 W/cm^2 or greater) cooling for data center, super computers, laser weapons, and other devices. One of these challenges is smallness of available space for device cooling (that must employ flow-boilers) and occasionally also for heat rejection (for devices that must employ flow-condensers). The space restrictions and low pumping power needs often limit hydraulic diameter D_h of the boiler/condenser tubes to be small but not too small (e.g., 100 μm $\leq D_h \leq$ 8 mm), whereas safety and cost-effectiveness issues restrict pure fluids to available refrigerants and/or water. This review is focused on the millimeter-scale hydraulic diameter applications. However, there remains a need for high heat-flux boiling in microscale tubes (hydraulic diameter less than 100 μm) as well – and active research in this area is going on (see, e.g., Kuo and Peles 2009; Li et al. 2017; Zhu et al. 2016).

Another challenge is a restriction on allowed boiling surface and/or condensing surface temperatures. For example, typically, 75–85 °C is the maximum allowed temperature for the boiler tube surfaces connected to cold plates used in electronic cooling (Kandlikar and Hayner 2009; also see ▶ Chap. 49, "Single- and Multiphase Flow for Electronic Cooling"). Besides high heat removal capabilities at high heat-fluxes, there are demands on effectiveness of such millimeter-scale boilers and condensers. For example, effectiveness often requires low pumping power consumption through manageable pressure-drops, and, in case of high heat-flux flow-boilers, it may also mean an ability to recover large amounts of mechanical power available (associated with higher exiting vapor speeds from mm-scale ducts) at the exit.

Often effectiveness also requires avoidance of vapor compressibility-related choking effects (Ghiaasiaan 2007), and this, in turn, may require modest mass fluxes (G) in tubes of modest hydraulic diameters ($D_h \equiv 4A/P$, where A and P, respectively, represent the cross-sectional area and perimeter of the tube). Based on available experimental studies and experiences, modest G (~100 $\leq$ G $\leq$ 500 kg/m^2.s) means avoiding high G (>500 kg/m^2 s) and modest D_h (~100 μm $\leq D_h \leq$ 8 mm) means tube diameters that are neither too small (e.g., $D_h \leq$ 100 μm) nor too large (e.g., $D_h \geq$ 8 mm). The microscale tubes have surface tension and/or contact line phenomena present most everywhere in the flow – and significant flow rates at acceptable pumping power needed for high heat-flux operations are not available, and, therefore, such operations require innovation. On the other hand, flow boiling in very large macroscale tubes has significant surface-tension effects only in certain nucleate boiling and bubbly flow-regimes, which is only at small volumetric gas fractions or low qualities. Furthermore, contact-line flow physics cannot be beneficially utilized outside nucleate flow-boiling regime, as they appear to be advantageous only at certain nucleation sites through their impact on bubble

dynamics (contact angle, pool-boiling heat transfer coefficient, etc.). This would mean, according to some popular naming conventions (Ghiaasiaan 2007; Kandlikar and Grande 2003; Mehendale et al. 2000), that effectiveness of high heat-flux flow-boiling operations may restrict one to mini-channels (~100 μm $\leq D_h \leq$ 1 mm) and a subset of macro-channels (~1 mm $\leq D_h \leq$ 8 mm) – excluding micro-channels (~10 μm $\leq D_h \leq$ 100 μm) as well as very large diameter ($D_h \geq$ 8 mm) macro-channels.

Unfortunately, established technologies such as an array of small diameter heat pipes or their capillary and looped heat pipe variations (Faghri 1995) are not the appropriate solutions for the increasing high heat-flux and heat-load needs of the electronic cooling applications (Agostini et al. 2007; Ball 2012; also see ▶ Chap. 52, "Heat Pipes and Thermosyphons"). This is because, for these applications, *direct use* of heat pipes does not work well due to limitations arising from necessarily large vapor speeds that are involved (sonic limits), wicking limits, and the need for large distances between boilers and condensers.

In the above context, this review chapter dealing with millimeter-scale boilers and condensers becomes relevant because of recently reported experimental and technological approaches that make it feasible for high heat-flux annular/stratified regimes to cover the entire device lengths. Necessarily, in the light of numerous and excellent existing books and reviews (Bergles 1988; Carey 1992; Collier and Thome 1994; Dhir 1998; Ghiaasiaan 2007; Manglik 2006; etc.) that partially cover this focus area, the chapter benefits from synthesis of insights and knowledge that already exist.

Innovative and effective steady operations (Kivisalu et al. 2014) may also require a change from *traditional* flow-boiler and flow-condenser operations – associated with multiple flow-regimes (see, e.g., Figs. 1 and 2 for depiction of different flow-regimes in a horizontal duct and Carey (1992) and Ghiaasiaan (2007) for discussions on the different flow-regimes) – to operations such as the ones in Fig. 3a, b. These operations control the flow-regimes through control of inlet quality and attain *stable* and steady annular flow-regime over all of a suitably chosen device length. Furthermore, to address high heat-flux needs (500–1000 W/cm^2 or greater), as discussed near the end of this review, resonant pulsations in the liquid and vapor flows may be introduced to create vapor acoustic-enabled *large amplitude* standing waves on the interface of the highly stabilized thin liquid film (300–200 μm thickness range) flow boiling in the annular regime. Such flows are realized through flow controls and one of several pulsation input options indicated in Fig. 3a, b. This is to make liquid film flow as choppy (i.e., up, down, and forward motions) as possible – within the feasibility offered by laminar flow restrictions imposed by the thinness of the liquid film flow (300–200 μm thickness range) on a wetting wall. The choppiness helps in introducing additional micro-convection advantages to evaporation at the interface as well as, particularly at higher heat-flux values, in increasing the level of contributions from microscale nucleate boiling. Both micro-convection and microscale nucleate boiling, consisting of micron to submicron diameter bubbles, take advantage of high heat-flux contact-line flow physics known to play a pivotal role in macroscale pool boiling during an ebullition cycle. The size limitations on the nucleating bubbles are imposed by liquid film thickness and accompanying significant reductions in *inertial pinning forces* (see Dhillon and Buongiorno

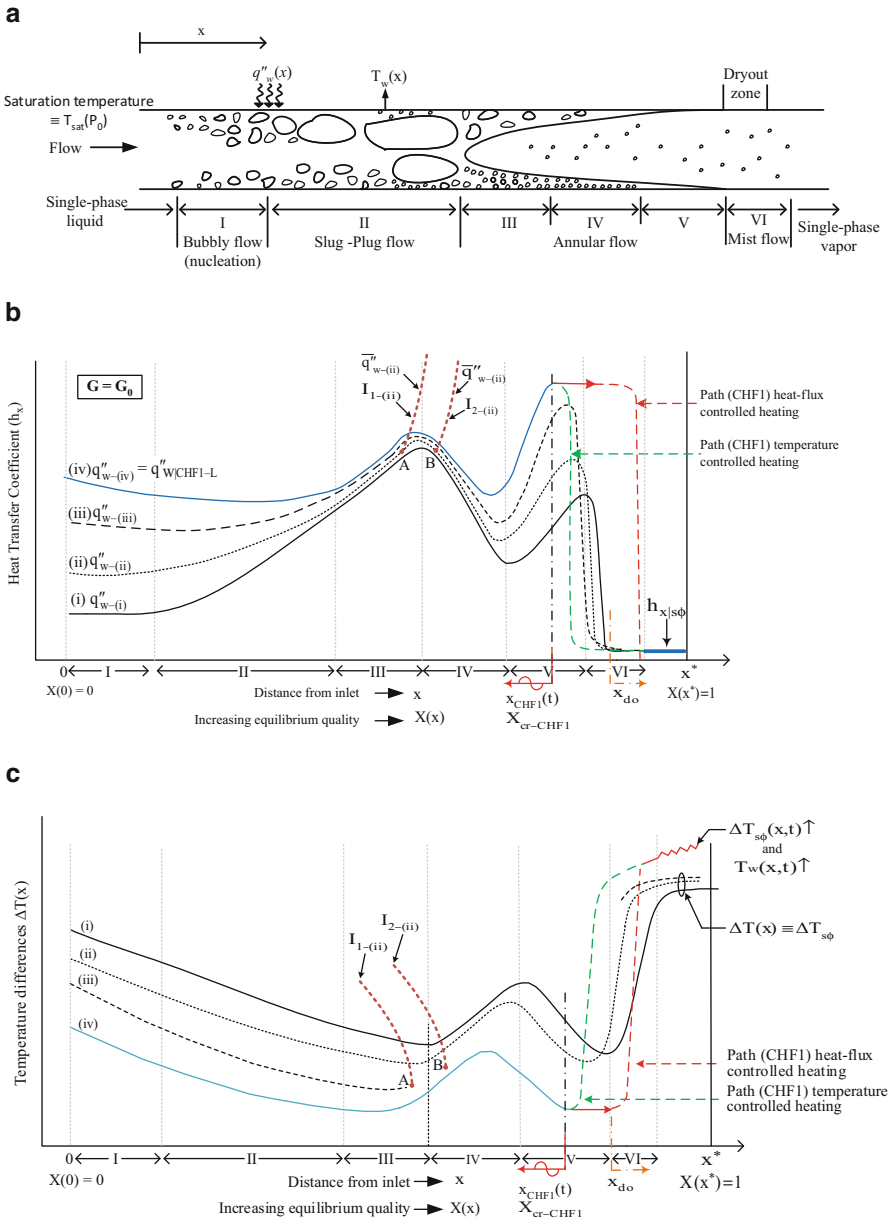

Fig. 1 **(a)** Typical flow-regimes encountered in traditional operations dealing with saturated flow boiling (with saturation conditions at $x = 0$) in a horizontal tube. The sequence of regimes is for cases where the average heat-flux $\bar{q}''_w$ for a given mass-flux G is below a certain threshold. **(b)** For a certain $G = G_0$ value, the expected qualitative variation in local values of heat transfer coefficient h_x with distance $0 \le x \le L$ and quality $0 \le X(x) \le 1$ is shown as curves (i)–(iv), for increasing values of uniform heat-flux prescriptions. In addition, for a representative heating curve (i), the flow

2017; Phan et al. 2009; Zeng et al. 1993a, b, etc., for meaning of inertial pinning forces) present in pool boiling. In Fig. 1b, c, at locations A and B of a representative steady operation curve (ii), the depicted curves $I_{1-(ii)}$ and $I_{2-(ii)}$ represent the expected benefits associated with the wavy annular innovative flow-boiling operations just mentioned (with further discussions in Sect. 6). For related and additional discussions on pool-boiling contact-line flow physics, see Gerardi et al. (2010), Kunkelmann et al. (2012), McHale and Garimella (2010), and Raghupathi and Kandlikar (2016) and ▶ Chap. 41, "Nucleate Pool Boiling".

One way to achieve (see Kivisalu 2015; Kivisalu et al. 2014) the aforementioned and beneficial wavy (large amplitude standing waves) annular flow realizations is by imposing pulsations in the incoming vapor (and liquid, if needed) streams (Fig. 3a).

By traditional saturated boiling operations of flow-boilers (Fig. 1), it is meant here that a flow-boiler sees an all liquid flow at the inlet with the inlet temperature close to saturation temperature (i.e., only a slight subcooling). Depending on whether imposed heat-flux relative to mass flux is below or above a certain threshold (discussed in Sect. 2), the traditional flow-boiling regimes may evolve as in Fig. 1a or result in inverted annular flows as discussed in Sect. 2. These inverted annular regimes are also commonly found in subcooled flow boiling as noted in Collier and Thome (1994), Lee and Mudawar (2009), and Tibiriçá et al. (2012). Similarly, a traditional flow-condenser (Fig. 2) sees an all vapor flow at the inlet with the inlet temperature close to saturation temperature (i.e., only a slight super heating).

For the saturated flow-boiling realizations in Fig. 1, the increasing distance or quality from the inlet is marked on the horizontal axis, as zones I–VI. The zone boundaries in Fig. 1b, c are for a representative heating level associated with curve (i), which change a little with increasing heating levels. The marked zones, respectively, denote the following flow-regimes: macroscale nucleate boiling (I), where bubble sizes are determined by hydraulic diameter D_h; plug-slug regime (II), associated with coalesced bubbles and microscale nucleating bubbles in the thin liquid film adjacent to the wall; annular (III) with significant contributions from increasing microscale nucleating bubble sites and frequencies that eventually plateau; annular (IV) with decreasing microscale nucleating bubble sites, sizes, and frequencies, as liquid film thickness gets below a certain threshold; convective annular boiling with suppressed nucleation (V), as liquid film thickness gets below another threshold; and regimes with near wall dry-out conditions (VI).

The near inlet downstream flow-regime (I) in Fig. 1a consists of millimeter-scale (tube diameter controlled) bubbles in the nucleate boiling flow-regime – whose heat-flux-dependent h_x values in Fig. 1b perhaps arise from increasing number of active

Fig. 1 (continued) traverses multiple flow-regimes I–VI. Curve (iv) corresponds to the approach of a dry-out instability (termed CHF1 mechanism) associated lower threshold value of critical heat-flux ($q''_{w-CHF1-L}$). At this value, the dry-out location x_{CHF1} (t) becomes oscillatory – with motion biased toward upstream locations. On curve (iii), at points A and B, imposition of innovative operations discussed in the paper may lead to attainment of quasi-steady values along curves $I_{1-(ii)}$ and $I_{2-(ii)}$. **(c)** The curves (i)–(iv) in (**b**) above are plotted here as $\Delta T(x)$ versus X(x), where $\Delta T(x) \equiv |T_w(x) - T_{sat}(p_0)|$

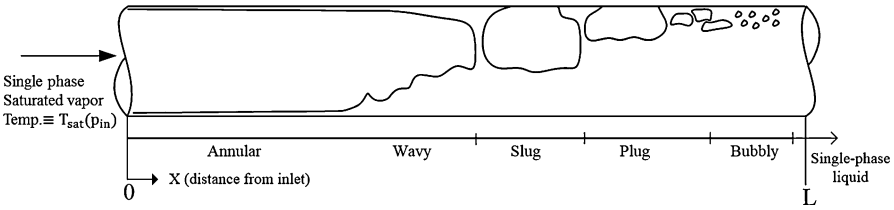

Fig. 2 Typical flow-regimes encountered in traditional operation of a horizontal flow-condenser

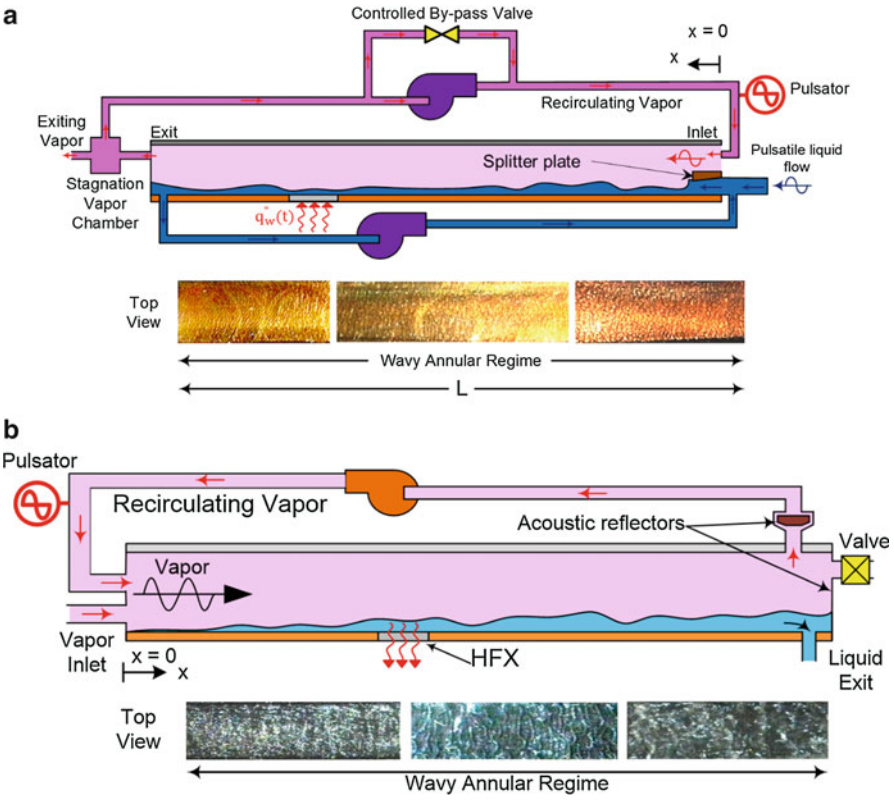

Fig. 3 **(a)** Innovative flow-boiler operations. **(b)** Innovative flow-condenser operations

nucleation sites with increasing heat-flux impositions. These macroscale nucleation contributions become weaker relative to the *convective contribution*-induced/*convective contribution*-controlled microscale nucleation in downstream zones II–III of Fig. 1b. The coalescing curves (i)–(iv) in zone III perhaps represent *convectively controlled* (by smaller liquid film thicknesses near heated walls) microscale nucleating bubbles – appearing and plateauing at saturated number of nucleation sites with

increasing frequencies. Macroscale convection defining macroscale liquid-vapor interface configurations in turn controls these smaller liquid film thicknesses near heated walls. The term *predominantly convective contributions* for zones II–III is widely used; see Chen (1966), Cooper (1989), Kenning and Cooper (1989), etc.

The available literature on macro- and microscale nucleation is not the focus of this review. Yet it is noted that some heuristic support for the above description of the role played by macro-/micro-nucleation can be obtained by superposition of convection mechanisms and available modeling for nucleating bubble mechanisms based on pool-boiling investigations. Such superposition-based simulations are available on FLUENT (2015). The phase distribution is obtained by solving continuity equations for volume fraction and Navier-Stokes equation for both the phases separately. The simulations use the Rensselaer Polytechnic Institute (RPI) nucleate boiling models as integrated by Kurul and Podowski (1991) and Lavieville et al. (2006). The RPI boiling model partitions the heat-flux from the wall into contributing mechanisms while adding information on models for bubble departure frequency (such as Cole 1960), departure diameter (such as Tolubinsky and Kostanchuk 1970), and nucleation site density (Lemmert and Chawla 1977).

The widths of the zones IV–VI in Fig. 1 are somewhat uncertain – but their presence is expected and widely acknowledged (Ranga Prasad et al. 2017; Ross and Radermacher 1987). Typical experimental data available in the literature are largely skewed in favor of zones I–III of Fig. 1 (see Kim and Mudawar 2013c; Kenning and Cooper 1989).

In the above discussions, only relevant *heterogeneous* (at heated solid surfaces) nucleate boiling mechanisms for superheated liquids have been mentioned. The fundamentals of *homogeneous* nucleate boiling mechanisms for superheated liquids are not discussed here – but they can be found elsewhere (Avedisian 1985; Forster and Zuber 1954; Plesset and Zwick 1954; Prosperetti and Plesset 1978, etc.).

The horizontal configuration flow-regimes in Figs. 1, 2, and 3 are different from flow-regimes associated with downward or upward inclined (with respect to the gravity vector) tubes (Carey 1992; Ghiaasiaan 2007). For modest to high mass-flux values of G and millimeter-scale hydraulic diameters D_h, interfacial shear and pressure gradients may dominate effects of gravity, and, therefore, even tubes at different inclinations may exhibit flow-regimes that are qualitatively close to the ones associated with the horizontal configuration (as shown in Figs. 1, 2, and 3). This is because axial and transverse gravity components g_x and g_y may become effectively negligible compared to inertia forces (see definitions of Froude numbers in Sect. 2.1).

It is also well known that there are some qualitative similarities between the boiling and condensing flow-regimes in Figs. 1, 2, and 3 and regimes that are encountered in adiabatic flows (Carey 1992; Ghiaasiaan 2007). That is, if saturated isothermal liquid and saturated isothermal vapor were flowing through an insulated duct (constituting adiabatic flows), it would typically lead to flow-regimes that exhibit uniform values of qualities X(x) (meaning the same value of X at all duct locations x) and a particular associated flow-regime. Here, $X(x) \equiv \dot{M}_V(x)/\dot{M}_{in}$, where $\dot{M}_V(x)$ represents the vapor mass flow rate and $\dot{M}_{in} \equiv \dot{M}_V(x) + \dot{M}_L(x)$ is the total mass flow rate, including the liquid mass flow rate $\dot{M}_L(x)$. It is common to compare

the flow-regime of saturated boiling/condensing flows of Figs. 1, 2, and 3 at a particular location "x," where the quality is X(x), to the flow-regime of an adiabatic flow with the same quality X (with same fluids, tube diameter D_h, and mass-flux G). This is because a qualitative similarity between the adiabatic and non-adiabatic flow-regimes is expected – provided the X(x) value is away from a *flow-regime transition boundary*. That is, flow-regime similarities between adiabatic and phase-change flows may not be good at a flow-regime transition boundary (see Sects. 2 and 3) – which is located by critical values of X, denoted as X_{cr}, and estimated with the help of experiments. This is because these boundaries represent some sort of instability of a given flow-regime, and interfacial mass flux strongly affects the stability of the flow-regimes. For example, flow-regime boundaries – relative to those obtained from adiabatic flow considerations – are expected to be particularly different for thin annular flows involving high heat-fluxes and high interfacial mass fluxes (which are zero for the adiabatic flows).

Consider low to modest mass-flux steady boiling/condensing flow-regimes in Figs. 1, 2, and 3. At a spatial location x, vapor mass flow rate quality X(x) is typically assessed as thermodynamic quality $X_{th}(x)$ (with $X_{th}(x) \cong X(x)$). The quality of $X_{th}(x)$ estimate depends on the available knowledge with regard to (i) the ability to approximately identify an $x = 0$ location where bulk mean fluid temperature is close to saturation temperature $T_{sat}(p_0)$, (ii) information on "method of heating/cooling" (i.e., whether wall heat-flux or wall temperature values are known and uniform at all "x" locations or are nonuniform in a certain known way), and (iii) the "level" of heating/cooling (which is either the average heat-flux $\overline{q}_w^{''}$ values or the average values of imposed temperature difference $\Delta T \equiv \left|\overline{T}_w - T_{sat}(p_0)\right|$). The average spatial heat-flux $\overline{q}_w^{''} \equiv \frac{1}{L}\int_0^L q_w^{''}(x).dx$ values are associated with the steady wall heat-flux $q_w^{''}(x)$ values, and the average spatial values of imposed temperature difference ΔT are associated with locally varying $\Delta T(x) \equiv |T_w(x) - T_{sat}(p_0)|$ values over $0 \le x \le L$, where $T_w(x)$ represents steady wall temperature variations, $\overline{T}_w \equiv \frac{1}{L}\int_0^L T_w(x).dx$ represents average wall temperature, and L is the device length. The realization of various steady flow-boiling regimes depend on the stability of the various time-averaged values of flow variables – which also depends on avoidance of phenomena associated with critical heat-flux (CHF), as discussed in literature (Carey 1992; Ghiaasiaan 2007; Thome 2004) and later on in Sects. 2 and 3. For characterizing macroscale convection-dominated phase-change flows, or the convective component of these flows, standard continuum-level fluid properties and associated non-dimensional numbers for flow boiling and flow condensation are sufficient (Naik and Narain 2016; Naik et al. 2016; Narain et al. 2015; Ranga Prasad et al. 2017).

Flow-boiling regimes, however, often involve significant amount of macro- and microscale nucleate boiling, and, therefore, added dependences on a nondimensional parameter set {S*} should be included. This nondimensional parameter set {S*} would represent relevant properties and other variables that characterize vapor-liquid-solid interactions at micro-/nanolayers found near contact lines over the heated solid surfaces and particularly those which, in turn, influence macroscopic behavior of nucleating bubbles (see Carey 1992; Ghiaasiaan 2007; Raghupathi and Kandlikar 2016, etc.). Directly or indirectly, the list of such variables may include

contact angles, surface-texture profile measures, liquid-vapor-solid interactions that relate to contact angles and nucleation site density, surface chemistry, and time-averaged local values of wall heat-flux (or wall temperature) that affect the growth, departure, and emission frequency of a representative bubble. The transient bubble dynamics (not necessarily the average steady nucleate boiling heat transfer coefficient) is also affected by parameters that affect the bubble ebullition cycle related thermal transients of the externally or internally heated solid, which forms the boiling surface (these include the solid's density, specific heat, thermal conductivity, and characteristic thickness in the heat flow direction).

Similar to nucleate boiling (pool or flow), the analogue for condensation is nucleation of vapor in the form of dropwise condensation on hydrophilic/super-hydrophilic or hydrophobic/super-hydrophobic surfaces – with or without discussions of condensate removal mechanisms (inclined or vertical plates, moving vapor, etc.). Such condensation has high heat-flux capabilities and is of great current fluid physics interest (see Rykaczewski et al. 2013 and ▶ Chap. 50, "Film and Dropwise Condensation"). For reasons related to durability of such mechanisms and development of applications of interest, the traditional (Fig. 2) and innovative (Fig. 3b) mm-scale annular flow-condensers remain the primary interest of this review.

The primary focus of this review is, however, innovative annular steady operations (without the imposition of pulsations) depicted in Fig. 3a, b. The focus is on quantitative characterization of such flows and flow control-based avoidance of neighboring non-annular flow-regimes (typically thermally inefficient plug-slug regimes in Figs. 1 and 2). This is because innovative operations, such as those in Fig. 3, involve controlled recirculation rate for the passive vapor flow through proper setting of the inlet quality for a given device length L, mass-flux G, and a range of heating/cooling conditions. Characterization of the heat transfer efficiency for the flows in Fig. 3 involves quantitative assessment of the local values of *heat transfer coefficient* (h_x) appearing in the defining relationship: $q_w''(x) \equiv h_x \cdot \Delta T(x)$ or $q_w''(x) \equiv h_x \cdot \Delta T$. This later definition involving mean temperature difference is rarely used in the context of local heat-flux – it is often an engineering convenience when $\Delta T(x)$ is not known or its spatial variations are not significant. Typically, for the annular flows in Fig. 3, one seeks a correlation of nondimensional values of h_x in terms of suitable nondimensional values of *overall* flow variables, namely, mass-flux G, quality X (x), heating levels (average heat-flux $\overline{q}_w''$ representing $q_w''(x)$ variation or average temperature difference ΔT representing $\Delta T(x)$ variation), heating methods characterized by fixed spatial dependence of ratios such as $q_w''(x)/\overline{q}_w''$ (or $\Delta T(x)/\Delta T$), and relevant fluid properties. Furthermore, clearly for the annular flows in Fig. 3, some key *intermediate* flow variables such as local film thickness $\delta(x)$, interfacial shear, ratio of average gas and average liquid-phase velocities (U_V and U_L) being determined through their dependence on fluid properties, quality X, and the *void fraction* ϵ play a significant role in determining the spatial variations in the overall flow variables (such as X(x)). Void fraction ϵ ($\equiv A_G(x)/A$, where $A_G(x)$ is the mean cross-sectional area occupied by the gas phase at location "x," etc.), along with its dependence on ratio of average gas and average liquid-phase velocities (U_V and U_L), is discussed later on in Sect. 3. For a more general definition of the void fraction (ϵ),

see Carey (1992), Ghiaasiaan (2007), Thome (2004), etc. Another key *intermediate* flow variable that is influenced by interfacial shear – through wall shear stress values – is the local pressure gradient dp/dx(x) associated with the pressure p(x) averaged over a cross-section, which, in turn, relates to pressure-drop and pumping power associated with the device. All these intermediate flow variables are very important in defining and obtaining suitably characterized relationships for the *overall* variables and the local heat transfer coefficient h_x.

The above discussions necessitate a brief overview of relevant knowledge that exist with regard to correlations for:

- Heat transfer coefficient h_x or its nondimensional form termed Nusselt number Nu_x
- Defining flow-regime maps with distance "x" or quality "X(x)" with the help of suitable representation of flow-regime transitions – defined by critical values of quality X_{cr} as a function of other nondimensional parameters characterizing the realization of flows (see Figs. 1, 2, and 3)
- Void fraction ϵ and its dependence on quality X and fluid properties
- Pressure gradient and/or pressure-drop values
- Obtaining different critical heat-flux (CHF) values and associated qualities X_{cr-CHF} that are relevant to the mechanisms by which unstable conditions arise due to high enough average values of externally imposed heat-flux

Toward addressing the above-described correlation needs, a broad overview as well as review is undertaken in the next two sections.

2 Basic Variables and Correlations of Scientific and Engineering Interest and their Relationship to One-Dimensional Modeling of Flow Boiling and Flow Condensation

2.1 Basic Variables and Their Correlations

In this review, the primary focus is on the shear and pressure-drop-driven annular flows inside tubes of circular (diameter D) or rectangular (height h and width w) cross-sections, including channels (i.e., $h/w \ll 1$ rectangular cross-sections; also see ▶ Chaps. 47, "Flow Boiling in Tubes," and ▶ 48, "Boiling and Two-Phase Flow in Narrow Channels"). Both traditional saturated flow boiling and flow condensation (Figs. 1 and 2) and innovative annular flow operations (Fig. 3a, b) are of interest. A single characteristic length scale, popularly used in the hydrodynamics literature for defining pressure-drop and phase-specific Reynolds number, is used. This is the hydraulic diameter:

$$D_h \equiv 4A/P \tag{1}$$

where A is the tube cross-sectional area and $P = P_F$ is the wetted (by liquid or vapor) perimeter. For order of magnitude estimates of heat transfer rates in tubes of different cross-sectional geometries but equivalent diameters, if curvature effects are secondary (which is not the case here), many Nusselt number definitions may prefer to use D_h in Eq. (1) after replacing the perimeter P by $P = P_H$ in Eq. (1) where P_H is the heated perimeter, which may only be a fraction of P_F. To address such a need, retaining the definition in Eq. (1), as needed, the D_h value may be explicitly multiplied by the fraction "$fr_P \equiv P_H/P_F$." Furthermore, for present purposes, commercially smooth and hydrophilic heating/cooling surfaces (i.e., heat-exchange surfaces) are assumed for the flows in Figs. 1, 2, and 3. This does not mean that special cross-sections (elliptical as opposed to circular, square, rectangular, etc.), mini- and macro-fins, twisted tape inserts, and special hydrophilic or hydrophobic micro- and nanostructured surfaces (see Kim et al. 2006; Mogaji et al. 2013; Thome 2004; Wu et al. 2013, etc.) aren't actively being investigated – or relevant here (when discussed) – for performance enhancement purposes (also see ▶ Chap. 43, "Boiling On Enhanced Surfaces").

As mentioned earlier, commonly available pure fluids (refrigerants, fluorinert electronic cooling fluids, water, etc.) are the primary focus of this chapter – although the literature also shows a significant amount of interest in phase-change flows with azeotropic and non-azeotropic fluid mixtures, nano-fluids, and phase change in the presence of non-condensable gases (see Dalkilic and Wongwises 2009; Kim et al. 2007; Shah 2015b, etc.; also see ▶ Chap. 44, "Mixture Boiling").

The liquid and vapor phases in the flows of Figs. 1, 2, and 3 are denoted with subscripts I = "L" and I = "V," respectively. Both phases are modeled as incompressible (i.e., vapor Mach numbers are low). The properties (density ρ, viscosity μ, specific heat C_p, and thermal conductivity k) are denoted with subscript "I." The properties are to take their representative constant values for each phase (I = "L" or "V").

Let the temperature, pressure, and velocity fields over the two phases – for the steady-in-the-mean flows depicted in the Figs. 1, 2, and 3 – be, respectively, denoted as T_I, p_I, and $\vec{v}_I = u_I\hat{\mathbf{i}} + v_I\hat{\mathbf{j}}$. Let p_0 be the mean inlet pressure (or inlet pressure at a designated inlet location), h_{fg} be the heat of vaporization at a local interfacial pressure p or associated saturation temperature $T_{sat}(p)$, and $\overline{T}_w$ be the mean heat-exchange surface temperature associated with steady but spatially varying wall temperature $T_w(x)$. Further, let $\Delta T\left(\equiv \left|T_{sat}(p_0) - \overline{T}_w\right|\right)$ be a representative controlling temperature difference between the fluid and the heat-exchange surface and $\dot{M}_{in}$ be the total steady mass flow rate (kg/s) through the tube. Furthermore, let $\dot{M}_{in}$ consist of liquid mass flow rate $\dot{M}_L(x)$ and vapor mass flow rate $\dot{M}_v(x)$ at any distance "x" from the inlet – i.e., $\dot{M}_{in} = \dot{M}_L(x) + \dot{M}_v(x)$. Let $X(x)\ \left(\equiv \dot{M}_V(x)/\dot{M}_{in}\right)$ be the local quality and $G\ \left(\equiv \dot{M}_{in}/A\right)$ be the mass flux (kg/m^2 s), and let the overall characteristic speed be $U\ (\equiv G/\rho_V)$. The "method of heating/cooling" for the flows in Figs. 1, 2, and 3 can be specified by prescribing either the wall temperature values or the heat-flux values. The prescription choice depends on which of the two wall variables is experimentally known or is more conveniently assumed as a tentative prescription. A tentative prescription suffices if it is a conjugate problem and the

boundary conditions for the surrounding environment are sufficiently known to *find* the assumed thermal boundary condition. It is common to replace wall temperature variations $T_w(x)$ by the characterizing temperature difference $\Delta T(x)$.

Next, it is important to define the "level" of heating/cooling. Over the heating/cooling length "L" in Figs. 1, 2, and 3, these "levels" are characterized by either the average temperature difference $\Delta T \equiv \left|\overline{T}_w - T_{sat}(p_0)\right|$ between the saturation temperature $T_{sat}(p_0)$ and the axially averaged mean wall temperature $\overline{T}_w \equiv \frac{1}{L}\int_0^L T_w(x).dx$ or the axially averaged mean wall heat-flux $\overline{q}_w^{''} \equiv \frac{1}{L}\int_0^L q_w^{''}(x).dx$. Furthermore, a specific nonuniform "method of heating/cooling" is defined as $\theta_w(x)$ or $\Psi_q(x)$ through the relations:

$$\Delta T(x) \equiv |T_w(x) - T_{sat}(p_0)| \equiv \Delta T.\theta_w(x) \tag{2}$$

and

$$q_w^{''}(x) = \overline{q}_w^{''}.\Psi_q(x) \tag{3}$$

For nonuniform temperature-controlled heating/cooling, a specific $\theta_w(x) \neq 1$ over $0 \leq x \leq L$ defines a specific "method of heating/cooling," whereas for uniform temperature heating/cooling that specific function is $\theta_w(x) = 1$ over $0 \leq x \leq L$. Similarly, for a nonuniform wall heat-flux controlled heating/cooling, a specific $\Psi_q(x) \neq 1$ over $0 \leq x \leq L$ defines a specific "method of heating/cooling," whereas for uniform heat-flux heating/cooling that specific function is $\Psi_q(x) = 1$ over $0 \leq x \leq L$.

The heat transfer to or from heat-exchange surfaces for the phase-change flows in Figs. 1, 2, and 3 are characterized by the value of local heat transfer coefficient h_x defined as:

$$q_w^{''}(x) \equiv h_x.\Delta T(x) = h_x.|T_w(x) - T_{sat}(p_0)| \tag{4}$$

where local heat transfer coefficient h_x depends on the overall flow-specifying geometry and boundary conditions. Once it is assumed that straight ducts and their orientation with respect to gravity are of interest here, the local heat transfer coefficient h_x depends on the following variables: distance "x" from the inlet, tube diameter D_h, inlet mass flow rate $\dot{M}_{in}$, relevant fluid properties, controlling thermodynamic variables for phase change, the "level of heating/cooling" as specified by values of ΔT (or $\overline{q}_w^{''}$), the "method of heating/cooling" as specified by the functions $\theta_w(x)$ or $\Psi_q(x)$ at the tube walls, values of gravity components g_x and g_y, and inlet quality X_{in}. The above list of dependencies assumes, as needed, an implicit or explicit dependence on solid-liquid-vapor interactions specifying parameters set {S*}, as discussed earlier for the nucleate boiling component. It should be noted that $g_x \cong 0$ for the horizontal flow configurations of interest in Figs. 1, 2, and 3 and the quality X_{in} at the inlet ($x = 0$) is zero for saturated flow boiling in Fig. 1, unity ($X_{in} = 1$) for saturated flow condensation in Fig. 2, and X_{in} is such that $0 < X_{in} < 1$, for the flows in Fig. 3a, b. For traditional flow realizations in Figs. 1 and 2, with

known wall temperature "method of heating," if "x" is lying in the convection-dominated plug-slug or annular regimes, this means that one can assume that the convective component $h_{x|cb}$ of the heat transfer coefficient $h_x \equiv h_{x|cb} + h_{x|nb}$ for flow boiling (assuming microscale nucleation contribution $h_{x|nb}$ remains an important contribution for annular flow-boiling zone III in Fig. 1b), or total heat transfer coefficient h_x (for flow condensation; or for flow boiling with an assumed implicit dependence on {S*}; or for suppressed/negligible nucleation flow boiling for which $h_x \cong h_{x|cb}$, as in zone-V of Fig. 1b); one can write the dependence for $h_{x|cb}$ or h_x as:

$$h_{x|cb} \equiv h_{x|cb}\left(x, G, D_h, \Delta T, \theta_w(x), \rho_L, \rho_V, \mu_L, \mu_V, C_{pL}, k_L, h_{fg}, \sigma, |g_x|, |g_y|\right) \tag{5}$$

Similarly, for known wall heat-flux "method of heating/cooling," Eq. (5) for the flows in Fig. 1 is replaced by:

$$h_{x|cb} \equiv h_{x|cb}\left(x, G, D_h, \overline{q}''_w, \Psi_q(x), \rho_L, \rho_V, \mu_L, \mu_V, C_{pL}, k_L, h_{fg}, \sigma, |g_x|, |g_y|\right) \tag{6}$$

With regard to explicit or implicit dependence for flow-boiling heat transfer coefficient $h_x \equiv h_{x|cb} + h_{x|nb}$ on {S*}, the following practice is recommended. If $h_{x|nb}$ dominates in its contribution to the value of h_x in a way that its dominance is not controlled by convective motion, as in pool boiling, it is best to keep its dependence on {S*} explicit. However in the annular flow-boiling regions IV–V of Fig. 1, micro-nucleation controlled $h_{x|nb}$ may dominate h_x ($\equiv h_{x|cb} + h_{x|nb}$), but this phenomena is likely to be controlled by the convective motion associated with $h_{x|cb}$; in this case it is recommended that the dependence of h_x on {S*} be kept implicit – and this recommendation is followed in this chapter. However, for innovative wavy annular flow boiling along curves $I_{1-(ii)}$ and $I_{2-(ii)}$ in Fig. 1b, c and discussed in Sect. 6, it is recommended that dependence of h_x on {S*} be kept explicit. This is because the expected explosive presence of micro-nucleation and its impact depend significantly on {S*} and, as discussed in Section 6, other external approaches are imposed to influence/control the micro-nucleation phenomena.

Heat transfer coefficient (be it the convective component $h_{x|cb}$ or total h_x) is typically nondimensionalized as Nusselt number Nu_x and is given below:

$$Nu_x \equiv h_x . \frac{D_h}{k_L} \tag{7}$$

At times, for channel flows, the channel height "h" is used as the characteristic length scale (Naik and Narain 2016; Naik et al. 2016; Ranga Prasad et al. 2017) instead of the hydraulic diameter D_h. Also, elsewhere, for channel flows with only bottom-wall heating/cooling – as in Naik et al. (2016) and Ranga Prasad et al. (2017) – D_h is replaced by $\widetilde{D}_h \equiv D_h \cdot fr_P = 4h$ as the characteristic length in the Nu_x definition.

Using the Nu_x definition in Eq. (7), it is easily seen that the functional dependencies in Eqs. (5) and (6) can be nondimensionalized, with the help of Pi-theorem (White 2003), in the following forms:

$$Nu_{x|conv} \equiv Nu_{x|conv}\left(\hat{x}, Re_T, Ja, Pr_L, We, Fr_x^{-2}, Fr_y^{-2}, \frac{\rho_V}{\rho_L}, \frac{\mu_V}{\mu_L}, \theta_w(x)\right) \tag{8}$$

and

$$Nu_{x|conv} \equiv Nu_{x|conv}\left(\hat{x}, Re_T, Bl, Pr_L, We, Fr_x^{-2}, Fr_y^{-2}, \frac{\rho_V}{\rho_L}, \frac{\mu_V}{\mu_L}, \Psi_q(x)\right) \tag{9}$$

In Eqs. (8) and (9), $\hat{x} \equiv x/D_h$, $Re_T \equiv GD_h/\mu_V$, $Ja \equiv C_{pL}\Delta T/h_{fg}$, $Pr_L \equiv \mu_L C_{pL}/k_L$, $Fr_x^{-2} \equiv |\, g_x \,|\, D_h/U^2$, $Fr_y^{-2} \equiv |\, g_y \,|\, D_h/U^2$, $We \equiv \rho_L U^2 D_h/\sigma$, and $Bl \equiv \overline{q}_w''/Gh_{fg}$. In Eqs. (8) and (9), we have not recommended use of $Ja(x) \equiv Ja \cdot \theta_w(x)$ and $Bl(x) \equiv Bl \cdot \Psi_q(x)$ because often (i) the nondimensional spatial variation functions θ_w or Ψ_q defining the "method of heating/cooling" are not known or (ii) they are not "far," in an integral sense, from their corresponding uniform case value of "1." The total Reynolds number Re_T simply represents nondimensional value of mass-flux G – where its use of vapor viscosity μ_V is appropriate for traditional flow-condensation cases in Fig. 2 or innovative flow-boiling and flow-condensation cases in Fig. 3. For traditional flow-boiling case in Fig. 1, it is more appropriate to nondimensionalize G by using liquid viscosity μ_L and replacing Re_T in Eqs. (8) and (9) by $\widetilde{Re}_T \equiv Re_T \cdot \mu_V/\mu_L$. Nondimensional surface-tension parameter Weber number (We) may also influence steady annular flows in Fig. 3, particularly if tube diameters are small and, therefore, interfacial curvatures are high (in different ways and places of the interfacial configurations realized in a rectangular cross-section as opposed to a circular cross-section).

For annular flow boiling in Fig. 3, the argument list in Eqs. (8) and (9) has direct additional dependence on inlet quality X_{in} (Ranga Prasad et al. 2017), and for Nu_x representing the total heat transfer coefficient h_x, Eqs. (8) and (9), the structure for convective boiling component of the Nusselt number $Nu_{x|cb}$ (Ranga Prasad et al. 2017) admits implicit additional dependence on nondimensional parameter set {S*} that represent relevant vapor-liquid-solid interactions.

The condensing/boiling flows of interest typically exhibit a one-to-one correspondence because of monotonically decreasing/increasing values of quality X with distance x (or nondimensional distance $\hat{x}$). It is therefore possible and common to replace the nondimensional distance $\hat{x} \equiv x/D_h$ in Eqs. (8) and (9) by the local quality $X(\hat{x})$ defined as:

$$X(\hat{x}) = \frac{\dot{M}_v(\hat{x})}{\dot{M}_{in}} \tag{10}$$

One of several reasons for replacing distance $\hat{x}$ with quality X is the expectation that its use, in place of "$\hat{x}$," will allow more convenient and meaningful

characterization of flow-regimes (except near transition boundaries) because of approximate similarities found among different flow-regimes encountered in phase-change flows (see Figs. 1, 2, and 3) and those encountered for different realizations of adiabatic flows (Ghiaasiaan 2007; Thome 2004). It is again noted here that, for adiabatic flows, a uniform quality $X(x) = X$ over $0 \leq x \leq L$ retains a value between zero and one. Another advantage of using X in place of $\hat{x}$ – for developing the Nu_x (or $Nu_{x|cb}$) correlations in Eqs. (8) and (9) – is that such uses are likely to significantly weaken the influence of different functions $\theta_w(\hat{x})$ or $\Psi_q(\hat{x})$ that characterize the effects of spatially nonuniform methods of heating/cooling. For a certain class of annular flow boiling, this fact has been verified by Ranga Prasad et al. (2017). As a result of the above, it is a common practice to characterize heat transfer for phase-change flow processes in horizontal tube configurations of Figs. 1, 2, and 3 (where $g_x = 0$ and effects of g_y are often negligible within the plug-slug or annular regimes of interest but may affect the flow-regime transition boundaries) by seeking Nu_x correlation for known wall temperature heating/cooling cases – using experiments or computations or their synthesis – in the simplified functional dependence structure of the form (or its equivalent):

$$Nu_x \equiv Nu_x \left(X, Ja, Re_T, Pr_L, We, \frac{\rho_V}{\rho_L}, \frac{\mu_V}{\mu_L} \right) \tag{11}$$

For a known heat-flux specifying the "method of heating/cooling" of horizontal tubes, the Nusselt number dependence is of the simplified form (or its equivalent):

$$Nu_x \equiv Nu_x \left(X, Bl, Re_T, Pr_L, We, \frac{\rho_V}{\rho_L}, \frac{\mu_V}{\mu_L} \right) \tag{12}$$

The nondimensional arguments in Eqs. (8) and (9) or Eqs. (11) and (12) simply represent a broad structure and may implicitly assume additional dependence, particularly if it is important to precisely decompose $h_x \equiv h_{x|cb} + h_{x|nb}$, on the earlier discussed nondimensional parameter set $\{S^*\}$ representing relevant parameters characterizing vapor-liquid-solid interactions. While developing correlations, one may choose to simplify the dependences further or optimize them by changing the definitions of different nondimensional numbers into different equivalent combinations. For example, one may choose to limit mass-flux (G or speed $U \equiv G/\rho_V$) effects to Reynolds number Re_T and replace Weber number We and Froude numbers (Fr_x^{-2} and Fr_y^{-2}), respectively, by Suratman number Su ($\equiv \sigma\rho_V D_h/\mu_V^2$) and a pair of nondimensional gravity numbers (g_{nd-x} and g_{nd-y} where $g_{nd-x\ (or\ y)} \equiv \left|g_{x\ (or\ y)}\right| . \rho_V^2 . D_h^3/\mu_V^3$).

Furthermore, for thin film annular flows of Fig. 3, as established by several analyses (Narain et al. 2015; Ranga Prasad et al. 2017), independent dependences on Ja and Pr_L on the right sides of Eqs. (11) and (12) can be further simplified by a single parameter dependence on "Ja/Pr_L." Thus, for thin steady annular flows of Fig. 3 restricted to mm-scale channels (curvature of the interface is negligible), effect

of the surface-tension parameters (We or Su) can be assumed to be negligible, and one can replace Eqs. (11) and (12) by their respective and further simplified forms – with the addition of inlet quality X_{in} (which is an independent additional variable only for innovative flow boiling, as $X_{in} = 1$ for innovative flow condensation) – given below:

$$Nu_x = Nu_x\left(X, X_{in}, Re_T, \frac{Ja}{Pr_L}, \frac{\rho_V}{\rho_L}, \frac{\mu_V}{\mu_L}\right) \tag{13}$$

and

$$Nu_x = Nu_x\left(X, X_{in}, Bl, Re_T, Pr_L, \frac{\rho_V}{\rho_L}, \frac{\mu_V}{\mu_L}\right) \tag{14}$$

Again for annular flow boiling with nucleation, Eqs. (13) and (14) only specify the structure for $Nu_{x|cb}$ – i.e., convective component of HTC (see Ranga Prasad et al. 2017) – unless an implicit dependence on the earlier alluded nondimensional parameter set {S*} is assumed. The goal is to carefully obtain correlations of the forms (or their equivalent) given in Eqs. (8) and (9) or (11) and (12) or (13) and (14), over a well-defined parameter space, by employing information obtained from experiments, or accurate modeling/simulation techniques, or a synthesis of the two.

If Nu_x correlations in the above form (or equivalent) could be reliably and completely obtained from experimental data obtained for flow-boilers and flow-condensers, such experimental correlations would already be consistent – at least approximately – with all the relevant laws of nature (mass, momentum, energy, etc.). This is because experimental realizations automatically satisfy all the relevant laws of nature.

2.2 Other Indirect Variables and Their Influence on Aforementioned Key Variables

Laminar or Turbulent Nature of Flows The total Reynolds number Re_T cannot shed much light on the expected laminar or turbulent nature of the different phases in annular flows. Clearly laminar or turbulent nature of the flows impacts heat transfer correlations for Nu_x and most other variables of interest. For this assessment, one often uses "local" values of liquid and vapor Reynolds numbers ($Re_L(x)$ and $Re_V(x)$, respectively) defined as:

$$Re_L \equiv \frac{G\cdot(1 - X(x))\cdot D_h}{\mu_L} \tag{15}$$

and

$$Re_V \equiv \frac{G\cdot X(x)\cdot D_h}{\mu_v} \tag{16}$$

For separated annular flows, Re_L (or Re_V) < 2000 continue to indicate laminar nature of the flow in that phase. Similarly, Re_L (or Re_V) $\gg 2000$ continue to indicate turbulent nature of flow in that phase, with D_h based on wetted perimeter, as in Eq. (1), being used. In fact for thin film flows over a plate or in a channel, for which $\Delta \ll h$, $Re_\Delta(\equiv G \cdot (1 - X(x)) \cdot 4\Delta/\mu_L) < 1800$ is the more appropriate – and less conservative – thin-film flow laminarity criteria (see Bergman et al. 2011 for Nusselt solution for film condensation) which is automatically satisfied, whenever $Re_L < 2000$.

Flow-Regime Transition Criteria The instabilities that lead to transition between one flow-regime "i" to another downstream/upstream regime marked as "i + 1" /"i-1" often need to be characterized with the help of a relationship among influencing variables. This typically leads to a representative "critical" value or a range of critical values of quality X (i.e., $X_{cr|i \to (i\pm1)}$ or $X_{cr-L|i \to (i\pm1)} \le X_{cr} \le X_{cr-H|i \to (i\pm1)}$) that mark a transition between two adjacent regimes – viz., "i" to "i ± 1" – as quality X sufficiently increases or decreases in Figs. 1 and 2. Such transitions clearly influence the nature of the Nu_x correlation function and most variables of interest. For the annular thin-film flows in Fig. 3, the significant nondimensional parameters being the ones listed on the right sides of Eqs. (13) and (14), one expects that the transition criteria between "regime - i ≡ regime - annular" and "regime - |i±1| ≡ regime - plug/slug" need characterizations for known temperature or known heat-flux ways of specifying the "methods of heating/cooling." Therefore, in principle, these can be obtained in the following forms:

$$X_{cr|i\to(i\pm1)} = X_{cr|i\to(i\pm1)}\left(\frac{Ja}{Pr_L}, Re_T, \frac{\rho_V}{\rho_L}, \frac{\mu_V}{\mu_L}\right) \tag{17}$$

or

$$X_{cr|i\to(i\pm1)} = X_{cr|i\to(i\pm1)}\left(Bl, Re_T, \frac{\rho_V}{\rho_L}, \frac{\mu_V}{\mu_L}\right) \tag{18}$$

Clearly, the characterizing functions in Eqs. (17) and (18) will also depend on the laminar or turbulent nature of the flows – as assessed through Reynolds number values obtained through definitions in Eqs. (15) and (16) – that may exist for the separate phases of the annular regime.

Film Thickness and Void-Fraction Correlations Heat transfer rates obtained from Nu_x correlations should, clearly, also depend on the thinness of the liquid films adjacent to the heat-exchange surfaces (e.g., the liquid film thickness $\Delta(x)$ in the annular flows of Fig. 3 or liquid thickness near the heat-exchange surface in the plug-slug or annular regimes in Figs. 1 and 2). For most steady annular regimes of interest here, an estimate of film thickness can be obtained from measurements based on experimental correlations for void fraction ϵ, whose definition and expected dependences for flows of interest are of the type:

$$\epsilon \equiv \frac{A_G}{A} = \epsilon \left(X, \frac{\rho_V}{\rho_L}, \frac{\mu_V}{\mu_L}, Re_T, \text{other parameters} \right) \tag{19}$$

Pressure-Drop and Friction Factors Clearly, for annular flows in Fig. 3 and plug-slug flows in Figs. 1 and 2, representative overall pressure gradients $\left(-\frac{\partial p}{\partial x}\Big|_{total}\right)$ are significantly coupled to the flow-regimes and are also related to the local flow quality X (x). For annular flows in Fig. 3, the pressure gradients are more directly influenced by interfacial shear and liquid film thickness Δ(x), which, in turn, also control heat transfer rates being sought through Nu_x correlations of the type given by Eqs. (13) and (14). The overview in the next section outlines the importance of such correlations to many Nu_x correlation in the literature (Ghiaasiaan 2007; Thome 2004).

Flow and CHF-Related Instabilities Time-varying *system* instabilities for internal phase-change flows may also arise due to limitations in the *system* (see discussions in the category of "Static Instabilities" in Saha and Celata 2016) – outside the condenser and/or the boiler of interest – that do not allow the required steady flow boundary conditions to be realized. The main issue is that the device (flow-boiler and flow-condenser) often needs to realize its particular and intrinsic steady flow under the specifications of hydrodynamic and thermal boundary conditions at the inlet and at the duct walls. This requires that the system (i.e., the device and its environment) design be such that it allows the flow the necessary freedom to self-seek a particular set of exit conditions (e.g., pressure or liquid-vapor mass flow rates). However, such devices are often placed in a "closed" flow loop, which physically connects the exit of the device to the inlet of the device – via an external flow loop – thereby making the inlet and exit conditions potentially *interdependent*. Since the design of the external flow loop may have its own characteristics and limitations (e.g., the nature of "pressure-drop versus flow rate curve" for the external flow loop might be quite different than the one for the device/test section of interest), which, in turn, are dependent on the types of devices (pumps, heaters and their controls, etc.) chosen for the external flow loop, certain time-varying instabilities may arise (e.g., Ledinegg 1938 instability discussed in Saha and Celata 2016). Such system-induced instabilities are not the focus of this chapter. This is partly because most such instabilities – which arise from a coupling between the inlet and the outlet of a flow-boiler or a flow-condenser – can be suppressed by employing modern design methods for the flow loop, such as the ones discussed in Sect. 6 of this chapter as well as in Kivisalu et al. (2014) and Sepahyar (2018). These modern designs use the latest in electronic flow control, electronic control of heating/cooling methods, and use of suitable and controllable hardware to effectively eliminate the effects of the connection that exists between the inlet and the outlet of a device in a closed flow loop.

If the boiler and/or condenser employs acoustic waves within the subsonic and incompressible vapor flow, an example being the devices in Fig. 3 (further discussed in Sect. 6 of this chapter), the device may start exhibiting dynamic instabilities if

certain amplitude thresholds are crossed with regard to the external actuation of the underlying waves. Typically, such dynamic responses are also likely to be dependent on the nature of exit geometry and exit flow conditions. Thus, either for subsonic flows (with externally actuated pulsations) or supersonic vapor-phase operations, if certain threshold flow conditions are crossed, density waves, acoustic oscillations, thermal oscillations, pressure-drop oscillations, etc., may arise as dynamic instabilities, that is, they may not allow "steady-in-the-mean" flow realizations. Such instabilities (see Saha and Celata 2016) are also not the focus of this chapter.

The major focus of this chapter is on realization of steady or "steady-in-the-mean" flows with vapor at subsonic speeds within the boiler and the condenser – and under conditions (hydrodynamic and thermal) that suppress dynamic instabilities of the type mentioned above. It is assumed here that the flow loop can be designed to provide adequate freedom for the steady realizations of flows in a way that it allows the flows to self-seek appropriate exit condition (e.g., exit pressure or exit values of liquid-vapor mass flow rates). Furthermore, the totality of the hydrodynamic and thermal conditions at the inlet and the wall is assumed to be such that they suppress dynamic instabilities of the types discussed earlier.

Despite the exclusion of the above-described instabilities by properly defining/restricting the range of operating conditions for the device, the flows *within* the duct can still exhibit a "static" and a "dynamic" instability type – both of these are of primary interest here.

The kind of "static" instabilities that occur within a flow-boiler/flow-condenser and are of interest here has already been discussed in the introduction and earlier in this section (under *flow-regime transition criteria*). These are instabilities that cause one "steady-in-the-mean" flow pattern (or flow-regime) – as far as liquid-vapor interface configurations are concerned – to gradually lose its stability (around a certain critical value of quality, X_{cr}, discussed through Eqs. (17) and (18)) via a downstream or upstream transition to another flow pattern (or flow-regime). The transitions from nucleate/bubbly to plug-slug to annular – as discussed earlier for the flows in Figs. 1 and 2 – fall in this category.

The kind of "dynamic" instabilities that are of interest here are limited to flow-boilers and are called critical heat-flux (CHF) instabilities for flow boiling (see Carey 1992; Collier and Thome 1994; Dhir 1998; Ghiaasiaan 2007, etc.). These are dynamic instabilities that arise when certain threshold values of $\left\{\overline{q}_w^{''}, G, X(x)\right\}_{cr}$ are crossed together under increasing values of the externally imposed mean heat-flux $\overline{q}_w^{''}$. For convenience, we *only* consider uniform x-independent heat-flux $\overline{q}_w^{''} = q_w^{''}$ imposition cases here. There are two principle CHF mechanisms for saturated flow boiling. One corresponds to *dynamic instability* of the dry-out zone in Fig. 1a – as a certain lower limit of the critical heat-flux ($q_{w-CHF1-L}^{''}$ in Fig. 1b) is crossed by increasing values of $q_w^{''}$. Under these conditions, the physical location of the dry-out point in Fig. 1b – indicated as x_{CHF1} (t), which corresponds to the peak just prior to precipitous drop in h_x values – starts oscillating, predominantly in the upstream direction. And $\Delta T(x)$ in the dry-out zone, represented by the vertical axis in Fig. 1c, now takes the new meaning of becoming a time-varying $\Delta T_{s\phi}$ – the

temperature difference representing unsteady heating in the vapor-blanketed zone, with an increasing wall temperature $T_w(x, t)$ values' difference from the more slowly increasing mean temperature of the poorly conducting gas phase above it. The second CHF mechanism (termed CHF2) corresponds to *dynamic instability* of the inverted annular zone in Fig. 4a – as a certain lower limit of the critical heat-flux (q''_{w-CHF2} in Fig. 4b-c) is crossed by increasing values of q''_w from levels below it. Again physical location of the onset of inverted annular flows – indicated as x_{CHF2} (t) – starts oscillating, predominantly in the upstream direction. The important issues are (i) when do inverted annular flows occur, and (ii) how is the inverted annular flow realization related to the two CHF mechanisms – and these are further discussed next. The discussions, we believe, are improvements in qualitatively and progressively improved interpretations that have been evolving through Dhir (1998), Collier and Thome (1994), Lee and Mudawar (2009), etc.

Curves (i)–(iv) in the qualitative "$h_x - X(x)$" depictions in Fig. 1b correspond to increasing uniform heat-flux (q''_w) impositions at or below the lower threshold value of $q''_{w-CHF1-L}$ (see corresponding points (i)–(iv) in Fig. 5a, b). These correspond to "low to modest" imposition of heat-flux q''_w values for a specified mass-flux $G = G_0$. That is, increases in q''_w values correspond to the upward movement along (i)–(iv) in Fig. 5a – with (i)–(iii) being points below the *lower critical curve* (associated with heat-flux $q''_{w-CHF1-L}$) and (iv) being the point on it. Alternatively, these values correspond to the upward movement along points (i)–(iv) in Fig. 5b – with (i)–(iii) being points below *the lower nondimensional threshold curve* $\widetilde{Bl}_{cr-L}\left(\widetilde{Re}_T\right)$ in the nondimensional "$\widetilde{Bl} - \widetilde{Re}_T$" plane of Fig. 5b and (iv) being the point on it. The curves (i)–(iii) in Fig. 1b correspond to points (i)–(iii) in Fig. 5a, b. These correspond to *stable* dry-out flow-regimes that are achieved downstream of qualities associated with peaks (in Fig. 1b) just before dry-out (such as the peak for curve (i), at the cusp between regions V and VI which occurs slightly upstream of the dry-out point x_{do} in Fig. 1b). The downstream locations beyond such points are rapidly vapor blanketed, and the wall temperature rapidly rises in the downstream portions of the corresponding curves (i)–(iii) in the "$\Delta T(x) - X(x)$" plane of Fig. 1c. In case of the presence of entrained liquid in the vapor core, onset of single-phase vapor regions may not begin at dry-out points such as x_{do} in Fig. 1b but may occur slightly downstream of it. The $\Delta T(x)$ values associated with curves (i)–(iii) can potentially reach steady and asymptotic equilibrium values of single-phase temperature differences $\Delta T_{s\phi}$, where $\Delta T_{s\phi}$ values represent temperature difference between the wall and the mean temperature of the vapor. Note that curves (ii)–(iv) in regions I–III in Fig. 1c are *below* curve (i) in Fig. 1c. This is because these curves are associated with corresponding curves (i)–(iv) in Fig. 1b through the relationship: $\Delta T(x) = q''_w/h_x$, and percentage increases in q''_w are typically much smaller than percentage increases in h_x (this claim is supported by some experimental data-based correlations presented in subsequent sections). However, for heat-flux prescribed heating along curve (iv), at uniform heat-flux of $q''_{w-(iv)} = q''_{w-CHF1-L}$, as the peaks marked by red arrows in Fig. 1b, c are reached, a dynamic instability sets in oscillations in the dry-out location (with its motion biased toward upstream regions, as discussed

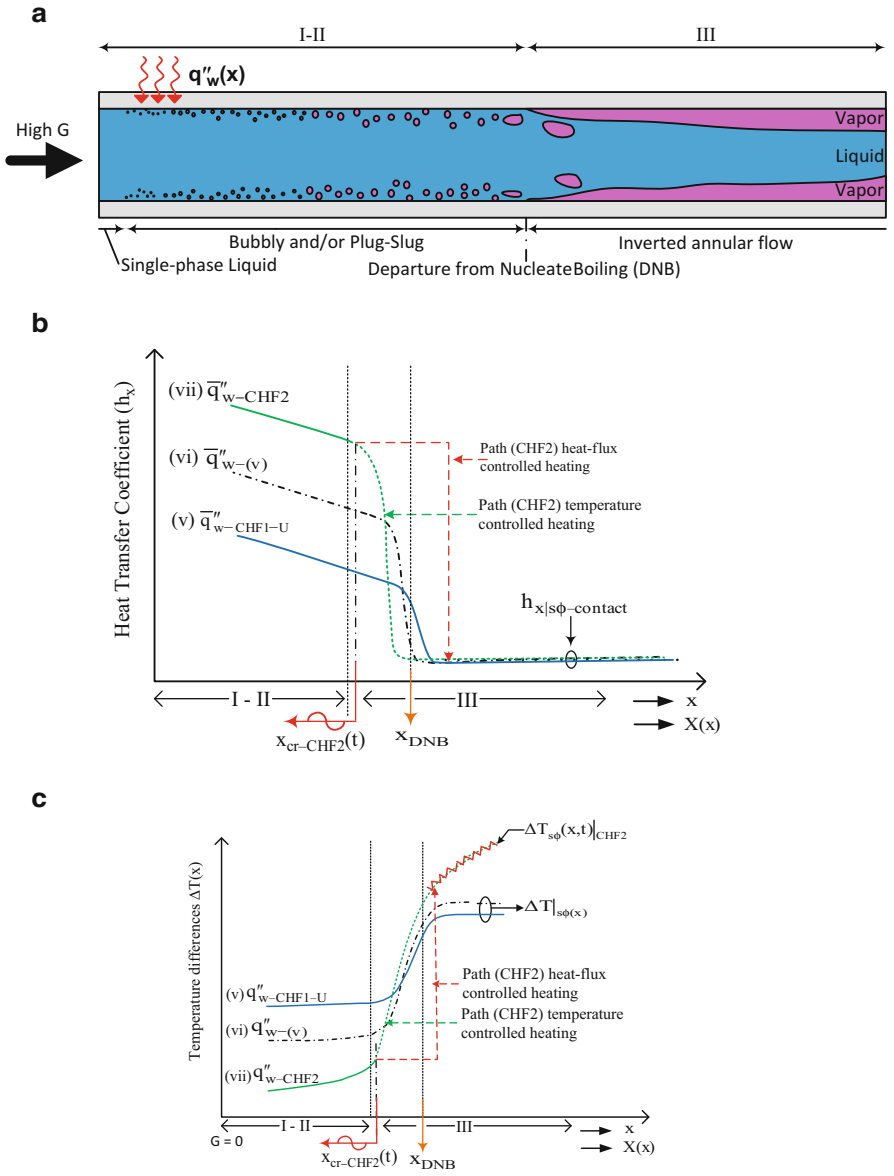

Fig. 4 **(a)** For cases where the average heat-flux $\overline{q}''_w$ for a given mass flux G is at or above a certain threshold $\overline{q}''_{w-CHF1-U}$, the figure depicts the sequence of flow-regimes that are encountered in traditional operations dealing with saturated flow boiling (with saturation conditions at $x = 0$) in a horizontal tube. **(b)** For a certain $G = G_0$ value and the depicted range of imposed heat-fluxes ($\overline{q}''_{w-(v)} < \overline{q}''_{w-(vi)} < \overline{q}''_{w-CHF2} = \overline{q}''_{w-(vii)}$), expected qualitative variation in local values of heat transfer coefficient h_x over $0 \leq x \leq L$ (or thermodynamic qualities $0 \leq X(x) \leq 1$) are shown as curves (v)–(vii). With increasing heat-flux, the decreasing distance or quality from the inlet is

earlier), and the abrupt transition of h_x and $\Delta T(x)$ takes place along the indicated red curves in Fig. 1b, c. Yet, even for this heat-flux prescribed heating along curve (iv) associated with uniform heat-flux of $q''_{w-CHF1-L}$, if a switch is made to a temperature-controlled heating (with the control allowing decreases in heat-flux as needed), further quality increases beyond the peak, without dynamic instability, is possible along the green curves indicated in Fig. 1b, c. The dynamic instability mechanism CHF1 at uniform heat-flux of $q''_{w-CHF1-L}$, as discussed above, does correspond to vapor blanketing at locations downstream of the red marked peak and larger unsteady increases in wall temperature $T_w(x, t)$ relative to single-phase gas temperatures are expected, see Fig. 1c. However, this should not be confused with a runaway unsteady temperature rise in wall temperature that necessarily leads to melting/failure of the solid heated surface, as that phenomenon is highly dependent on the length of the duct, the value of the mass-flux G, and whether or not the imposition of uniform heat-flux value of $q''_{w-CHF1-L}$ is actually sustained. This dynamic instability mechanism for the dry-out location at a critical heat-flux is termed here as CHF1. As indicated in Fig. 5, the dynamic instability of the dry-out point is not only observed along curve (iv) (for heat-flux $q''_{w-CHF1-L}$ in Fig. 1b) but is likely to be observed over a range of heat-flux values ($q''_{w-CHF1-L} \leq q''_w \leq q''_{w-CHF1-U}$).

At heat-flux values higher than $q''_{w-CHF1-U}$, the flow-regimes qualitatively change to the ones depicted in Fig. 4a – where inverted annular regimes begin somewhere near the end of the nucleate boiling or the beginning of the plug-slug regimes of Fig. 1a. In the literature (Collier and Thome 1994; Ghiaasiaan 2007, etc.), the depicted stable onset of inverted annular regimes in Fig. 4a are also termed *departure from nucleate boiling* (DNB). When this heat-flux rises to the heat-flux level of q''_{w-CHF2}, the onset of inverted annular regimes in Fig. 4a also becomes dynamically unstable, and another type of *critical heat-flux* mechanism – termed here as CHF2 in Fig. 4b, c– is reached. At this value, the physical location of the inversion point – indicated as x_{CHF2} (t) – starts oscillating, predominantly in the upstream direction, with $\Delta T(x)$ at locations downstream of x_{CHF2} (t) now takes on the new meaning of becoming a time-varying $\Delta T_{s\phi}$ (with the temperature difference representing unsteady heating in the vapor-blanketed zone, with an increasing wall temperature $T_w(x, t)$ and a more slowly increasing mean temperature of the poorly conducting gas phase above it). This type of *critical heat-flux* mechanism is quite common for saturated and subcooled boiling at high heat-fluxes and is extensively discussed in Collier and Thome (1994), Lee and Mudawar (2009), etc.

The inverted annular flow instability is considered through curves (v)–(vii) in the qualitative "$h_x - X(x)$" depictions given in Fig. 4b. These curves correspond to increasing values of uniform heat-flux q''_w impositions above the lower threshold

Fig. 4 (continued) marked, prior to the beginning of inverted annular flows, as zones I–II. At $\overline{q}''_{w-CHF2} = \overline{q}''_{w-(vii)}$, the inverted annular zone becomes unstable with oscillatory onset locations x_{CHF2} (t). **(c)** The curves (v)–(vii) in (**b**) above are plotted here as $\Delta T(x)$ versus X(x), where $\Delta T(x) \equiv |T_w(x) - T_{sat}(p_0)|$

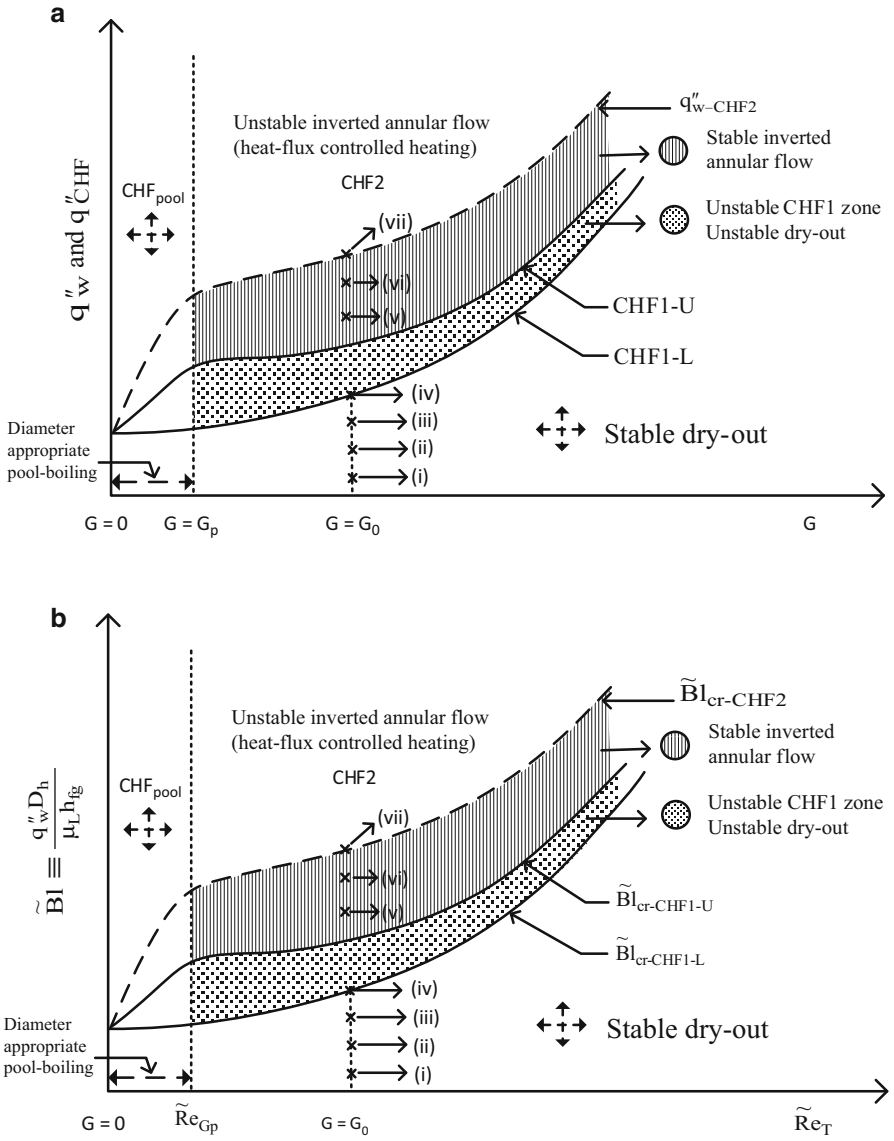

Fig. 5 **(a)** The figure attempts depiction of qualitative threshold values of heat-fluxes associated with dry-out instabilities (CHF1) and inverted annular flow instability (CHF2) in the depicted $q_w^{''} - G$ plane. **(b)** This is a nondimensional version of the figure in (**a**). A different nondimensional heat-flux $\widetilde{Bl} \equiv q_w^{''} \cdot D_h / \left(\mu_L \cdot h_{fg}\right)$ is used to replace Bl as explicit dependence of CHF values on G (or $\widetilde{Re_T}$) is desired

value of $q''_{w-CHF1-U}$ and up to a value termed as q''_{w-CHF2}. These correspond to heat-flux q''_w imposition values for a specified mass-flux $G = G_0$, at the three points (v)–(vii) depicted in Fig. 5. For curves (v)–(vi) in Fig. 4b, *stable* inverted annular flows are achieved downstream of appropriate qualities indicated in Fig. 4b. The downstream locations beyond this point are vapor blanketed, and wall temperature rapidly rises in the aft portions of curves (v)–(vi) in the "$\Delta T(x) - X(x)$" plane of Fig. 4c. Curves (vi) and (vii) in Fig. 4c are *below* curve (v) in the upstream portions of Fig. 4c because curves (v)–(vii), respectively, correspond to the curves (v)–(vii) in Fig. 4b through the relationship: $\Delta T(x) = q''_w/h_x$ and percentage increases in q''_w are typically much smaller than percentage increases in h_x values.

Fig. 5a, b also suggests presence of a low enough mass-flux range $0 \leq G \leq G_p$ where all the flow-boiling CHF mechanisms will behave closer to the CHF mechanism associated with pool boiling.

Both CHF mechanisms arise from the fact that it is possible to raise the "levels" of sustained heating above certain high threshold values that a stable, steady realization of flow boiling – as depicted in Fig. 1a or Fig. 4a – is no longer possible. At such levels, different instability mechanisms are triggered – both leading to a situation where the vapor-blanketed-heated surface of the tube/channel starts experiencing oscillatory dry patches (i.e., the solid surface is exposed directly to the vapor through the adsorbed layer of liquid; see discussions in Sects. 3 and 6) that allow, in time, for unsteady rise in wall temperatures $T_w(x, t)$ when either of the two CHF mechanisms are triggered – with a possibility of a runaway. The gas-phase flow rate over the vapor-blanketed heated wall for CHF2 mechanism is much smaller than the one associated with CHF1, and, therefore, catastrophic rises in wall temperature $T_w(x, t)$ at these higher heat-fluxes ($q''_{w-CHF2} > q''_{w-CHF1-U}$) are more likely.

The main point of the above discussions is to distinguish between CHF mechanisms of pool boiling (Collier and Thome 1994; Dhir 1998) and flow boiling despite obvious similarities. The analogies, as given in Collier and Thome (1994) through three-dimensional qualitative plots involving $\{q''_w, T_w(x), X(x)\}$ axes or the projected curves in the q''_w and $T_w(x)$ planes, can be improved – though it is not done here – with the help of above-reported figures and three-dimensional qualitative plots involving $\{h_x, \Delta T(x), X(x)\}$ or $\{q''_w, T_w(x), X(x)\}$ axes.

Clearly one needs to seek Nu_x correlations of the type given by Eqs. (13) and (14) – provided one is also able to keep wall heat-flux q''_w values *below estimated threshold values* of q''_{CHF1} and q''_{CHF2}.

2.3 Segmented Flow-Regime Dependent Nu_x Correlations

The earlier flow-regime specific discussions (in Sect. 2.2) regarding other indirect variables influencing key variables in the arguments list presented for Nu_x correlations suggest that they may also indirectly influence the very form of the Nu_x function – in ways such that the best forms of the correlations may significantly differ from one flow-regime to another. This suggests that it may be more convenient to obtain the sought-for and more accurate Nu_x correlations in Eqs. (8) and (9) by an

approach that restricts the correlations to one regime at a time. That is, if "regime - i" denotes a particular flow-regime (such as bubbly, plug-slug or annular flow-regimes, etc.), and its neighboring upstream and downstream regimes in Figs. 1, 2, and 3 are, respectively, marked as "regime - (i–1)" and "regime - (i + 1)" – with corresponding flow-regime transition criteria in terms of quality (see Eqs. (17) and (18)) denoted as $X_{cr|(i-1)\rightarrow i}$ and $X_{cr|i\rightarrow(i+1)}$ – one could seek correlations of the type:

$$\begin{aligned} Nu_x &= Nu_{x|regime-i}\left(X, Re_T, \frac{Ja}{Pr_L}, \frac{\rho_V}{\rho_L}, \frac{\mu_V}{\mu_L}, \ldots\right) \\ &\text{or,} \\ Nu_x &= Nu_{x|regime-i}\left(X, BI, Re_T, \frac{\rho_V}{\rho_L}, \frac{\mu_V}{\mu_L}, \ldots\right) \end{aligned} \tag{20}$$

where $X(\hat{x})$ is in the range

$$X_{cr|(i-1)\rightarrow i} \leq X(\hat{x}) \leq X_{cr|i\rightarrow(i+1)} \tag{21}$$

and nondimensional $\hat{x} \equiv x/D_h$.

2.4 Underlying One-Dimensional Modeling Approach to Obtain Spatial x–Variations of Flow Variables That Are Known or Correlated in Terms of Quality X and Other Parameters

For the flow-boiling and flow-condensation realizations in Figs. 1, 2, 3, and 4, one-dimensional energy balance can be applied to the control volume between any two arbitrary locations "x" and "x + Δx" (see Fig. 6).

It is easy to see that, in the limit of $\Delta x \rightarrow 0$, the energy balance yields:

$$\frac{dX(x)}{dx} \cong \pm\frac{|q_w''(x)|\cdot P_H}{\dot{M}_{in} h_{fg}(p_0)} = \pm\frac{h_x|T_w(x) - T_{sat}(p_0)|\cdot P_H}{G\cdot A\cdot h_{fg}} \tag{22}$$

The "+" and "–" signs in Eq. (22) are, respectively, for flow boiling and flow condensation. Using the definitions given earlier, P_H being the heated perimeter (potentially a fraction $fr_P \equiv P_H/P_F$, where P_F is the wetted – by liquid or vapor –

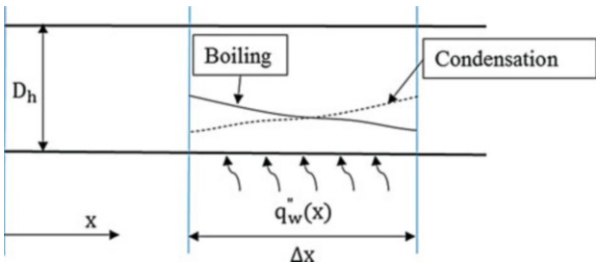

Fig. 6 A schematic of a control volume between "x" and "x + Δx." The heat-flux arrows, as shown, are positive for boiling. The reversed direction negative values are for flow condensation

perimeter), $\dot{M}_{in} \equiv G \cdot A$, and the relevant nondimensional variables and numbers as defined following Eq. (9), Eq. (22) can be nondimensionalized as:

$$\frac{dX(\hat{x})}{d\hat{x}} = \pm 4.fr_P \cdot Nu_x \frac{Ja}{Pr_L} \cdot \frac{1}{Re_T} \cdot \frac{\mu_L}{\mu_V} \cdot \theta_w(x) \tag{23}$$

for known wall temperatures specifying the "method of heating/cooling."

For known heat-flux values specifying the "method of heating/cooling," Eq. (22) is nondimensionalized as:

$$\frac{dX(\hat{x})}{d\hat{x}} = \pm 4.fr_P \cdot BI.\Psi_q(x) \tag{24}$$

2.4.1 Use of Nu_x Correlations Covering All Flow Regimes

For known wall temperatures specifying the "method of heating/cooling," the nonlinear *ordinary differential equation* (ODE) in Eq. (23) may be solved over $0 \leq \hat{x} \leq L/D_h$, in conjunction with a reliable Nu_x correlation (covering all flow-regimes of saturated flow boiling or flow condensation in Figs. 1 and 2) given in the form of Eq. (11), or its equivalent, and subject to initial condition.

$$X(0) = \begin{cases} 0, & \text{for saturated flow} - \text{boiling} \\ 1, & \text{for saturated flow} - \text{condensation} \end{cases} \tag{25}$$

For a known heat-flux value specifying the "method of heating/cooling," the ODE in Eq. (24) yields linear $X(\hat{x})$ variation if it is solved for a uniform heat-flux prescription (i.e., for $\Psi_q(x) \approx 1$) – over $0 \leq \hat{x} \leq L/D_h$ subject to the initial conditions in Eq. (25). If the overall Nu_x correlation in Eq. (12) (or its equivalent) is known, it allows evaluation of h_x given values of $\overline{q}''_w$, Bl, and computed $X(\hat{x})$ variations. The use of this h_x in the defining relationship of Eq. (4) then yields the temperatures $T_w(x)$ over $0 \leq x \leq L$.

A more interesting and a relatively difficult case is when the Nu_x correlation is available from known heat-flux-based measurements and associated correlations in the form of Eq. (12) – as in the example given later on in Sect. 3.1.1 – and one wants to use/solve Eq. (23) to make $X(x)$ and $q''_w(x)$ predictions for a known wall temperature $T_w(x)$ case. In this case, preliminary reasonable guesses of $\overline{q}''_w$ and $\Psi_q(x) \cong 1$ are employed to express Nu_x in Eq. (12) as a function of quality X for use in the solution of Eq. (23). The solution of Eq. (23) yields associated $X(x)$ variations. These new $X(x)$ variations are used in Eq. (12) and Eq. (24) to obtain $Bl \cdot \Psi_q(x)$ or $q''_w(x)\big|_{new}$. This yields new guesses of $\overline{q}''_w$ and $\Psi_q(x)$ toward iterative evaluation of Nu_x in Eq. (12) as a function of quality X followed by solution of Eq. (23). The process is repeated until converged values of $X(x)$, $\overline{q}''_w$, and $\Psi_q(x)$ are obtained.

2.4.2 Use of Flow-Regime-Specific Nu_x Correlations

Alternatively, for the flow-regime-specific Nu_x correlations given in flow-regime-specific forms of Eq. (20) or Eq. (21) along with known wall temperature "method of heating/cooling" cases, the related nonlinear ODE in Eq. (23) – with or without the need for combining it with Eq. (24) – may be solved over $x_i^* \le x \le x_{i+1}^*$; the distances over which flow-regime "i" is realized. The initial condition for these flow-regime-specific solutions of X(x), for a guessed value of x_i^*, then becomes:

$$X\left(x_i^*\right) = X_{cr|(i-1)\to i} \tag{26}$$

where the $X_{cr|(i-1)\to i}$ correlation is available from Eq. (18) and the guessed value of x_i^* remains unknown until X(x) is obtained from $x = 0$ up to $X\left(x_i^*\right)$, through similar considerations of all the prior flow-regimes.

Current knowledge of segmented and flow-regime-specific Nu_x correlations may be approximate and reasonable for annular flow realizations, but the knowledge of the flow-regime boundaries, as sought in nondimensional forms (such as Eqs. (17) and (18)), is poor for the flows in Fig. 4. The flow-regime transition boundaries, which occur for flows in Figs. 1, 2, and 3, are also poorly known.

Alternatively for cases where "method of heating/cooling" is specified by known heat-flux values specifying the cases and a reasonable flow-regime-specific Nu_x correlation is available (as in Eq. (20)), the solution of the ODE in Eq. (24) over $x_i^* \le x \le x_{i+1}^*$ may be obtained – and $X(\hat{x})$ will vary linearly with $\hat{x}$ for the initial assumption of $\Psi_q(x) \approx 1$. With the help of the initial condition in Eq. (26) and "regime-i"-specific Nu_x correlation in Eq. (20), h_x can be evaluated for given values of $\overline{q}_w''$, Bl, and $X(\hat{x})$ variation. The use of this h_x in the defining relationship of Eq. (4) then yields temperatures $T_w(x)$ over the x-locations $x_i^* \le x \le x_{i+1}^*$ for regime-i. The ability to correctly place the physical x-location of this "regime-i" at a suitable distance form is possible only if one knows the $x = x_i^*$ location in Eq. (26) through similar considerations of all the prior flow-regimes between $x = 0$ and $x = x_i^*$.

3 Overview of Available Correlations for Direct and Indirect Variables of Interest

The correlations that are relevant to the focus of this review – annular flow boiling and flow condensation – correspond typically to laminar liquid film flows, laminar or turbulent vapor flows, and negligible entrainment rates. These correlations (for heat transfer coefficient and pressure-drop, etc.) are related to key variables (dimensional or nondimensional) that define a specific flow realization, namely, hydraulic diameter D_h, mass-flux G, relevant fluid properties, imposed heat-flux $\overline{q}_w''$ or wall temperature $\overline{T}_w$, length L, quality X, and inlet quality X_{in} (for annular flow boiling only) in the horizontal tube configuration of the flows in Figs. 1, 2, and 3. Though horizontal tube considerations are sufficient for most inner diameters D_h and mass-flux G values of interest to this review, downward tilted ($g_x > 0$) flow-boilers and

flow-condensers for some macroscale diameters (5 mm $\leq D_h \leq$ 15 mm) and low mean mass-flux (G = 10 to 30 kg/m^2 . s) may also be of interest and are briefly discussed here.

Effects of nonuniform heating/cooling methods have been discussed by Naik et al. (2016), Naik and Narain (2016), and Ranga Prasad et al. (2017) from a theoretical point of view. Regardless of whether the correlations assume knowledge of wall temperature $T_w(x)$ or heat-flux $q''_w(x)$ prescriptions, one can establish (with the help of CFD simulations) equivalence between the two prescriptions (see Naik et al. 2016 and Ranga Prasad et al. 2017) for convective boiling and flow condensation.

Next, relevant correlations for heat transfer coefficient h_x, flow-regime maps, pressure-drop, and void fraction are reviewed. Furthermore, additional available information on CHF issues (for flow boiling) as discussed in Sect. 2.2 and related to the annular flows in Figs. 1, 2, and 3 are also discussed.

3.1 Local Heat Transfer Coefficient h_x from Nusselt Number Nu_x Correlations

3.1.1 Flow Boiling

Known results from the flow-boiling experiments that are cited here typically use the fact that the mean wall heat-flux $\overline{q}''_w$ and key flow defining variables are known, and Nu_x, for traditional boiling operations, can be correlated in the structural form (or its equivalent) indicated in Eq. (12).

Several local heat transfer coefficient correlations covering a range of experiments (in mini-/micro-channels for both single and multi-channel configurations, as given in Table 1) have been recently considered by Kim and Mudawar (2013c), and an order of magnitude curve fit for flow boiling – covering all the flow-regimes in Fig. 1 – has been proposed. Though these experiments, and hence associated correlations, also cover the annular regime results, which are of particular interest to this review, the experimental data underlying the correlations' data are more biased toward regimes marked I–III in Fig. 1b.

The "more general" HTC correlation of Kim and Mudawar (2013c) – given in Eqs. (27), (28), (29), and (30) below – has a built in, but ad hoc, breakup of total HTC into its *nucleate* and *convective* components:

$$h_x = \left(h_{x|nb}^2 + h_{x|cb}^2\right)^{0.5} \tag{27}$$

where,

$$h_{x|nb} \equiv \left[2345\left(Bl\frac{P_H}{P_F}\right)^{0.7} P_R^{0.38}(1-X)^{-0.51}\right]\left(0.023 Re_L^{0.8} Pr_L^{0.4}\frac{k_L}{D_h}\right) \tag{28}$$

and

Table 1 Previous saturated flow-boiling heat transfer correlations or experimental data considered by Kim and Mudawar (2013c). The parenthetical notation (V/V-u/V-d, H; C/R) under "Remarks," respectively, represent considered flow directions (V vertical-up or vertical-down not stated, V-u vertical-up, V-d vertical-down, H horizontal) and following the semicolon (C/R), respectively, represent considered cross-sections (C circular and/or R rectangular)

Authors	Remarks
Recommended for macro-channels	
Cooper (1984b)[a]	6000 data points for nucleate pool boiling
Gungor and Winterton (1986)	D = 2.95–32 mm, water, R11, R12, R113, R114, R22, ethylene glycol, 4300 data points – (V-u, V-d, H; C)
Liu and Winterton (1991)	Same data as Gungor and Winterton (1986) – (V, H; C)
Shah (1982)	Experiments are mostly in horizontal tubes of circular or rectangular cross-sections D = 6–25.4 mm, water, R11, R12, R113, cyclohexane, 780 data points – (V, H; C)
Recommended for mini/micro-channels	
Agostini and Bontemps (2005)	D_h = 2.01 mm, 11 parallel channels, R134a – (V-u; R)
Bertsch et al. (2009)	D_h = 0.16–3.1 m, water, refrigerants, FC-77, nitrogen, 3899 data points– (V, H; C, R)
Ducoulombier et al. (2011)	D = 0.529 mm, CO_2 – (H; C)
Lazarek and Black (1982)	D = 3.15 mm, R113, nucleate boiling dominant – (V; C)
Li and Wu (2010)	D_h = 0.16–3.1 m, water, refrigerants, FC-72, ethanol, propane, CO_2, 3744 data points – (V, H; C, R)
Oh and Son (2011)	D = 1.77, 3.36, 5.35 mm, R134a, R22 – (H; C)
Tran et al. (1996)	D = 2.46, 2.92 mm, D_h= 2.40 mm, R12, R113, nucleate boiling dominant – (H; C,R)
Warrier et al. (2002)	D_h = 0.75 mm, 5 parallel channels, FC-84 – (H; R)
Yu et al. (2002)	D = 2.98 mm, water, ethylene glycol, nucleate boiling dominant – (H; C)

[a]The Cooper (1984b) correlation was developed for nucleate pool boiling

$$h_{x|cb} \equiv \left[5.2\left(Bl\frac{P_H}{P_F}\right)^{0.08} We_{L0}^{-0.54} + 3.5\left(\frac{1}{\tilde{X}_{tt}}\right)^{0.94}\left(\frac{\rho_V}{\rho_L}\right)^{0.25}\right]\left(0.023 Re_L^{0.8} Pr_L^{0.4}\frac{k_L}{D_h}\right) \tag{29}$$

The parameters in the above definitions of h_x are:

$$Bl \equiv \frac{\overline{q}_w''}{G.h_{fg}}, P_R = \frac{p_o}{p_{cr}}, Re_L \equiv \frac{G(1-X)D_h}{\mu_L}, Re_{L0} \equiv \frac{GD_h}{\mu_l}, Pr_L \equiv \frac{\mu_L C_{pL}}{k_L},$$
$$We_{L0} \equiv \frac{G^2 D_h}{\rho_L \sigma}, \tilde{X}_{tt} = \left(\frac{\mu_L}{\mu_V}\right)^{0.1}\left(\frac{1-X}{X}\right)^{0.9}\left(\frac{\rho_V}{\rho_L}\right)^{0.5} \tag{30}$$

where P_F is the wetted perimeter (in case a tube/channel is not wetted on all its periphery P) and P_H is the heated perimeter (and includes cases for which a tube/

channel is not heated on all its periphery). This is also the perimeter where $q_w''(x)$ is replaced by $\overline{q}_w''$.

The correlation in Eqs. (27), (28), (29), and (30) covers all the saturated flow-boiling regimes depicted in Fig. 1, i.e., as the quality X increases and the flow goes from tube diameter determined nucleate boiling (nb) dominated zone I to the macroscale convective boiling (cb) controlled regime III. The use of the Martinelli parameter $\widetilde{X}_{tt}$ in Eq. (29) is typically not indicative of both phases being turbulent – it is simply a correlation parameter. The uncertainty in the predictions from a correlation, such as the one in Eqs. (27), (28), (29), and (30), can be high as it allows for many experimental and conceptual uncertainties. Some of the significant sources of uncertainty are associated with:

(i) Replacing $X(x) = \dot{M}_v(x)/\dot{M}_{in}$ inferred from the expression of $X(x) \cong X_{th}(x)$ where $X_{th}(x)$ is a thermodynamic vapor quality obtained from experimentally assessing (with some uncertainty) an "$x = 0$" location where the fluid is at close to saturation conditions. And then applying energy balance to the flow-boiling control volume, between the identified "$x = 0$" location and one at an "$x > 0$" location, with knowledge of the experimentally measured values (with its own uncertainties) of heat input ($q_{[0,x]} = \int_0^x q_w''(x).P_H.dx$) between the two locations.

(ii) Uncertainties in measuring $\Delta T(x)$ ($\equiv |T_w(x) - T_{sat}(p_0)|$) and $q_w''(x)$ (due to the limitations in accuracy of thermocouple and other instruments – more so with older experiments with less accurate sensors) and then evaluating $h_x \equiv q_w''(x)/\Delta T(x)$. This error is also related to occasional assumption, without verification, that the wall temperature $T_w(x)$ is nearly uniform and one can replace $\Delta T(x)$ by the average temperature difference ΔT.

(iii) Uncertainties associated with the current practice of combining data obtained for different cross-sectional geometries, e.g., from channel flows (i.e., high aspect ratio rectangular cross-sections) not significantly influenced by curvature effects on the flow field as well as surface tension effects with those obtained from mm-scale tubes, where the flow, interfacial shear, and interfacial pressure differences are affected by curvatures and surface tension effects. Similarly, significant uncertainties arise from combining data from experiments conducted at different tube inclinations – particularly data for low to moderate mass-flux G values.

(iv) There are inherent curve-fitting inaccuracies associated with developing a single correlation that cover all the flow-regimes (as in Eqs. (11) and (12)) as opposed to developing segmented correlations specific to different flow-regimes (as in Eq. (20)).

(v) A rather *ad hoc* splitting of total HTC h_x in its macroscale convective ($h_{x|cb}$) and macroscale nucleate ($h_{x|nb}$) boiling parts (see Sect. 6, Ranga Prasad et al. 2017, and Gorgitrattanagul 2017).

Despite the aforementioned uncertainties and weaknesses, correlations – such as the one in Eqs. (27), (28), (29), and (30) – can provide useful order of magnitude

estimates until more accurate flow-regime and flow-physics specific correlations are developed in appropriately classified ranges of parameter space of interest to the user. For design purposes, as in the sample example of Sect. 4, one can use a range of estimates based on the results in Eqs. (27), (28), (29), and (30). A crude estimate of uncertainty of the correlation in Eqs. (27), (28), (29), and (30) is

$$0.5h_{x|\text{Eq (27)}-(30)} \le h_x \le 2h_{x|\text{Eq (27)}-(30)} \tag{31}$$

Correlation of Kim and Mudawar (2013c) in Eqs. (27), (28), (29), and (30) also covers annular flows – involving both laminar and turbulent flows of the vapor and the liquid phases. Direct numerical simulation (DNS) approach (see Sect. 5 for further discussions) has been recently used by Ranga Prasad et al. (2017) to propose local heat transfer coefficient ($h_{x|cb}$) correlations for annular boiling cases over the length of the boiler (Fig. 3a) – but the cases were limited to sufficiently thin and *laminar* liquid film flows and *laminar-to-turbulent* vapor flows. Such $h_{x|cb}$ values, particularly after its semi-theoretical extension to cover laminar liquid film flows and full range of turbulent vapor flows, can be effectively combined with experimental h_x values for annular flow boiling, and this will yield superior estimate of microscale nucleate boiling contributions, where $h_{x|nb} = h_{x|nb\ -\ micro}$ – as is expected for region III and part of region IV in Fig. 1b (see Sect. 6 for further considerations and uses of this aspect of annular flows).

A sample correlation, for low values of imposed heat-flux $q''_w(x)$ as well as low mass-flux G values, is obtained by CFD solutions, and their correlation is presented in Ranga Prasad et al. (2017) for channel flows (of gap "h" and a reference length scale of "h" changed here to $\widetilde{D}_h = 4h$) – with CFD employing laminar liquid and laminar vapor assumptions but the resulting heat transfer correlations (given in Eq. (32) below) continuing to apply to moderately turbulent vapor phases as well ($Re_V < 40{,}000$). The correlation provided in Ranga Prasad et al. (2017) is for "method of heating" specified by known wall temperatures, with the considered/specific parameter space corresponding to flow situations in Table 2, and is given by:

$$\frac{h_{x|cb}\cdot\widetilde{D}_h}{k_L} = 21.46^{*}X^{1.61}X_{in}^{0.128}Re_T^{0.0284}\left(\frac{Ja}{Pr_L}\right)^{-0.0583}\left(\frac{\rho_V}{\rho_L}\right)^{-0.399}\left(\frac{\mu_V}{\mu_L}\right)^{0.454} \tag{32}$$

Table 2 Ranges of raw variables and fluid flow conditions considered for the development of the correlation given in Eq. (32)

Working fluids	FC-72	R113	R123
Inlet pressure, p_0 (kPa)	105.1	105.1–200	105.1
Channel height, h (mm)	2	2	2
Mass flux, G ($\equiv\rho_V U$) (kg/m^{2}s)	7–35	3.8–56.3	3.4–26.8
Transverse gravity, g_y (m/s^2)	−9.81	−9.81	−9.81
Average inlet vapor speed, U (m/s)	0.5–2.5	0.5–4	0.5–4
Temperature difference, ΔT (°C)	5–25	5–25	5–25

where, $0.5 \le X_{in} \le 0.86$, $2466 \le Re_T \le 39{,}524$, $0.0048 \le Ja/Pr_L \le 0.0424$, $0.00466 \le \rho_V/\rho_L \le 0.0097$, $0.0216 \le \mu_V/\mu_L \le 0.0295$.

Correlations such as Eq. (32) can also be developed with the help of simulations for low heat-flux $q_w^{''}(x)$ and mass-flux G values for cases where "method of heating" is specified by known heat-flux values. These issues, along with forthcoming methodologies for obtaining $h_{x|cb}$ for a higher range of $q_w^{''}(x)$ and G values – typically associated with laminar liquid and turbulent vapor flows in Fig. 3 – are also discussed in Ranga Prasad et al. (2017) and Gorgitrattanagul (2017). For such cases, vapor flows can be laminar or turbulent, and thin liquid film flows can be controlled to be in the laminar regime (at least for devices in Fig. 3); the forthcoming semi-empirical CFD approaches cannot only yield reliable $h_{x|cb}$ correlations for a higher range of G and other parameters, but they can also be supplemented with experimental measurement-based correlations for the total HTC h_x values – in the expected presence of significant microscale nucleate boiling contributions $h_{x|nb\ -\ micro}$ (region III of Fig. 1b) through an $n = 1$ relation in Eq. (33) below. Thus, following the superposition approach in Eq. (33), one can also propose annular flow-boiling correlations in the presence of microscale nucleate boiling. Such correlation proposals – which employ $n = 1$ (Eq. (33)) – are being studied for compatibility with experiments dealing with the flow in Fig. 3a (Gorgitrattanagul 2017; Sepahyar 2018) and are expected to be compared with results obtained from other available correlations of the following approximate forms:

$$h_x = \left(\left(h_{x|nb}\right)^n + \left(h_{x|cb}\right)^n\right)^{1/n}, n = 1, 2, 3, \ldots \tag{33}$$

Here $n = 1$ is preferred if $h_{x|cb}$ is given by the direct suppressed nucleation assumption-based CFD approaches, similar to the one leading to Eq. (32). A variation of $n = 1$ approach – such as those of Chen (1966), Kenning and Cooper (1989), and Gungor and Winterton (1986) – takes a suitable $h_{x|cb}$ empirical correlation (typically for region III in Fig. 1b) and adds it to a suitable macroscale $h_{x|nb}$ correlation (after multiplying it by a suppression factor $S < 1$) for pool boiling regimes – this is typically done for both vertical and horizontal in-tube flow-boiling operations in regions I and II of Fig. 1b. These authors often employ a pool-boiling correlation for $h_{x|nb}$. Lately pool-boiling correlations of Cooper (1984a), or Cooper (1984b), or Gorenflo (1993) are preferred over the earlier Forster and Zuber (1955) correlation, although their relative merits depend on many factors – even for pool boiling (see Jones et al. 2009). The popular Cooper (1984b) correlation is given by:

$$h_{x|nb} = C^* P_R^{(0.12-0.2\cdot\log_{10}R_a)} * \left(-\log_{10}P_R\right)^{-0.55} M^{-0.5} \left(q_w^{''}\right)^{0.67} \tag{34}$$

where P_R is the reduced pressure as defined in Eq. (30), M is the molecular weight of the working fluid in kg/kmol, heat-flux is measured in W/m^2, R_a is a specific roughness measure in μm divided by 1 μm, and although C is fluid-solid pair specific – often $C \cong 55(kg/kmol)^{0.5} \cdot (W/m^2)^{-0.67} \cdot (W/m^{2^\circ}C)$ is recommended if specific information is not available.

It should be reiterated that the use of the separate terms $h_{x|cb}$ and $h_{x|nb}$ in Eq. (33) – through popular correlations such as Cooper (1984b) – only focuses on how macro-nucleation effects in regions I–II of Fig. 1b become subservient to the controlling dominance of $h_{x|cb}$ in region III of Fig. 1b. However, the focus of this chapter is on thin film (about 300–200 μm thick) annular flow-boiling devices of Fig. 3 – where micro-nucleation effects of $h_{x|nb\ -\ micro}$ needs to be more specifically modeled (for regions III-IV of Fig. 1b) in the decomposition of the local HTC h_x through $h_{x|nb} = h_{x|nb-micro}$, $h_{x|cb} = h_{x|cb-ann}$, and $h_x = h_{x|nb-micro} + h_{x|cb-ann}$.

3.1.2 Flow Condensation

Known results from flow-condensation experiments that are cited here assume that the mean wall temperature $\overline{T}_w$ along with some key problem defining variables are known and Nu_x values that can be correlated in the structural form (or its equivalent) indicated in Eq. (11).

Table 3 shows several "local" heat transfer coefficient h_x correlations (that included consideration of annular regime in the flow-condensation experiments from which data were used) considered by Kim and Mudawar (2013a) before they

Table 3 Previous annular flow-condensation heat transfer correlations or data considered by Kim and Mudawar (2013a) involved experiments that employed macro- and mini-/micro hydraulic diameter straight ducts of circular and rectangular cross-sections - and experienced annular flows as the dominant flow-regime. The parenthetical notation (V/V-u/V-d, H; C/R) under "Remarks," respectively, represents considered flow directions (V vertical-up or vertical-down not stated, V-u vertical-up, V-d vertical-down, H horizontal) and following the semicolon (C/R), respectively, represent considered cross-sections (C circular and/or R rectangular)

Author (s)	Remarks
Recommended for macro-channels	
Akers and Rosson (1960)	D = 19.05 mm R12, propane $re_V \left(\frac{\mu_V}{\mu_L}\right)\left(\frac{\rho_L}{\rho_V}\right)^{0.5} > 20,000, \quad re_L > 5000$ – (H; C)
Cavallini and Zecchin (1974)	R12, R22, R113, $7000 \le re_{LO} \le 53{,}000$ – (V; C)
Dobson and Chato (1998)	D = 3.14–7.04 mm; R12, R22, R134a, R32/R125 – (H; C)
Haraguchi et al. (1994)	D = 8.4 mm; R22, R123, R134a – (H; C)
Moser et al. (1998)	D = 3.14–20 mm; R11, R12, R125, R22, R134a, R410a – (H; C)
Shah (1982)	D = 7–40 mm; water, R11, R12, R22, R113, methanol, ethanol, benzene, toluene, trichloroethylene (V, H, I; C)
Recommended for micro-channels	
Bohdal et al. (2011)	D = 0.31–3.30 mm; R134a, R404a – (H; R)
Huang et al. (2010)	D = 1.6, 4.18 mm; R410a, R410a/oil – (H; C)
Koyama et al. (2003)	D_h= 1.46 mm; R134a; multi-channel – (H; C)
Park et al. (2011)	D_h= 1.45 mm; R134a, R236fa, R1234ze (E); multi-channel – (V-d; R)
Wang et al. (2002)	D_h= 1.46 mm; R134a; multi-channel – (H, R)

The experiments mostly employ straight ducts and annular flows are the dominant flow-regimes. Both circular and rectangular cross-section ducts have been considered.

proposed their own order of magnitude curve fit correlation given below in Eqs. (35), (36), (37), and (38):

$$Nu_x \equiv \frac{h_x D_h}{k_L} = 0.048 Re_L^{0.69} Pr_L^{0.34} \left(\frac{\Phi_g}{\widetilde{X}_{tt}} \right) \tag{35}$$

where $\widetilde{X}_{tt}$, turbulent-turbulent Lockhart-Martinelli parameter, is used merely as a known function and defined as:

$$\widetilde{X}_{tt} = \left(\frac{\mu_L}{\mu_V} \right)^{0.1} \left(\frac{1 - X}{X} \right)^{0.9} \left(\frac{\rho_V}{\rho_L} \right)^{0.5} \tag{36}$$

The parameter Φ_g in Eq. (35) is the two-phase multiplier defined as:

$$\Phi_g^2 = 1 + CX_m + X_m^2 \tag{37}$$

where C is a Lockhart-Martinelli coefficient defined in Kim and Mudawar (2013a) and in Table 6a of this review and X_m is a Lockhart-Martinelli parameter defined as:

$$X_m = \left[\frac{(dp/dx)_L}{(dp/dx)_V} \right]^{1/2}$$

where $(dp/dx)_L$ and $(dp/dx)_V$ represent the frictional pressure gradients of liquid and vapor phases, respectively, flowing alone in the pipe and are computed using the following equations:

$$\begin{aligned} \left(\tfrac{dp}{dx}\right)_L &\equiv \frac{-2 f_L G^2 (1 - X)^2}{\rho_L D} & Re_L &\equiv \frac{G(1 - X)D}{\mu_L} \\ \left(\tfrac{dp}{dx}\right)_V &\equiv \frac{-2 f_V G^2 X^2}{\rho_V D} & Re_V &\equiv \frac{GXD}{\mu_V} \\ f_L &= B Re_L^{-n} & f_V &= B Re_V^{-n} \end{aligned} \tag{38}$$

The friction factor f_L and f_V are defined as above for vapor and liquid phases, with laminar flows' ($Re_{L/V} < 2000$) values of $B = 16$ and $n = 1$ and turbulent flows' ($Re_{L/V} > 2000$) values of $B = 0.0079$ and $n = 0.25$.

Computational fluid dynamics (CFD) which becomes a direct numerical simulation (DNS) approach for laminar/laminar case has been recently used by Narain et al. (2015), Naik et al. (2016), and Naik and Narain (2016) (also see Sect. 5 for further discussions) to propose local heat transfer coefficient h_x correlations for annular flow-condensation cases (Fig. 3b) that involve sufficiently thin laminar liquid flows and low values of both heat-flux $q_w''(x)$ and mass-flux G.

A sample Nu_x correlation, presented in Eq. (39) below, is for laminar/laminar channel flows (of gap "h" and reference length $\widetilde{D}_h = 4$ h), and its validity range extends to reasonably turbulent vapor phases ($Re_V < 40{,}000$) as well. The

Table 4 Range of raw fluid variables and flow conditions considered for the development of the correlation given in Eq. (39)

Working fluids	FC 72	R113	R113	R134a
Inlet pressure (kPa)	100	25	225	150
Saturation temperature (°C)	55.94	11.1	73.86	−17.15
Hydraulic diameter (h = 0.001–0.003 m in Fig. 3b)	4 h	4 h	4 h	4 h
Transverse gravity, g_y (m/s^2)	$0 \le \lvert g_y \rvert \le g$	$0 \le \lvert g_y \rvert \le g$	$0 \le \lvert g_y \rvert \le g$	$0 \le \lvert g_y \rvert \le g$
Mass flux, G (kg/m^2s)	4.55–127.4	4.2–115.3	5.51–154.1	4.1–113.5
Temperature difference, ΔT (°C)	2.93–12.30	8.69–36.50	2.25–9.45	3.45–14.45

correlation is for "method of cooling" specified by known wall temperatures, with the parameter space restrictions given below, immediately following Eq. (39):

$$\frac{h_x.\widetilde{D}_h}{k_L} \equiv Nu_x\Big|_{\widetilde{D}_h} = 0.02^*(1-X)^{-0.59}Re_T^{0.122}\left(\frac{Ja}{Pr_L}\right)^{0.3}\left(\frac{\rho_V}{\rho_L}\right)^{-0.73}\left(\frac{\mu_V}{\mu_L}\right)^{0.069} \quad (39)$$

where $3200 \le Re_{in} \le 92{,}000$, $0.0058 \le Ja/Pr_L \le 0.021$, $0.0013 \le \rho_V/\rho_L \le 0.011$, and $0.012 \le \mu_V/\mu_L \le 0.034$. These parameter restrictions arose from considering the range of flow conditions given in Table 4.

It was shown by Narain et al. (2015) that, for low heat-flux $\overline{q}''_w$ and mass-flux G cases, the channel flow DNS yields h_x values much higher than the corresponding predictions from the Kim and Mudawar correlation in Eqs. (35), (36), (37), and (38). The in-tube (as opposed to channel) shear-dominated condensing flow predictions for h_x from Naik et al. (2016) and Naik and Narain (2016) yield values closer to the one in Kim and Mudawar (2013a), whereas the channel predictions yield much higher values. This suggests that high curvature effects associated with mm-scale in-tube flows may degrade the heat transfer performance relative to condensing flows in channels (i.e., high aspect ratio rectangular cross-sectional ducts).

As discussed in Sect. 5 of this review, the CFD/DNS approach can be extended to yield reliable h_x values for a higher range of parameters (particularly mass-flux G values, etc.) than those indicated in Table 4.

3.2 Flow-Regime Maps/Correlations

Flow-regime maps are needed, and recommendations exist (see Ghiaasiaan 2007; Kim and Mudawar 2013a) for identifying flow-regimes associated with traditional operations of boiling (Fig. 1) and condensing (Fig. 2) flows.

3.2.1 Annular Adiabatic Cases

Flow-regime maps also exist for adiabatic flows (Carey 1992; Ghiaasiaan 2007) which may also be applicable and useful in the inlet region, just past the splitter

plates in the innovative annular operations shown in Fig. 3. In this region, the flow behavior will approach adiabatic flows because it would not have been exposed to significant amounts of externally imposed heating/cooling (see Fig. 3).

Precise nondimensional transition maps, as suggested by correlations of the type indicated in Eqs. (17) and (18), currently do not exist – even for adiabatic two-phase flows. For the adiabatic case, following certain earlier larger diameter (>5 mm) studies (Baker 1953; Hewitt and Roberts 1969), a map employing raw variables was proposed by Mandhane et al. (1974). This map uses superficial velocities of vapor and liquid phases but covers a significant range of the parameter space, which includes conditions of interest to this review (i.e., millimeter-scale horizontal ducts with cocurrent flows).

3.2.2 Annular Flow Boiling

This regime is of primary interest here (Fig. 3a), and it occurs at locations further downstream of the plug-slug regime as quality X increases in the traditional saturated flow-boiling cases (Fig. 1). For known uniform heat-flux values specifying the "method of heating," Harirchian and Garimella (2012) recommended the following criteria for micron-scale D_h:

$$\begin{aligned} &Bo^{-0.5}.\widetilde{Re} > 160 \\ &Bl \bullet \frac{X.P_H}{D^2}.\frac{\rho_L - \rho_V}{\rho_V} > 96.65\left(Bo^{0.5}\widetilde{Re}\right)^{-0.258} \end{aligned} \tag{40}$$

where P_H = heated perimeter, $D \equiv \sqrt{A}$, $Bo \equiv g(\rho_L - \rho_V)D^2/\sigma$, Bl is as defined in Eq. (9), and $\widetilde{Re} \equiv G.D/\mu_L$. They assume heating levels and flow rates as discussed for Fig. 1 realizations, and therefore annular flows are expected only over downstream distances "x" satisfying:

$$x > x_A \equiv 96.65\left(Bo^{0.5}\widetilde{Re}\right)^{-0.258} Bl^{-1}\frac{\rho_V}{\rho_L - \rho_V}\frac{A}{P_H} \tag{41}$$

or quality X satisfying:

$$X > X_{cr} = X(x = x_A) \tag{42}$$

where X (x) has been obtained from the approach described in Sect. 2.4 along with use of an appropriate Nu_x correlation, such as the one in Eqs. (27), (28), (29), and (30), and estimates being approximate (as in Eq. (31)). The parameter ranges for validity of Eq. (41) are as given in Harirchian and Garimella (2012), but it does not include sufficient experimental data (even in nondimensional terms) that would cover the larger mm-scale D_h values of interest to this review. For identifying critical transition quality for annular flow boiling, Kim and Mudawar (2013a) also recommend another criterion. This criterion is similar to the one for flow condensation and, therefore, is described instead in Sect. 3.2.3. The effectiveness of these empirical

correlations is limited and may provide only some order of magnitude estimates. More accurate, nonlinear stability analysis based transition quality (plug-slug to annular) correlations for Eqs. (17) and (18) can also be obtained by a synthesis of CFD/DNS approach (see Ranga Prasad et al. 2017) and new especially designed experiments – but such estimates are currently limited to low mass-flux and heat-flux cases of annular flow boiling in channels under hypothetical pure convective boiling scenarios (i.e., suppressed nucleation cases - real or assumed, as in Eq. (32)).

3.2.3 Annular Flow Condensation

This regime is of interest here (Fig. 3b), and it occurs upstream of the slug and plug regimes (Fig. 2), as quality X decreases, in traditional flow-condenser operations. For "method of cooling" being specified by known/assumed wall temperatures, Kim and Mudawar (2013a) recommend the following criteria:

$$We^* > 7.\widetilde{X}_{tt}^{0.2} \tag{43}$$

where $\widetilde{X}_{tt}$ is as defined in Eq. (30) (or Eq. (36)) and:

$$We^* \equiv \frac{2.45Re_V(x)^{0.64}}{Su_{vo}^{0.3}\left(1+1.09\widetilde{X}_{tt}^{0.039}\right)^{0.4}} \text{ for } Re_L(x) \le 1250 \tag{44}$$

or

$$We^* \equiv \frac{0.85Re_v\widetilde{X}_{tt}^{0.157}}{Su_{vo}^{0.3}\left(1+1.09\widetilde{X}_{tt}^{0.039}\right)^{0.4}}\left[\left(\frac{\mu_V}{\mu_L}\right)^2\left(\frac{\rho_L}{\rho_V}\right)\right]^{0.084} \text{ for } Re_L(x) > 1250 \tag{45}$$

Note that in Eqs. (43), (44), and (45), $Su_{VO} \equiv \rho_V \sigma D_h/\mu_V^2$, and the range of parameter space for these correlations is as given in Kim and Mudawar (2013a). By plotting the above criteria on an $X - Re_T$ plane, the results in Eqs. (43), (44), and (45) can be presented in the form of Eq. (17). Again, effectiveness of the above-described type of correlations is expected to be limited and, at best, is meant only to provide order of magnitude estimates for circular and rectangular cross-sections (of aspect ratio near unity) tubes. For specific fluids and parameter ranges (inlet pressure, etc.), the correlations in Eqs. (43), (44), and (45) can be compared with flow-regime maps of Coleman and Garimella (2003), etc. For low mass fluxes (G) and channel flow condensation in Fig. 3b (aspect ratio ~ 0), the correlation in Eqs. (43), (44), and (45) can even be compared with accurate nonlinear stability-based transition quality (annular to plug-slug) correlation given by Naik et al. (2016) and Naik and Narain (2016).

The correlation proposed by Naik et al. (2016) and Naik and Narain (2016) for flow condensation in a channel yields the distance from $x = 0$ (where $X(0) = 1$) to the onset of plug-slug regime ($x = x_{A|lg}$) in the horizontal channel flow configurations of Fig. 3b. Replacing D_h by $\widetilde{D}_h = 4h$ (instead of "h" used as characteristic

length in Naik et al. 2016 and Naik and Narain 2016), it is recalled here that (see Narain et al. 2015):

$$\hat{x}_A|_{lg} \cong 0.237\,(Re_T)^{0.85}\left(\frac{Ja}{Pr_L}\right)^{-2.17}.\left(\frac{\rho_V}{\rho_L}\right)^{1.03}.\left(\frac{\mu_V}{\mu_L}\right)^{1.64} \tag{46}$$

and

$$X_{cr} = X(\hat{x})|_{\hat{x}=\hat{x}_A|_{lg}} \cong 1 - \left(5.41{\cdot}\hat{x}|^{0.73}_{\hat{x}=\hat{x}_A|_{lg}}\,(Re_T)^{-0.64}\left(\frac{Ja}{Pr_L}\right)^{1.02}.\left(\frac{\rho_V}{\rho_L}\right)^{-0.33}.\left(\frac{\mu_V}{\mu_L}\right)^{-0.86}\right) \tag{47}$$

The parameter ranges over which Eqs. (46) and (47) are valid are the same as the ones given for Eq. (39). These low heat and mass-flux parameter ranges are more limited than the ones given in Kim and Mudawar (2013a) for Eq. (43). There is an order of magnitude agreement in the flow-regime transition boundaries obtained from Eqs. (43), (46), and (47), (see Narain et al. 2015) for $16{,}000 \leq Re_T \leq 32{,}000$. Note that there is no surface-tension dependence in Eqs. (46) and (47) for modest mass-flux thin-film annular flows (unlike Suratman number Su_{VO} dependence in Eqs. (43), (44), and (45)), and this is consistent with the specific physics of channel flows. Eq. (43), being a curve fit, loses accuracy but gains in the parameter space ranges over which order of magnitude estimates are valid.

3.3 Void Fraction (ϵ) and Quality (X) Correlations

Void fraction (ϵ) can be defined "locally" (Carey 1992; Ghiaasiaan 2007), i.e., as a variable whose value depends on the location of a point and the instant of time in a given two-phase flow field. However, for the "steady-in-the-mean" in-tube flows of interest (such as the ones in Figs. 1, 2, and 3), void fraction ϵ definition simplifies (Ghiaasiaan 2007) to:

$$\epsilon \equiv \frac{A_V(x)}{A} \tag{48}$$

where $A_V(x)$ is the cross-sectional area occupied by the gas phase at any location "x" (see Figs. 1, 2, and 3) for two-phase flows in a tube of cross-sectional area "A."

It is expected that dependence of void fraction ϵ, on quality $X(x)\left(\equiv \dot{M}_V(x)/\dot{M}_{in}\right)$, density ratio ρ_V/ρ_L, viscosity ratio μ_V/μ_L, etc., need to be correlated. This is important in assessing the significance of *actual* mean gas-phase speed $U_V(x)$ and the mean liquid-phase speed $U_L(x)$ – as opposed to uniform *superficial* speeds (Carey 1992) $j_V \equiv G/\rho_V$ and $j_L \equiv G/\rho_L$. This is because $U_V(x) \equiv \dot{M}_V(x)/(\rho_V.A_V(x)) = G.X(x)/(\rho_V.\epsilon(x))$ and $U_L(x) \equiv \dot{M}_L(x)/(\rho_L.A_L(x)) = G.(1 - X(x))/(\rho_L.(1 - \epsilon(x)))$. As a result of this importance, several such correlations have been developed and are used in developing correlations for total pressure gradient $\left(-\frac{\partial p}{\partial x}\right)_T$, interfacial shear

correlations, film thickness correlations, and heat transfer rate correlations for high mass-flux annular flows (Cavallini et al. 2006; Kosky and Staub 1971; Thome 2004). The acceleration component of the total pressure gradient is very important in high heat-flux boiling because $U_V(x)$ rapidly increases with "x" (Kim and Mudawar 2014; Thome 2004).

Most of these void-fraction correlations have been developed by considering adiabatic flows and using various homogeneous, separated, and drift-flux modeling hypotheses (Ghiaasiaan 2007) – suitably correlated for agreement with adiabatic flow experiments in limited contexts. These correlations are not to be taken, however, as ones that model the "physics" of the phase-change flows. For example, for low mass flux laminar/laminar flows in a channel, $\epsilon - X$ relationships can be obtained by a combination of exact analysis or equivalent, DNS, for: annular adiabatic, certain suppressed nucleation annular flow-boiling (see Ranga Prasad et al. 2016), and for annular flow-condensation cases (Naik et al. 2016; Naik and Narain 2016; Narain et al. 2015). The comparisons of exact results for a representative situation (involving $\rho_V/\rho_L = 0.086$, $\mu_V/\mu_L = 0.0235$, $Ja/Pr_L = 0.034$, $Re_T = 4 \,.\, Re_h = 9616$) are plotted in Fig. 7 – along with results from some well-known correlations in literature – on an $\epsilon - X$ plane. Clearly, laminar liquid/laminar vapor nearly exact $\epsilon - X$ relationship of adiabatic flows does not match similar exact CFD-/DNS-based accurately modeled "flow physics" results obtained for flow condensation and flow boiling.

Despite the "physics" issues associated with using $\epsilon - X$ adiabatic correlations for phase-change flows, two such popularly used engineering correlations are also plotted for laminar/laminar situations in Fig. 7. These popular correlations are as follows:

- Zivi (1964):

$$\epsilon = \frac{1}{1 + \frac{1-X}{X}\left(\frac{\rho_v}{\rho_L}\right)^{2/3}} \tag{49}$$

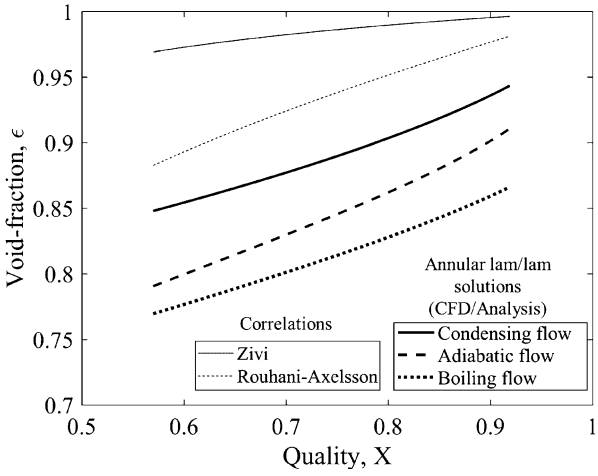

Fig. 7 Comparisons of exact solutions (analytical and computational) for laminar/laminar annular flow – adiabatic flows, flow condensation ($Ja/Pr_L = 0.034$), and flow boiling ($Ja/Pr_L = 0.034$). For order of magnitude comparison purposes, Zivi (1964) and Rouhani and Axelsson (1970) correlations are also plotted for the same parameters ($\rho_V/\rho_L = 0.086$, $\mu_V/\mu_L = 0.0235$, $Re_T = 4 \,.\, Re_h = 9616$)

- Rouhani and Axelsson (1970) (with Steiner 1993 modifications for horizontal tubes):

$$\epsilon = \frac{X}{\rho_V}\left\{[1+0.12(1-X)]\left(\frac{X}{\rho_V}+\frac{1-X}{\rho_L}\right)+\frac{1.18}{G}\left[\frac{g\sigma(\rho_L-\rho_V)}{{\rho_L}^2}\right]^{1/4}(1-X)\right\}^{-1} \tag{50}$$

Besides quality X, adiabatic flow $\epsilon - X$ curve depends on ρ_V/ρ_L, μ_V/μ_L, and Re_T. Condensing and boiling flows additionally depend on Ja/Pr_L (or Bl).

The main value and use of adiabatic flow correlations, such as the ones in Eqs. (49) and (50), for flow boiling and flow condensation are not their ability to capture flow physics. It lies in the fact that their order of magnitude correctness (see, e.g., comparisons in Fig. 7) are used over a large range of parameters (G values, liquid-vapor Reynolds numbers, etc.) that are not currently accessible by proper flow-physics based analyses. Also correlations such as Eqs. (44) and (50) allow development of other "curve fit" correlations for HTC and pressure-drop that cover a similarly large range of parameters in their experimental data – such as those in Kim and Mudawar (2013c) and Kim and Mudawar (2013d).

3.4 Pressure-Drop Correlations

The engineering approach (as opposed to CFD simulations approach) is to use results obtained from an integrated momentum balance (see Carey 1992) for the control volume between any two arbitrary locations "x" and "x + Δx" in Fig. 6 for an *a priori* decomposition of the total pressure gradient $\left(-\frac{\partial p}{\partial x}\right)\Big|_T$ for two-phase flows into three parts (frictional, gravitational, and acceleration/momentum) as:

$$\left(-\frac{\partial p}{\partial x}\right)\Big|_T = \left(-\frac{\partial p}{\partial x}\right)_{fric} + \left(-\frac{\partial p}{\partial x}\right)_g + \left(-\frac{\partial p}{\partial x}\right)_{acc} \tag{51}$$

The subsequent step consists of defining/modeling the three parts on the right side of Eq. (51) separately and then assembling the three terms over the tube length ($0 \le x \le L$) of interest. Denoting the total pressure-drop, or rise, as Δp_T ($\equiv p_{in} - p_{out} = p(0) - p(L)$) – and allowing Δp_T to be negative (as pressure rise is possible for some condensing flow cases) – one obtains:

$$\begin{aligned}\Delta p_T &\equiv \int_0^L \left(-\frac{\partial p}{\partial x}\right)_{fric}.dx + \int_0^L \left(-\frac{\partial p}{\partial x}\right)_g.dx + \int_0^L \left(-\frac{\partial p}{\partial x}\right)_{acc}.dx \\ &\equiv (\Delta p)_{fric} + (\Delta p)_g + (\Delta p)_{acc}\end{aligned} \tag{52}$$

For each of the three pressure gradient terms, particularly the frictional pressure gradient, there are several modeling approaches (Ghiaasiaan 2007; Kim and

Mudawar 2014; Thome 2004). For the acceleration and gravity terms, the following definitions arise from adding 1-D form of vapor and liquid momentum balance equations (see derivation and definitions in Carey 1992):

$$\left(-\frac{\partial p}{\partial x}\right)_{acc} = G^2 \frac{d}{dx}\left[\frac{X(x)^2}{\rho_V.\epsilon} + \frac{(1-X(x))^2}{\rho_L{}^*(1-\epsilon)}\right] \tag{53}$$

$$\left(-\frac{\partial p}{\partial x}\right)_{g} = [\epsilon\rho_V + (1-\epsilon)\rho_L].g\sin\varphi \tag{54}$$

In obtaining Eqs. (53) and (54), mass-balance equations and definitions of void fraction ϵ, mass-flux G, and quality X are also used. In Eq. (54), "φ" measures the angle between the tube axis and the horizontal, and hence $\left(-\frac{\partial p}{\partial x}\right)_g \cong 0$ for horizontal tubes, as $\varphi = 0$.

For integrating Eq. (53), one may choose a void-fraction model – such as Zivi's in Eq. (49) or the one in Eq. (50). For the frictional pressure gradient in Eq. (52), one may choose any one of several adiabatic pressure gradient calculating models by replacing "X(x)= constant" situation for the adiabatic cases with genuine X(x) variations with x – as obtained by integrating the ODEs (Eqs. (23) and (24) of Sect. 2.3) under use of appropriate flow-boiling or flow-condensation Nu_x correlations. Samples of such Nu_x correlations are given in Eqs. (27), (28), (29), and (30) of Sect. 3.1.1 or in Eqs. (35), (36), (37), and (38) of Sect. 3.1.2.

Two well-known frictional pressure gradient models for Eq. (51) are as follows.

Lockhart-Martinelli Model

$$\left(-\frac{\partial p}{\partial x}\right)_{fric} = \left(-\frac{\partial p}{\partial x}\right)_L \emptyset_L^2 \tag{55}$$

where $\emptyset_L$ is one of the several two-phase multipliers which depends on a certain Martinelli factor $\widetilde{X}_{MF}$ through the following relationships:

$$\begin{aligned}
\left(-\tfrac{\partial p}{\partial x}\right)_L &\equiv \frac{2f_L G^2(1-X(x))^2}{\rho_L D_h} \\
\left(-\tfrac{\partial p}{\partial x}\right)_V &\equiv \frac{2f_V G^2 X(x)^2}{\rho_V D_h} \\
\emptyset_L^2 &= 1 + \frac{C}{\tilde{X}_{MF}} + \frac{1}{\tilde{X}_{MF}} \\
\tilde{X}_{MF}^2 &\equiv \frac{(\partial p/\partial x)_L}{(\partial p/\partial x)_V}
\end{aligned} \tag{56}$$

The following quantities, with subscript "k" – where "k = L" or "k = V," are needed for evaluating the terms in Eqs. (55) and (56). These quantities include $Re_L(x) \equiv G(1 - X(x))D_h/\mu_L$ and $Re_V(x) \equiv G \,.\, X(x)D_h/\mu_V$.

For phase "k" to be laminar, $Re_k < 2000$, and for it to be turbulent, $Re_k > 2000$. The constant C in Eq. (56) is given in Table 5.

The friction factors in Eq. $(56)_{1-2}$ are:

$$\begin{aligned} f_k &= 16Re_k^{-1} \cdots \text{for} \cdots Re_k < 2000, \\ f_k &= 0.079Re_k^{-0.25} \cdots \text{for} \cdots 2000 \le Re_k \le 20,000, \text{ and} \\ f_k &= 0.046Re_k^{-0.2} \cdots \text{for} \cdots Re_k \ge 20,000 \end{aligned}$$

Friedel Model

$$\left(-\frac{\partial p}{\partial x}\right)_{fric} = \left(-\frac{\partial p}{\partial x}\right)_L \emptyset^2_{Friedel} \tag{57}$$

where while retaining the remaining definitions in Eq. (56), $\emptyset^2_{Friedel}$ is defined (see Friedel 1979) as:

$$\emptyset^2_{Friedel} \equiv E + \frac{3.24\,FH}{Fr_H^{0.045} \cdot We_L^{0.035}} \tag{58}$$

The terms in Eq. (58) are:

$$\begin{aligned} E &= (1-X)^2 + X^2 . \frac{\rho_L}{\rho_V} . \frac{f_V}{f_L} \\ F &= (1-X)^{0.224} \bullet X^{0.78} \\ H &= \left(\frac{\rho_L}{\rho_V}\right)^{0.91} . \left(\frac{\mu_V}{\mu_L}\right)^{0.19} . \left(1 - \frac{\mu_V}{\mu_L}\right)^{0.7} \\ Fr_H &= \frac{G^2}{gD\rho_H^2} \\ \rho_H &= \left[\frac{X}{\rho_V} + \frac{1-X}{\rho_L}\right]^{-1} \\ We_L &= \frac{G^2 D_h}{\sigma . \rho_H} \end{aligned} \tag{59}$$

Table 5 Values of C for Lockhart-Martinelli model

Liquid	Gas	C
Turbulent	Turbulent	20
Laminar	Turbulent	12
Turbulent	Laminar	10
Laminar	Laminar	5

Table 6 Values of C for **(a)** adiabatic and condensing flows; **(b)** boiling flows

(a)		
Liquid	Gas	$C_{non\ -\ boiling}$
Turbulent	Turbulent	$0.39Re_{LO}^{0.03}Su_{VO}^{0.1}(\rho_L/\rho_V)^{0.35}$
Laminar	Turbulent	$0.0015Re_{LO}^{0.59}Su_{VO}^{0.19}(\rho_L/\rho_V)^{0.36}$
Turbulent	Laminar	$8.7 \times 10^{-4}Re_{LO}^{0.17}Su_{VO}^{0.5}(\rho_L/\rho_V)^{0.29}$
Laminar	Laminar	$3.5 \times 10^{-5}Re_{LO}^{0.44}Su_{VO}^{0.5}(\rho_L/\rho_V)^{0.48}$
(b)		
	$C_{boiling}$	
$Re_L \geq 2000$	$C_{non-boiling}\left[1 + 60We_{LO}^{0.32}\left(Bo\frac{P_H}{P_F}\right)^{0.78}\right]$	
$Re_L < 2000$	$C_{non-boiling}\left[1 + 530We_{LO}^{0.52}\left(Bo\frac{P_H}{P_F}\right)^{1.09}\right]$	

Kim and Mudawar (2014) report poor comparisons of experimental pressure-drop (considering a large set of data) for flow boiling and flow condensation with those obtained from the above-described procedures employing correlations by Lockhart and Martinelli (1949) and Friedel (1979).

Kim and Mudawar (2013d), after introducing $Re_{LO}(\equiv GD_h/\mu_L)$ and $Su_{VO}\left(\equiv \rho_V \sigma D_h/\mu_V^2\right)$, recommend continued use of Lockhart and Martinelli model in Eqs. (55) and (56) with replacements for the constant C (appearing in Eq. (25)) in Table 5 being given, for adiabatic and condensing flows, as in Table 6a below. For boiling flows, calculation of constant $C = C_{boiling}$ involves use of $C_{non\ -\ boiling}$ (calculated for adiabatic and condensing flows) in Table 6a through relationships given in Table 6b.

Grönnerud Model This popular pressure gradient model, available in Grönnerud (1972), is used here – but not reviewed for brevity.

3.5 Available CHF Considerations and Correlations

As discussed in the Introduction and a subsection (Flow and CHF-Related Instabilities) of Sect. 2.2, crossing certain threshold values of critical heat-flux while progressively increasing the values of a uniform heat-flux impositions on the flow-boilers (most conservative "method of heating" for identifying this phenomena) leads to vapor blanketing of certain downstream parts of the boiling surface. This is followed by sustained unsteady instabilities and subsequently – in some cases – runaway unsteady rise in the temperature of the vapor-blanketed boiling surface. There are several mechanisms for such flow-boiling instabilities – with only a qualitative relationship to the extensively studied CHF mechanisms for pool boiling.

The pool-boiling CHF, as discussed for the *boiling curves* in the "$q''_w - \Delta T$" plane (Collier and Thome 1994; Dhir 1998), relates to emission of bubbles with increasing and then plateauing bubble departure diameters, significantly increasing bubble departure frequency as well as nucleation site density with increasing heat-flux (see, e.g., McHale and Garimella 2010). At certain limiting values of these millimeter-scale departure diameters and plateauing bubble departure speeds, the bubbles ram into one another and coalesce – creating both vertical and lateral "connected vapor zones." Thus, the heated surface loses direct contact with liquid (except for a solid-like adsorbed liquid layer) and develops, instead, a poor but direct thermal contact with the vapor of much lower thermal conductivity. This pool-boiling CHF threshold has been studied from the point of views of instability (Kelvin-Helmholtz) of vapor columns of jets – issuing in the direction normal to the boiling surface – as CHF heat-flux level is approached from lower values of heat-flux (Dhir 1998; Dhir and Liaw 1989; Haramura and Katto 1983, etc.). This has also been studied from the point of view of instability (Rayleigh-Taylor) of vapor film blankets as post-CHF heat-flux values are reduced (Linehard and Dhir 1973; Zuber 1959). These and other related studies (Katto 1994) have been reviewed, and their relationship to ebullition cycle of nucleating bubbles below CHF and nucleation site density growth have been and are being explored/studied (Dhillon and Buongiorno 2017; Gerardi et al. 2009; McHale and Garimella 2010; Phan et al. 2009; Zeng et al. 1993a, b; Jones et al. 2009, etc.). Such investigations need to be better related to CHF. These pool boiling works relate to flow-boiling CHF only for the limited $G \cong 0$ zone in Fig. 5.

The flow-boiling CHF mechanisms at higher G values – as discussed through Figs. 1, 4, and 5 – and associated dry-out heat-flux and dry-out-related CHF values (Fig. 1b) are available in Kim and Mudawar (2013b). Other correlations such as Wojtan et al. (2006), Katto and Ohno (1984), Bowring (1972), and Zhang et al. (2006) can also be used with discrimination – as discussed in Basu et al. (2011). These are the CHF estimates (CHF1 in Fig. 1b) that are of interest to this chapter. This is because the onset of inverted annular flows related CHF (CHF2 of Fig. 4 and Fig. 5) are typically higher for the innovative designs of interest – which involve millimeter-scale ducts, controlled liquid film thickness annular boiling, and avoidance/minimization of liquid entrainment up to the exit.

If the heat-flux relative to mass flux is higher than a certain threshold (Fig. 5), at lower qualities – through departure from nucleate boiling (DNB) and associated inverted annular flows – CHF is achieved (Fig. 4), and its value can be estimated. The estimates can be based on CHF for subcooled flows at the inlet in the limit of the subcooling going to zero. Such CHF results are available in Collier and Thome (1994) and Qu and Mudawar (2004). In the subsection (Flow and CHF-Related Instabilities) of Sect. 2.2, it was argued that inverted annular flow CHF typically begins somewhere in the macro-nucleate boiling region I or plug-slug region II of Fig. 1b. However, there are exceptions. For example – at the connected inlet of multiple parallel channels – the instability may begin right at the inlet (Qu and Mudawar 2004), or for microscale ducts, it may begin at large local qualities

associated with the wispy annular regimes (see experimental photographs in Kuo and Peles 2009). Also, for microscale ducts – which are not of primary interest here – CHF values get affected by surface tension and surface texture (reentrant cavities, etc.) in a different way than the larger-scale ducts (see Kuo and Peles 2009). Also, for micro-scale duct flow boiling, CHF mechanisms get affected when vapor bubbles grow to the size of the micron-scale ducts (see Kumar and Kadam 2016).

Since the threshold defining critical curves in Fig. 5 have not yet been established with any degree of consensus, it is not uncommon for researchers to report that, at moderate mass flux, CHF could manifest itself through either of the two mechanisms discussed above (Shah 2015a).

As conjectured in Das et al. (2012), CHF arises from interactions between macroscale instability far (in the normal direction) from the heated surface and a more universal microscale phenomena near the heated surface. Near the heated surface, at CHF, replenishment of fluid into the micro-layer (see Raghupathi and Kandlikar 2016 and Sect. 6) present on the wetting surface – between the wet and dry sides – is not allowed from the wet side. With the macro-layer instability and micro-layer, phenomena working together, a dynamic CHF process is often triggered. Therefore, this CHF process has as many quantitative characterizations as there are varieties of macroscale flows (see multitudes of CHF characterizations in Katto 1994). The dynamic CHF process results in a situation where only an adsorbed layer of fluid in the vapor-blanketed domain is allowed while the time-averaged area associated with this vapor blanketing becomes larger and sustained.

In low mass-flux and low heat-flux cases, the dry-out instability as heat-flux values are increased for the annular flow in Fig. 1b is also indicated by a large surplus of mechanical energy that is supplied from the liquid film to the adjoining vapor flow, while the thin liquid film near dry-out zone consumes less and less viscous dissipation energy – see CFD studies of Ranga Prasad et al. (2017). This surplus of mechanical energy, typically, has to go to the vapor flow near the dry-out zone (see streamline patterns in Ranga Prasad et al. 2017). As higher heat-flux values are approached, this surplus energy can no longer be absorbed by either the steady flow of the vapor or the steady flow of the liquid (on the wetting surface) near the dry-out zone – and this is likely one of the contributing reasons that lead to dry-out instabilities. This is also a likely reason as to why dry-out instabilities can often be delayed (i.e., CHF values increased) by enhancing the liquid retaining wetting characteristics near the exit zone of the flow-boiler in Fig. 3a. These liquid retaining or liquid supplying techniques require sustaining the liquid flow in the liquid micro-layer in a way that it resists formation of nearby dry adsorbed layer through passive material alteration leading to super-hydrophilicity of the surface near the boiler exit or use of a porous and wetting exit zone boiling surface with additional and independent liquid supply into the pores or by active enhancement of wettability by use of suitable electric field impositions underneath a dielectric (near the exit) boiling surface, etc.

For design purposes of flow-boilers in Fig. 3a (as discussed in the next section), one can tentatively use a relevant and existing CHF threshold value estimates and/or simply ensure – by flow control (also see Sect. 6, as this is possible through proper

design of innovative annular flow-boilers) – that the exiting liquid layer is kept sufficiently thick (>10–20 μm or so).

4 Above-Reviewed Two-Phase Flow Correlations in the Context of their Use in the Design of Innovative Devices Experiencing Annular and Steady Flow Boiling and Flow Condensation

The correlation structure discussed in Sect. 2 supported the specific correlations reported in Sect. 3. The specific correlations in Sect. 3 were either developed with the help of data obtained from experiments (often flow-regime transition and pressure gradient correlations used adiabatic flow-regime maps) or computational/analytical solutions or by a combination of the two. The structure of correlations reported in Sect. 2 were developed with the aid of theory underlying nondimensionalization processes and some understanding of the physics that underlie these phase-change flows. Design of new experiments or new systems for a given working fluid and results obtained for a range of operating conditions can help develop such correlations. This, in turn, requires preliminary – but mutually consistent – "order of magnitude" estimates for values of variables (such as liquid and vapor flow rates, wall heat-flux or wall temperature values, inlet pressure, length and hydraulic diameter of the device, heat transfer coefficient values, pressure-drop values, liquid film thickness values, etc.) which will make device operations possible. To begin with, until better correlations or experimentally obtained refinements for the existing correlations become available, correlations that are presently available need to be judiciously used to define the experimental and/or design operating conditions and associated instrumentation requirements.

Need and use of existing correlations are motivated here with the help of two specific examples. The first example is that of a preliminary design of a millimeter-scale flow-boiler – operating in a steady annular/stratified regime with thin liquid film flows (Fig. 3a) – either in the presence of nucleation (at submicron-scale bubble diameters, as in regimes III and IV of Fig. 1b) or under suppressed nucleation conditions (as in regime V of Fig. 1b). The second example is that of a preliminary design of a millimeter-scale flow-condenser for a steady annular/stratified film-wise condensation on a hydrophilic surface (see Fig. 3b). In both examples, it is assumed here that the fluid flows through a horizontal duct of rectangular cross-section with high aspect ratio (adequately modeled as a channel) – with the heat-exchange surface being the bottom plate.

4.1 Design of Millimeter-Scale Annular Flow Boilers: An Example Illustrating Use of the Reviewed Correlations

The next subsection discusses some of the desired specifications and constraints for the design of an innovative flow-boiler operating in the annular flow-regime.

4.1.1 Desired Specifications, Constraints, and Information/Knowledge Needed for Meeting the Requirements

(i) A pure working fluid should be chosen such that it has a saturation temperature in 30–90 °C range for operating inlet pressures in 100–110 kPa range.

(ii) The inlet quality (at x = 0 in Fig. 3a) should be higher than the critical quality of transition from non-annular to annular flow-regimes – ensuring annular flow realization. For this, it is important to know, approximately, the quality at which the flow-regime transition occurs with estimates coming from different flow-regime transition maps. The required scientific structures for this have been discussed in Sect. 2, and the status of available knowledge has been discussed in Sect. 3. These estimates are sought to be within a reasonable range of values that would suffice, with trial-and-error experimental adjustments, for present purposes. It is hoped that, in the future, such estimates could be further improved (i.e., made more accurate) through a proper synthesis of experiments and modeling.

(iii) The *inlet* film thickness Δ_{in}, the liquid film thickness just downstream of the splitter plate in Fig. 3a, is desired to be around 300 μm. This is, presumably, neither too thin nor too thick, and it is important for subsequent and possible transitioning of the steady operations to pulsatile operations – the benefits of which have been alluded to through curves $I_{1-(ii)}$ and $I_{2-(ii)}$ in Fig. 1b and are further discussed in Sect. 6 (see experimental results given by Kivisalu et al. 2014). The control of inlet liquid film thickness by adjusting the recirculating vapor flow rate is essential because, otherwise, the liquid film thickness may change abruptly – as it exits the splitter plate in Fig. 3a – to an undesirable range of values. Thickness, at or below 300 μm, is needed to keep the films very stable – with or without micron/submicron diameters nucleating bubbles – even when large amplitude standing waves are superposed on the interface. For such a design, a correlation for inlet film thickness with dependence on inlet quality is required as input. Since this is a stratified/annular flow through a rectangular channel, with nearly adiabatic self-seeking free-surface locations immediately downstream of the inlet splitter plate (see Fig. 3a), a set of void-fraction correlations for adiabatic flows (as discussed in Sect. 3) could be used to obtain a good range of appropriate inlet quality and associated inlet film thickness values.

(iv) To avoid dry-out-related CHF instabilities at or near the exit, the exit quality should be less than 1 and the heat-flux at the exit should be less than the available order of magnitude estimates for CHF associated with dry-out instability ($q''_{w|exit} < q''_{CHF|dry-out}$). For this, an estimate of a dry-out-related CHF, obtained from correlation(s), such as the ones presented by Qu and Mudawar (2004), may be used. However, instead, the following more conservative constraint is utilized here. As a safety measure, it is required that the film thickness at the exit, estimated in different ways, be equal to or greater than 20 μm or, alternatively, one-fifth of the inlet film thickness (i.e., $\Delta_{out} \geq \Delta_{in}/5 \geq O(10\ \mu m)$). This constraint is also helpful in ensuring that inlet vapor

speeds (or qualities X_{in}) are not too large, as entrainment of liquid into the vapor needs to be avoided/minimized.

(v) Some of the important information that are required for this design are the Reynolds numbers: Reynolds numbers based on total mass-flux Re_T ($\equiv Gh/\mu_V$), liquid Reynolds number Re_L ($\equiv G(1 - X)h/\mu_L$), and vapor Reynolds number Re_V ($\equiv GXh/\mu_V$). The first Reynolds number is typically used in evaluating Nusselt number correlations for saturated flow boiling covering annular regimes (over appropriate range of qualities). Meanwhile, the second and third Reynolds numbers are often needed for assessing whether the liquid and vapor flows are laminar or turbulent and, accordingly, for selecting constants in sub-correlations (either directly for Nusselt number correlations or indirectly for related pressure-drop correlations). The knowledge of the laminar/turbulent nature of liquid and vapor flows are also useful in choosing appropriate correlation(s) that are available for different void-fraction models.

(vi) Since there are separate inlet channels for liquid and vapor, and a splitter plate is used (as in the experiments of Kivisalu et al. 2014) to ensure that the liquid and vapor do not mix before they enter the test section (as shown in the Fig. 3a), the cross-sectional area for vapor flow just before the inlet (locations $x < 0$) is different from the cross-sectional area for the vapor flow within the test section (locations $x \geq 0$). Furthermore, because of nonzero vapor inflow rate at the inlet and its subsequent acceleration associated with flow boiling, the vapor speed at the exit of the test section would be higher (much higher for higher heat-fluxes) than it is at the inlet of the test section. To avoid compressibility-related choking effects (see Ghiaasiaan 2007), it is required that the vapor speeds at both the inlet and the exit be, approximately, less than one-third of the speed of sound for saturated vapor operating at pressures that are at or below the inlet pressure value.

(vii) The inlet pressure p_{in} is required to be above atmospheric pressure such that, despite the pressure-drop along the length of the channel, the exit pressure is also higher than the atmospheric pressure (i.e., $p_{out} > p_{atm}$). This requirement is to make the design simpler, so that the system does not have to exhibit stringent and prolonged tolerance to vacuum pressures. For systems operating below atmospheric pressure, even small leaks of air can, over time, lead to substantial buildup of non-condensable air into the system, and then this system design, based on pure vapor and pure liquid flow-physics assumption and associated correlations, as proposed, will fail.

(viii) Further, despite the pressure-drop between the inlet and the exit of the channel, mechanical power in the vapor at the exit is likely to be much more than the incoming power at the inlet – i.e., for exiting vapor speeds relative to the inlet, it is expected that $P_{V,out}(\equiv p_{out} \cdot v_{V,out} \cdot A_{out}) > P_{V,in}(\equiv p_{in} \cdot v_{V,in} \cdot A_{in})$. The net power out ($P_{V,out} - P_{V,in}$) has to be maximized for high heat-flux cases. This is to ensure that no compressor is needed for steady operations and for start-up, shutdown, and other transients, only minimal additional power is needed for the recirculating vapor flow compressor shown in Fig. 3a. Note that the liquid pump and pulsator options (discussed in Sect. 6) already consume insignificant power.

(ix) For a known uniform heat-flux specifying the "method of heating," Eq. (24) yields linear quality variations, and, subsequently, order of magnitude estimate of the heat transfer coefficient h_x can be obtained from a Nusselt number correlation – which is only needed for assessing wall temperature $T_w(x)$ variations associated with the boiling surface. It is required that the design be such that the mean wall temperature $\overline{T}_w$ be not too high and remain below a certain threshold value specified by the application (e.g., $\overline{T}_w \leq 85\ ^\circ C$ for electronic cooling applications).

(x) The key parameters whose desired ranges need to be recommended, or chosen, to propose a design that satisfies the above conditions are mass-flux G, length of the channel L, height of the channel h, inlet pressure p_{in}, and inlet quality X_{in}.

4.1.2 Implementation of a Sample Design Methodology: Meeting the Requirements Given in "Section 4.1.1" and Obtaining Results for Steady Annular Flow-Boiler Operations

A range of inlet pressures p_{in}, total mass fluxes G, and mean heat-flux $\overline{q}''_w$ (or mean wall temperatures $\overline{T}_w$, depending on what is known or preferred assumption about the "method of heating") are initially chosen and considered. They are then optimized to satisfy most of the constraints mentioned in the above-described design requirements. Note that the length L of the flow-boiler may also be adjusted to satisfy remaining constraints. This is a reasonable approach because of the flexibility to stack these flow-boilers in series and/or in parallel arrangements toward a feasible solution for a new high heat-flux system design that can remove heat from a designated cooling area of interest.

Toward achieving a high heat-flux design, to begin with, one particular combination of inlet pressure, total mass-flux, a selected channel height h, and mean heat-flux (or mean wall temperature), is defined as a specific initial choice of operating condition for a single flow-boiler element (Fig. 3a) of the required system design. For example, if one is interested in achieving a steady heat removal capability at 1 kW/cm^2 from each of the flow-boilers in a new system design, one can investigate and attain an acceptable steady annular operation (say, at a lower imposed heat-flux value of about 20 W/cm^2) and a design restriction of $T_w(x) < 85\ ^\circ C$ over the length of the boiler. This can be achieved for suitable initial operating conditions specified for steady operations in Fig. 3a. Next by superposing pulsatile or other innovative operations, on the initial steady annular operating conditions indicated by points A and B and curves $I_{1-(ii)}$ and $I_{2-(ii)}$ in Fig. 1b, c, and controlling the range of external impositions (e.g., pulsation amplitudes at a given frequency, see Sect. 6), different phenomena (e.g., different levels of large amplitude standing waves on the interface) can be realized to obtain a range of very high local heat transfer coefficient h_x for the innovative operations. It can be shown that the initial steady design's $\overline{q}''_w$ ($\approx$ 20 W/cm^2) handling capability can be further increased in two steps by shifting to pulsatile (or similarly new) operations and increasing the local heat transfer coefficient h_x by a factor of about 10–30 (over the initial steady realization), provided a good strategy is

followed. In the first step, pulsatile (or equivalent) operations' increasing values of imposed controlling variable (e.g., amplitude at a certain frequency, see Sect. 6) can lead to a $\overline{q}_w^{''}$ (≈200 W/cm^2) and $T_w(x) < 85$ °C operations by only slightly adjusting the initial mass flux for the chosen length L. In the second step, pulsatile (or equivalent) operations' imposed controlling variable's values are further increased (e.g., amplitudes at the same frequency for pulsation impositions) with concurrent increases in $\overline{q}_w^{''}$ (to 1 kW/cm^2) and inlet mass-flux G while retaining the inlet quality from the second step. The second step also requires simultaneous suitable vapor bleeding flow rates from a set number of locations on the top dry plate in Fig. 3a. This is for satisfying incompressible vapor (Mach number < 0.28) and wall temperature $T_w(x) < 85$ °C restrictions.

However, the purpose of this review is not to propose a high heat-flux system design. Its focus is limited to elucidating the importance of a steady design methodology for the initial annular steady flow realization – as an enabling component of a high heat-flux system design.

For this illustration, toward meeting the design requirements elucidated in Sect. 4.1.1, an example case is chosen for which the channel height is 5 mm, the working fluid is R-123, and wall temperature restriction is $T_w(x) < 150$ °C. Additional tentative choices are inlet pressure $p_{in} = 120.1$ kPa, total mass-flux G = 300 kg/m^2 s, and mean heat-flux $\overline{q}_w^{''} = 50$ W/cm^2 = 500 kW/m^2. The flow-boiler length L is to be chosen in a way that the requirements given in Sect. 4.1.1 are met by following the steps given below:

(i) For any chosen operating conditions, the first step is to find the critical quality for transition from non-annular to annular flow-regimes ($X_{cr|NA-A}$) through available maps for traditional Fig. 1a operations, so an inlet quality $X_{in} > X_{cr|NA-A}$ can be chosen for Fig. 3a operations. This is accomplished by using approximate flow-regime transition maps. A few appropriate flow-regime transitions maps should be chosen, based on hydraulic diameter D_h, fluid, orientation (horizontal, in this case) of the channel/tube, etc. Since the flow-regime transition maps are semi-empirical in nature (i.e., correlated using data from either existing experiments or modeling/simulations), as a conservative measure, it is recommended that the critical quality for transition from non-annular to annular flow-regime $X_{cr|NA-A}$ be obtained from at least three different flow-regime transition maps and the highest of those qualities be used. For the flow-boiler design under consideration, flow-regime transition maps proposed by Harirchian and Garimella (2012), Kim and Mudawar (2013a), and Mandhane et al. (1974) were considered here to be approximate and relevant ones for further evaluations. Even though the map by Mandhane et al. (1974) was developed for adiabatic flows, its use in the present scenario is justified because the flow will be approximately adiabatic immediately after it exits the splitter plate at the inlet (Fig. 3a). The transition qualities obtained using the correlations are tabulated in Table 7. It can be noticed that the critical transition qualities obtained from correlations proposed by Kim and Mudawar (2013a) and Harirchian and Garimella (2012) are quite low and less likely to be applicable to the present design estimates. It was

Table 7 Critical transition qualities from non-annular to annular flow-regime obtained using correlations for the channel height (h = 5 mm; fluid, R-123; and operating conditions, p_{in} = 120 kPa; G = 300 kg/m^2 s; $-q''_w$ = 50 W/cm^2)

Flow-regime transition correlations	Transition quality, $X_{cr\|NA-A}$
Harirchian and Garimella (2012)	0.028
Kim and Mudawar (2013a)	0.0283
Mandhane et al. (1974)	0.307

further noticed that, for low values of mass-flux (G < 30 kg/m^2 s), Kim and Mudawar (2013a) correlation provided higher values of critical transition quality, while the critical transition qualities obtained from correlation by Harirchian and Garimella (2012) and flow-regime map by Mandhane et al. (1974) were quite low (<0.1). For the initial conservative estimate, it is then decided to set $X_{in} > 0.3$ (as implied by flow-regime map of Mandhane et al. 1974). It should be noted that, typically, there is also an experimentally determined upper bound on X_{in} so one can avoid entrainment and wispy annular flows.

(ii) For approximately realizing the assumed inlet film thickness Δ_{in} of around 300 μm, first the vapor Reynolds number Re_V ($\equiv GXh/\mu_2$) is calculated with $X_{cr|NA-A}$ as the initial guess of inlet quality X_{in}. This is to check if the vapor flow is laminar or turbulent. If the vapor flow is turbulent (and it is ensured that the liquid flows are still laminar), the adiabatic void-fraction correlations proposed by Zivi (1964) and Rouhani and Axelsson (1970) (with modifications for horizontal flows proposed by Steiner 1993) are used to calculate film thickness (note that $\epsilon_{in|correlation} = (h - \Delta_{in})/h$). If the vapor flow is also laminar, void-fraction correlation proposed by the authors (Ranga Prasad et al. 2017) may be used along with the ones mentioned earlier. Although all the abovementioned void-fraction correlations were originally proposed for adiabatic flows, their use in this case is, once again, justified since the flow is approximately adiabatic immediately after the splitter plate at the inlet (Fig. 3a). Using $X_{cr|NA-A}$ as the first guess, the corresponding film thickness values are calculated using the abovementioned void-fraction correlations. Next, the inlet quality value is typically increased to values higher than $X_{cr|NA-A}$ until the mean film thickness calculated from the chosen correlations gives a value of around 300 μm or less. However, since these are semi-empirical correlations with large uncertainties, the mean of the different film thicknesses obtained from the three different correlations above is actually considered the final film thickness value from this void-fraction approach. The final inlet film thickness value, for this example, is estimated to be 299.9 μm, and the corresponding inlet quality is found to be 0.405 ($>X_{cr|NA-A}$).

(iii) For this inlet quality, using the space available for the vapor flow above the splitter plate (3.7 mm for the current case), the vapor velocity and its ratio relative to the speed of sound are calculated. For the current case, it is found to be 0.17. If the ratio of inlet vapor speed to the speed of sound is more than 0.28 (conservatively chosen to be less than 0.33), it is suggested that, initially, the mass-flux G be reduced (which essentially means changing the initially

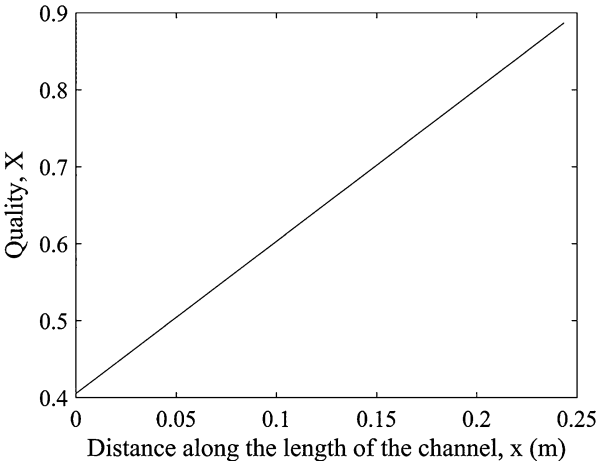

Fig. 8 Variation of quality X along the length of the channel

guessed operating condition) and steps (i) to (ii) be repeated. If that is not feasible, the height of the channel may also be increased so that the ratio of the vapor speed to sound speed is reduced.

(iv) If the compressibility effect constraint (i.e., Mach number <0.28) is satisfied at the inlet, assuming an arbitrarily high exit quality (say, 0.98) for a sufficiently long boiler and then using Nusselt number correlation(s), the heat transfer coefficient values for a linear range of qualities (as in Fig. 8, which is implied by Eq. (24) and uniform heat-flux assumptions) are calculated, along with their nucleate boiling (h_{nb}) and convective boiling (h_{cb}) components. For the current design problem, the correlation proposed by Kim and Mudawar (2013c), as discussed in Sect. 3, is used. The total heat transfer coefficient h_x for the full range of quality is calculated. The film thickness values for these qualities can be estimated by neglecting micro-nucleation effects on mean film thickness (these effects are, presumably, included in $h_{x|cb}(x)$ of Kim and Mudawar 2013c correlations) and ignoring *macro-nucleation* effects (modeled by $h_{x|nb}$ in Kim and Mudawar 2013c) by using the formula:

$$\Delta(x) \cong \frac{k_L}{h_{x|cb}(x)} \tag{60}$$

provided $h_{x|cb}$ values in Eq. (29) can be trusted (see Ranga Prasad et al. 2017 for better estimation of $h_{x|cb}$). However, it should be noted that this correlation (in fact most correlations) is semi-empirical in nature and obtained from curve-fitting available data for the total h_x values. So, while the total heat transfer coefficient h_x value might be approximately correct to within a certain percentage, the nucleate boiling and convective boiling term decomposition making up the total is arbitrary and (as discussed in Ranga Prasad et al. 2017) in all likelihood not correct. See Fig. 9a where such an initial decomposition from Kim and Mudawar (2013c) is denoted as $h_{x|cb-1}$ and $h_{x|nb-1}$

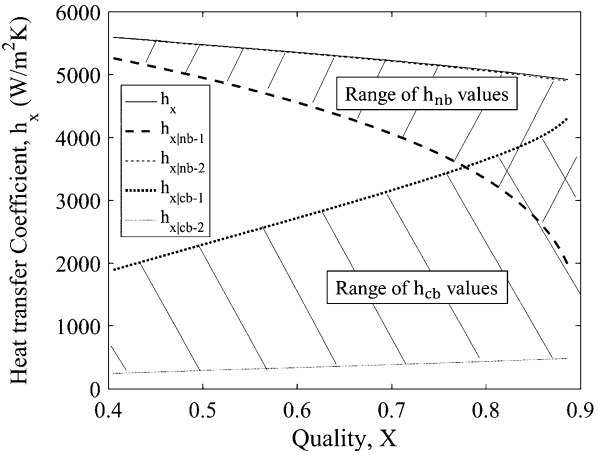

Fig. 9 Variation of heat transfer coefficients with quality – calculated using correlation proposed by Kim and Mudawar (2013c) along with the decomposition of h_x. The decomposition of h_x using the correlation are given as $h_{x|nb} \equiv h_{x|nb-1}$ and $h_{x|cb} \equiv h_{x|cb-1}$. The component terms of h_x after the introduction of correction factor α_c are $h_{x|nb-2}$ and $h_{x|cb-2}$. The actual values of the $h_{x|nb}$ are expected to lie between $h_{x|nb-1}$ and $h_{x|nb-2}$, while $h_{x|cb}$ actual values of $h_{x|cb}$ are expected to lie between $h_{x|cb-1}$ and $h_{x|cb-2}$

(whose order of magnitudes are probably more meaningful for regions I–III in Fig. 1a but likely incorrect for regions IV–VI). Therefore, a correction factor is introduced to obtain an improved $h_{x|cb-2} = \alpha_c \cdot h_{x|cb-1}$. The correction factor α_c is defined as the ratio of inlet film thickness calculated using void-fraction models (as in step (ii)) and the inlet film thickness calculated using convective boiling heat transfer coefficient term $h_{x|cb}$ (as in Eq. (60), i.e., $\alpha_c \equiv \Delta_{in-h|x-cb}/\Delta_{in-void-fraction-method}$). This is done because it is assumed that the void-fraction models provide more reliable estimate of film thickness value at the inlet because of the presence of adiabatic type conditions. For the present case, the correction factor α_c was found to be 0.132. It is then assumed that this can be used to better evaluate the convective component of heat transfer coefficient at the inlet (through $h_{x|cb,in-2} \cong k_L/\Delta_{in-void-fraction-method}$) because this is a more reliable order of magnitude estimate. Therefore, the convective boiling term $h_{x|cb-1}$ in Kim and Mudawar (2013c) is only approximate, and it can vary within a range bounded by this and the second estimate of $h_{x|cb-2} = \alpha_c \cdot h_{x|cb-1}$ – as obtained by correcting the Kim and Mudawar (2013c) values by simply multiplying it by a correction factor α_c. The nucleate boiling contribution term is calculated using the total heat transfer coefficient, which is experimentally known to be of reasonable accuracy, through relations such as $h_{x|nb-2} = h_x - h_{x|cb-2}$ or $h_{x|nb-2} = \sqrt{h_x^2 - h_{x|cb-2}^2}$ depending on whether $n = 1$ or $n = 2$ was originally used in Eq. (44) to decompose h_x between $h_{x|nb}$ and $h_{x|cb}$.

(v) Using the new corrected convective boiling $h_{x|cb-2}$ term in Eq. (60) given in step (iv), the new corresponding film thickness values, denoted as $\Delta_2(x)$, are calculated as a function of quality X over the range of quality values in step (iv). Further, using the vapor height above the exit film thickness ($\Delta_{exit} = \Delta_2(L)$), the vapor speed and its ratio with respect to the speed of sound are calculated for the exit location x = L. Now with the knowledge of film thickness available as a function of quality and quality variations available along the length of the channel, this step is iterated until an exit quality and a corresponding length L are found such that the Mach number at the exit is equal to or less than 0.28 *and* the exit film thickness is greater than or equal to 20–60 μm or one-fifth of inlet film thickness ($\Delta_{in}/5$). The restriction $\Delta_{in}/5$ was chosen for this example. The corresponding exit quality is considered as maximum exit quality, and the corresponding channel length is considered the maximum possible length L_{max}. The exit quality and maximum length thus calculated for the present design problem are 0.89 and 0.24 m, respectively. The variation of quality along this length of the channel is plotted in Fig. 8. The heat transfer coefficient values, for the range of qualities between the inlet and the exit, along with the two estimates of their component terms ($h_{x|nb}$ and $h_{x|cb}$), are plotted in Fig. 9. The film thickness values along the length of the channel (for the same quality range), calculated using convective boiling heat transfer coefficient $h_{x|cb-2}$ term and as obtained by the void-fraction correlation, are plotted in Fig. 10. Using total heat transfer coefficient values, wall temperature values are calculated using Eq. (4) and are plotted in Fig. 11.

A few important points to note are as follows:

(a) It is first assumed that the pressure-drop may be significant to affect sound speed, and therefore the sound speed at the exit is first calculated using the inlet pressure.

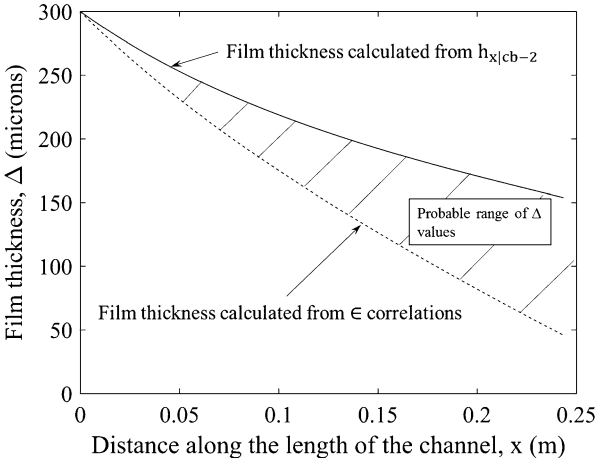

Fig. 10 Variation of liquid film thickness Δ along the length of the channel – calculated from void-fraction correlations and corrected convective boiling term of heat transfer coefficient $h_{x|cb-2}$ using Eq. (60)

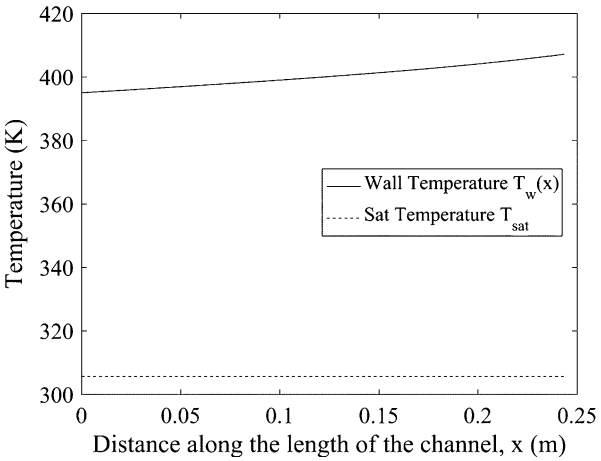

Fig. 11 Variation of wall temperature $T_w(x)$ along the length of the channel – calculated from total heat transfer coefficient using Eq. (4)

(b) The length calculated here is the maximum permissible length that would satisfy the constraints. However, as a conservative measure, it is suggested that the length of the channel could be a fraction (say, 0.7) of the maximum length L_{max} calculated earlier and that fraction should be further reduced if a different range of mean heat-flux ($\overline{q}''_w$) values are required for steady non-pulsatile operations.

(vi) For the calculated/identified quality variations between the inlet and the exit, both acceleration and frictional pressure-drops are calculated along the length of the channel. Acceleration pressure-drop is calculated using Eq. (53) and is dependent on the choice of void-fraction correlation (Zivi 1964 in this case) and does not depend on Nu_x correlation, as this case involves uniform heat-flux – and hence linear X(x) variations. The frictional pressure-drop is calculated using three different correlations, viz., Friedel (1979), Grönnerud (1972), and Lockhart and Martinelli (1949). This is done to get a range of possible frictional pressure gradient values which, as seen in Fig. 12a, have wide variations despite the fact that they are based on the easier correlations of experimental data obtained from adiabatic two-phase flows. The reasons are (i) simplifications in the implicit nondimensional parameter space used by these correlations (they do not explicitly use the nondimensional approach of Sect. 2, which is a more desirable approach if additional physics or modeling is not well established), (ii) the range of nondimensional parameters considered are not specified, and (iii) the data used in different correlations likely emphasize data in different zones of the underlying nondimensional parameter space. For present purposes, it is assumed that using flow-boiling-based X(x) values in these frictional pressure gradient correlations for adiabatic flows will suffice for order of magnitude estimates in Fig. 12a. However, for further calculations, as a conservative measure, the highest of the frictional pressure-drop values is chosen. The total and their corresponding frictional pressure-drop values

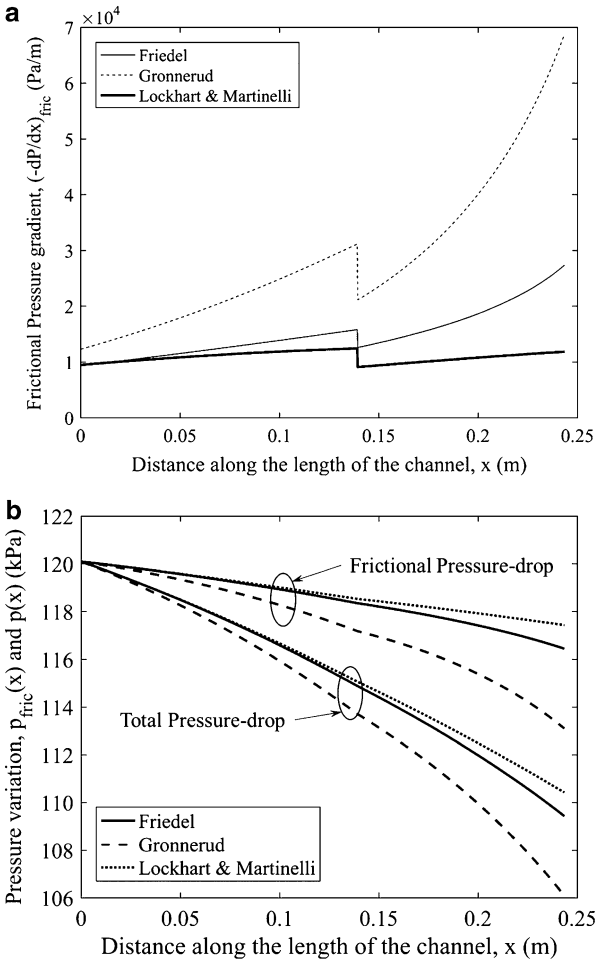

Fig. 12 **(a)** Variation of frictional pressure gradient along the length of the channel – calculated from Grönnerud, Friedel, and Lockhart and Martinelli pressure-drop correlations. **(b)** Both frictional pressure $p_{fric}(x) = p_{in} + \Delta p_{fric}$ and total pressure $p(x) = p_{in} + \Delta p_T$ variations with distance x are plotted. The frictional and total pressure-drops are defined in Eq. (52). The three curves from the three models are closer together than in part (**a**). This is because of dominance of acceleration pressure-drop in Eq. (52).

(relative to the inlet pressure) along the length of channel are shown in Fig. 12b, and the final exit pressure (including momentum/acceleration pressure-drop) is, for this example, 107.93 kPa.

(vii) Using the chosen inlet pressure and the exit pressure, along with vapor velocities (calculated in steps (iii) and (v) for the inlet and the exit, respectively), and the corresponding cross-sectional areas, net output power per unit channel width for the test section (as discussed in constraint (vi) of Sect. 4.1.1) is calculated and is found to be 8.97 kW/m. The vapor compressor power per unit width of the section is conservatively estimated as $1.2 \times [p_{in} - p_{out}] \cdot v_{in} \cdot h \cong 1.82$ kW/m. Since the net mechanical power input from the compressor is less than the mechanical power output, the flow-boiler design

operation is considered energy efficient – and for most steady operations in Fig. 3a, the recirculating vapor can use the route that bypasses the compressor.

4.2 Design of Millimeter-Scale Annular Flow Condensers: An Example Illustrating Use of the Reviewed Correlations

Design of the steady annular innovative operation of condenser shown in Fig. 3b is discussed in this section. Because of factors such as absence of nucleation and CHF phenomena, inlet quality of vapor flows being $X \cong 1$ and reducing at downstream locations, etc.; the number of constraints in the design of steady annular flow-condenser operations is relatively less as compared to that of steady annular flow-boiler operations.

4.2.1 Desired Specifications, Constraints, and Information/Knowledge Needed for Meeting the Requirements

This section discusses some of the constraints involved in the design of flow-condensers that may be required to operate in the thin liquid steady annular flow-regime. Such condensers can, in principle, be converted to high heat-flux compact devices by superposing a pulsatile flow physics and this is described in Sect. 6:

(i) It is important to know the transition quality from annular to non-annular flow-regimes so that the exit quality can be adjusted and kept above the transition quality. This is done with the help of the passively recirculating vapor arrangement in Fig. 3b. Using this strategy, non-annular flow-regimes (associated with high pressure-drop and poorer heat transfer rates) can be avoided all the way up to the exit of the condenser in Fig. 3b. For this, some appropriate flow-regime maps, as discussed earlier in Sect. 3.2.2, are used.

(ii) The total inlet Reynolds number ($Re_{in} = Re_T \equiv Gh/\mu_V$) needs to be computed for the chosen mass-flux G. This number is directly or indirectly required to evaluate any of the suitable Nusselt number correlations for flow-condensers and obtain quality X's variations along the length of the channel for, say, a known wall temperature case as specification for the "method of cooling." Further, for the known temperature specifying the "method of cooling," appropriate local Nusselt number correlation(s) would be required and should be used to get an order of magnitude estimate of the local heat transfer coefficient h_x, local heat-flux $q_w''(x)$, and the quality X(x) variations along the length of the channel (obtained from using Eq. (23) in Sect. 2).

(iii) Unlike the earlier case of flow boiling, the mechanical power in the vapor flow at the exit is, typically, lower than the mechanical power available in the vapor flow at the inlet. This is because of reduction in velocity along the length of the channel. However, the design should be optimized such that the reduction in velocity is minimal, and, consequently the loss in mechanical power in vapor is

also reduced – which is a relatively easy task for these millimeter-scale steady annular operations.

(iv) The length L of the condenser should be chosen such that exit liquid film thickness $\Delta(L)$ is less than say, 200 μm.

(v) Some of the parameters that are to be initially chosen and then varied to optimize the design are as follows: mass flux G, height of the channel h, length of the channel L, inlet pressure p_{in}, wall temperature $T_w = \overline{T}_w$, etc.

4.2.2 Implementation of a Sample Design Methodology: Meeting the Requirements Given in "Section 4.2.1" and Obtaining Results for Annular Flow-Condenser Operations

For a chosen working fluid, a range of inlet pressures p_{in}, mass fluxes G, and mean wall temperatures $\overline{T}_w$ are to be initially considered. These can later be optimized, based on constraints mentioned above or based on other specific and additional design requirements. However, similar to the flow-boiling design methodology, a particular combination of inlet pressure, total mass flux, and mean wall temperature is initially chosen as a specific operating condition around which all variations are to be considered. For the present case, the following parameters are chosen: fluid is R-123, channel height is $h = 5$ mm, inlet pressure is $p_{in} = 120.1$ kPa, total mass flux is $G = 300$ kg/m^{2}s, and the mean wall temperature is $\overline{T}_w = 382$ K, which corresponds to a cooling temperature difference of $\Delta T = 60$ K.

(i) For the chosen operating condition, the critical quality of transition from annular to non-annular flow-regimes ($X_{cr|NA-A}$) is calculated from available flow-regime maps, some of which have been discussed in Sect. 3.2.2. Here again flow-regime transition maps should be appropriately chosen with the working fluid, the orientation (horizontal, vertical, or inclined) of the channel, and mm/μm hydraulic diameter scale of the channel considered for selecting relevant maps in the literature. For the present case, flow-regime transition criterion proposed by Kim and Mudawar (2013a) and flow-regime map proposed by Mandhane et al. (1974) have been used. The critical transition qualities obtained from these flow-regime criteria are 0.048 and 0.307, respectively. Again, as in the design of innovative flow-boilers (in Sect. 4.1.2), the value obtained from the criterion proposed by Kim and Mudawar (2013a) is unacceptably low for this high mass-flux case even though the same correlation was found to have yielded reasonable estimates for the lower mass fluxes ($G < 50$ kg/m^2 s). The highest of the qualities obtained from these two criteria is tentatively considered as the critical quality of transition from annular to non-annular flow-regime. Furthermore, as a conservative measure, since the exit quality should be more than the critical transition quality, an even higher value (say, by $\Delta X = 0.05$ to 0.1) than the estimated critical value of transition quality is chosen to be the exit quality (say, $X_{out} \cong X_{cr|NA-A} + 0.1$). The chosen exit quality for the present case, at this step, is 0.407.

(ii) Assuming an inlet of 1 (or slightly less, say, 0.99) and using the knowledge of the exit quality calculated/identified from step (i) above, the local heat transfer

coefficient values for qualities between the inlet and exit qualities can be obtained by using Nusselt number correlation(s) of Kim and Mudawar (2013a) – which is of the type $Nu_x(X)$ and given in Eqs. (35), (36), (37), and (38). This correlation, for this case, can be directly evaluated and plotted (see Fig. 13) with values of X varying between the inlet and the exit qualities. The kink in Fig. 13, which in reality will be a gradual smoothed curve, is due to reduction in vapor quality from its inlet value of 1 – and is associated with thin liquid film flow transitioning from laminar to turbulent. The associated drop in h_x at the "kink," as the condensate moves from the higher-quality inlet values to the lower-quality downstream values, is unrealistic and is likely due to very approximate nature of Eqs. (35), (36), (37), and (38); part of the reason being that the correlation combines data from very different flow-physics realms of gravity-driven and shear-driven flow condensation. Such order of magnitude Nusselt number correlations, along with inlet and exit qualities, can also be used to calculate the length of the channel L, by obtaining quality versus distance X(x) variations by integrating Eq. (23) subject to the inlet value of $X(0) = X_{in}$. For the chosen exit quality $X(L) = X_{out}$, L is found to be 0.57 m. However, it should be noted that this would be the maximum possible length of the channel, and considerations should be given to the fact that it is to operate in the annular flow-regime, preferably with negligible entrainment. In addition, the test section might have to operate for multiple operating conditions, and all of the conditions should be taken into consideration before finally deciding on the length of the channel. For the chosen operating condition, however, the variation of quality along the length of the channel, as obtained from integrating Eq. (23), is shown in Fig. 14. The heat transfer coefficient values calculated above (see Fig. 13) can also be used to calculate the local wall heat-flux ($q''_w(x)$) values, by using Eq. (4). This is done and the results are plotted in Fig. 15. Again, drop in

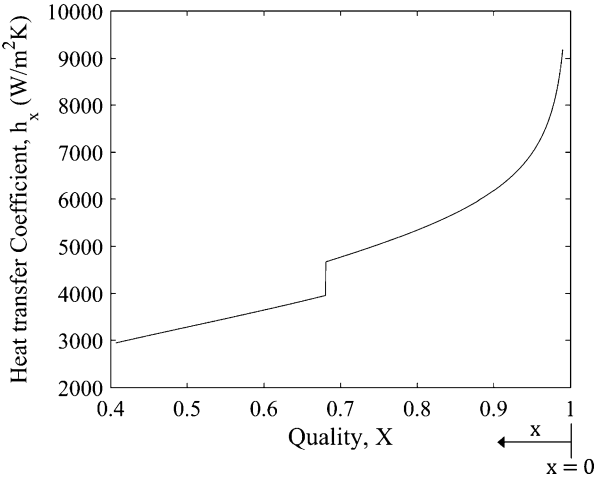

Fig. 13 Variation of heat transfer coefficients with quality – calculated using correlation proposed by Kim and Mudawar (2013a). Discontinuous reduction in h_x at downstream locations X (x) < 0.68 is due to thin laminar liquid becoming turbulent. The jump should have been an increase in h_x, and the above is likely due to inaccuracies in the h_x correlation for condensing flows

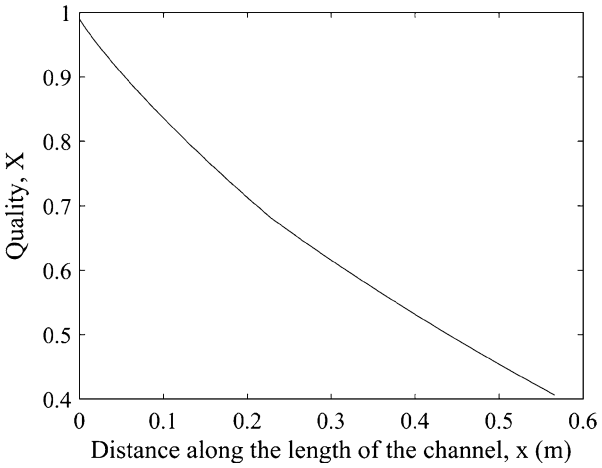

Fig. 14 Variation of quality X along the length of the channel calculated using Eq. (23)

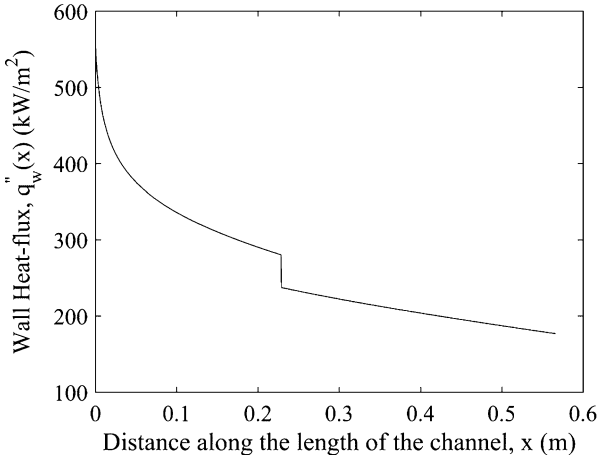

Fig. 15 Variation of wall heat-flux $q_w^{''}(x)$ along the length of the channel – calculated from total heat transfer coefficient using Eq. (4)

heat-flux at the "kink" in Fig. 15 is unrealistic and is due to reasons discussed for the "kink" in Fig. 13.

(iii) Using the inlet and the exit qualities, the pressure-drop/rise can be calculated using appropriate correlation(s). For this design, to get an estimate of changes in pressure along the length of the channel, frictional pressure-drop correlations proposed by Friedel (1979), Grönnerud (1972), and Lockhart and Martinelli (1949) were chosen and used. The acceleration pressure variation is calculated using Eq. (53). The reasons for the variations in frictional pressure gradient estimates of different models, as shown in Fig. 16a, are the same as those discussed for Fig. 12a. The frictional and total pressure variations along the

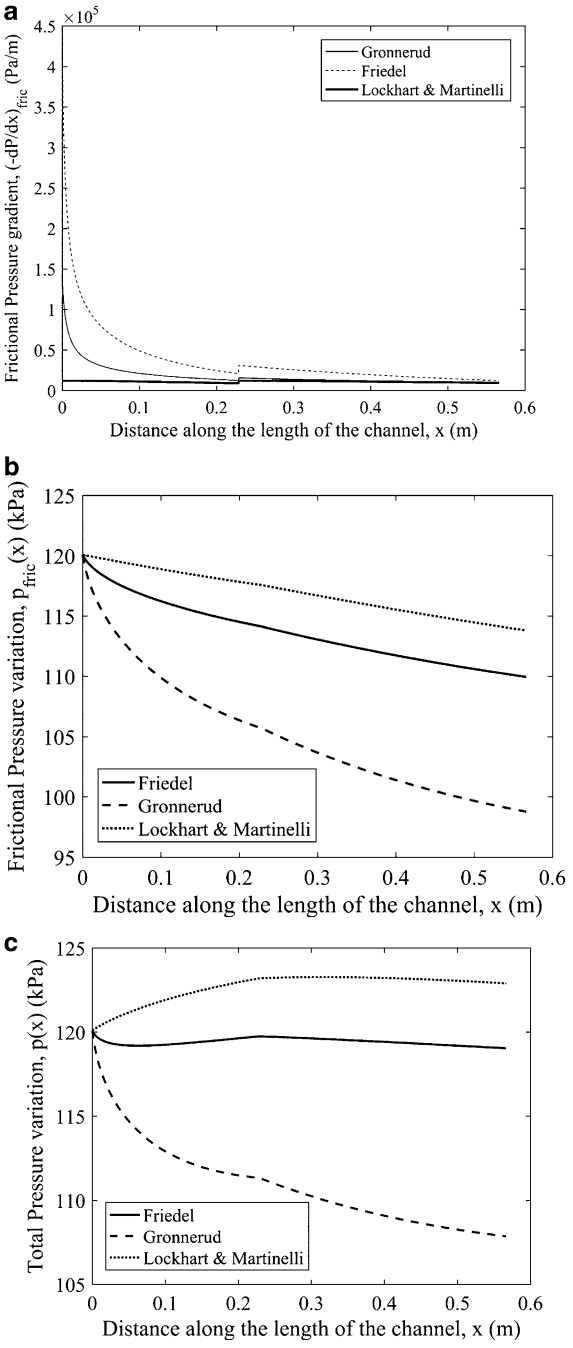

Fig. 16 **(a)** Variation of frictional pressure gradient along the length of the channel – calculated from Grönnerud, Friedel, and Lockhart and Martinelli frictional pressure-drop correlations. **(b)** Frictional pressure $p_{fric}(x) = p_{in} + \Delta p_{fric}$, with Δp_{fric} defined in Eq. (52), variations with distance x is plotted. **(c)** The total pressure variations $p(x) = p_{in} + \Delta p_T$, with Δp_T defined in Eq. (52); variations with distance x is plotted. The total pressure value p(x) rises with distance x for one of the three models. The total pressure variation values from the three models are higher than that of frictional pressure variation. This is because of decelerational pressure contributions from Eq. (53)

length of the channel, calculated using the three chosen correlations for frictional pressure, are respectively plotted in Fig. 16b and Fig. 16c. The final exit pressure, for L = 0.57 m, is found, by choosing the lowest absolute pressure (Grönnerud correlation), of the three total (frictional + acceleration) pressure values, shown in Fig. 16c, and is approximately 107.9 kPa. However, it can be seen in Fig. 16c that at least one of the other two frictional pressure-drop models (Lockhart-Martinelli) predicts pressure rise. Such rise in pressures (given p_{in} = 120.1 kPa) is possible in condensing flow operations due to vapor deceleration effects. However, as mentioned in Sect. 4.2.1, the design calculations should be done for different operating conditions, and pressure-drop (or rise) may be optimized, if needed, to minimize the reduction in mechanical power in the vapor (along with any other specific design constraint (s) that may also need to be imposed).

5 Improved CFD-Enabled Correlations (Current Status and Future Trends) Toward Developing Better Design Tools and Improved Understanding of Flow Physics

As discussed for the sample design methodologies presented in Sect. 4, the approximate order of magnitude prediction capability of available correlations and their strong empirical nature – for both annular flow boiling (because of the significance of microscale nucleate boiling contribution to the annular boiling heat transfer coefficient, in regions IV and V of Fig. 1b) and flow condensation – need to be improved for better understanding of flow physics as well as improved accuracy of the correlations. The basic approach for such improvements is illustrated through the concept diagram in Fig. 17.

Current status of correlations for annular flow boiling and flow condensation, as reviewed in Sects. 2 and 4, is predominantly empirical (with limited exceptions) and is characterized by the methodologies indicated in the experiments box (blue-bordered) of Fig. 17. The sought-for improvements require development of first principles (feasible for laminar/laminar annular flows) or minimal *ad hoc* modeling assumptions based (particularly for turbulent vapor and laminar liquid annular flows for the devices in Fig. 3) on computational simulations and accurate processing of such simulation results in the form of correlations – as indicated by the methodologies in the simulations box (red-bordered) of Fig. 17 – and their subsequent improvements with the help of proper synthesis with experiments. Therefore, such computational simulations need to be done in an environment where there is an active bidirectional information sharing with appropriately planned experiments for obtaining relevant data – towards enabling good synthesis of data from both the methodologies/activities (i.e., the experiments and the simulations boxes in Fig. 17).

In the following subsection, current status of simulation activities and their much needed evolutions, expected in the near future, are discussed separately for annular flow boiling and annular flow condensation.

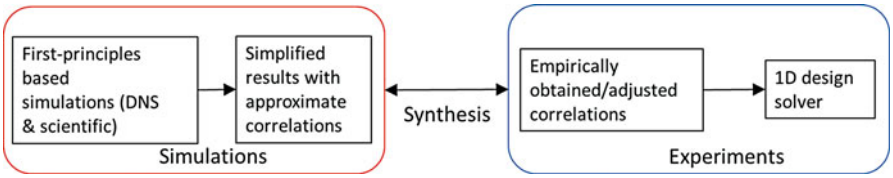

Fig. 17 Currently popular correlations employ, predominantly, the methodologies indicated in the experiments (*blue-bordered*) box. Modeling tool improvements require a bidirectional synthesis with the methodologies in the simulations (*red-bordered*) box

5.1 Annular Flow Boiling

As seen in estimates of heat transfer coefficient h_x in Sect. 4 (see empirical estimates for high heat and mass-flux cases, as shown in Fig. 9), experimental data underlying such correlation-based h_x estimates (and its convective and macro-/micro-nucleate boiling components) – supplemented by reasonable assumptions with regard to innovative annular flow-boiling approach in Fig. 3a – indicate a significant but reducing component of macroscale nucleate boiling over convective boiling (though $h_{x|nb} \geq h_{x|cb}$) over regions I–III of Fig. 1b, although the accuracy of estimates of $h_{x|cb}$ and $h_{x|nb}$ is more arbitrarily approximate than h_x in Eq. (31). However, as discussed in Sect. 4, the decomposition approach of h_x into macroscale nucleation component $h_{x|nb}$ and the convective component $h_{x|cb}$, either through Eq. (33) in Sect. 3 with $n = 2$ or other similar ones (e.g., Steiner and Taborek 1992, with $n = 3$) which use other values for "n," is arbitrary and can be significantly improved – in relation to what was already done in Fig. 9 – by a superior physics-based definition of what $h_{x|cb}$ is and how it can be obtained. This improved $n = 1$ approach is explained in Ranga Prasad et al. (2017), and a sample result has already been reported here in Eq. (32). Since the film thicknesses are small in Fig. 10 for Fig. 3a operations and the liquid film flows are laminar, these nucleate boiling-dominated high heat-flux shear-driven flows will typically have very small bubble diameters (microns to submicron scales) whose density and ebullition cycle (growth and departure durations) related frequencies – which increase with increased heat-flux, as in pool-boiling (Ghiaasiaan 2007) or macroscale nucleate boiling regime I in Fig. 1b – are at present poorly understood. This is because these mechanisms, unlike pool-boiling, are dictated by significantly weakened transverse gravity (or buoyancy) forces competing with other significantly weaker "inertial pinning force" and "viscous/pressure forces" at the time of bubble departure (when the pinning "surface-tension force" at the *effective* "contact line rim" goes to zero; see Phan et al. 2009; Zeng et al. 1993a, b). Though some studies in related areas exist (Zeng et al. 1993a, etc.), it is quite likely that the existing pool-boiling-based knowledge for mechanisms underlying the models for nucleation phenomena with regard to bubble diameters (Egorov and Menter 2004; Gerardi et al. 2010; McHale and Garimella 2010), activated nucleation site densities, and ebullition cycle frequencies (which are typically 0.5–3 mm in bubble diameters, 10^6–10^7 activated sites/m^2, and 40–200 Hz for refrigerants experiencing pool boiling under

relevant pressure and ΔT conditions considered for Figs. 6, 7, 8, 9, and 10) are not entirely applicable to thin-film microscale nucleate boiling associated with regions III and IV in Fig. 1b. This is likely because the relationship between changed microscale and nucleation controlling forces in the thin liquid film – along with submicron and adsorbed layer contact-line physics (Kandlikar and Grande 2003) – is different.

Furthermore, for low heat-flux and mass-flux cases ($\bar{q}''_w < 0.2$ W/cm^2, G < 20 kg/m^2.s, and refrigerants considered here), preliminary annular flow-boiling experiments (Gorgitrattanagul 2017 and Narain et al. 2012) and theoretical/computational $h_{x|cb}$ estimates (Ranga Prasad et al. 2017) do indicate that the thinner downstream liquid flows (indicated by region VI in Fig. 1b, e.g., with Δ(x) in 1–10 μm thickness range) exhibit suppressed nucleation convective boiling (i.e., $h_{x|cb} \gg h_{x|nb-micro}$). Since total heat transfer coefficient h_x (in equations such as Eq. (33)) can be experimentally assessed through relations such as $q''_{w|Expt}(x) \equiv h_x{}^* \Delta T(x)$, where $\Delta T(x) \equiv T_w(x) - T_{sat}(p_{in})$ and $T_w(x)$, like wall heat-flux $q''_{w|Expt}(x)$, is also experimentally measured, one can use computational simulations under the assumption of suppressed nucleation (as discussed in Ranga Prasad et al. 2017) and obtain superior $h_{x|cb}$ estimates for experimentally measured boiling surface temperatures $T_w(x)$. With h_x known experimentally and $h_{x|cb}$ known from proper physics-based CFD, $h_{x|nb-micro}$ can be accurately estimated through the defining relationship given as:

$$h_x \equiv h_{x|nb-micro} + h_{x|cb} \tag{61}$$

Therefore, to make use of Eq. (61), the computationally obtained correlations for $h_{x|cb}$ for different wall temperature values – obtained in the structural format of Eq. (11) – one must use those experimentally measured values of $T_w(x)$ appearing in $\Delta T(x)$ that are associated with the corresponding experimentally measured values of $q''_{w|Expt}(x)$. Thus, as in Ranga Prasad et al. (2017), this recommendation for estimating $h_{x|cb}$ does the following: (i) it defines what $h_{x|cb}$ is for suppressed (real or hypothetical) nucleation annular flow boiling under identical flow-determining boundary conditions, and (ii) it realizes that though nucleation will actually impact convective boiling's thermal boundary layers, it puts all such effects (including direct nucleation effect) in the definition of $h_{x|nb}$ through Eq. (61).

The above CFD-enabled $h_{x|cb}$ estimate has another advantage; such hypothetically suppressed nucleation assumption CFD results when compared with experiments, where an actual nucleation suppression occurs (typically at low mass and heat-flux values conducive to CHF avoiding stable dry-out, and at thin-film downstream locations), can help identify the location where suppression of nucleation begins. This approach is being used (Gorgitrattanagul 2017; Sepahyar 2018) toward locating (and eventually developing a criterion/correlation) and obtaining *a priori* information about conditions under which nucleate boiling contributions to h_x can be considered to be effectively suppressed (see zones V and VI in Fig. 1b).

5.1.1 Low Heat-Flux and low Mass-Flux Cases and $h_{x|cb}$ Estimates

First principles-based accurate estimates of $h_{x|cb}$ under the assumption of hypothetically suppressed nucleation are fairly recent (Ranga Prasad et al. 2017) and are currently available only for limited low range of heat-flux and mass-flux values, as in Eq. (32). The development and implementation of CFD algorithm in Ranga Prasad et al. (2017) are similar to the ones proposed for annular flow condensation (Naik and Narain 2016; Naik et al. 2016). These include algorithm development, which, in turn, are based on analytical approaches – covering both modeling and numerical methods (also see ▶ Chap. 3, "Numerical Methods for Conduction-Type Phenomena").

A sample annular flow-boiling simulation for FC-72 (under the assumption of suppressed nucleation and laminar vapor/laminar liquid cases) on the bottom plate of a rectangular cross-sectional horizontal channel, as in Fig. 3a, is considered here for exhibiting its potential – including prediction capability for $h_{x|cb}$. The assumption of no nucleation is made, not necessarily to say that the annular flow is actually occurring in the suppressed nucleation mode but to accomplish the following:

(i) Obtain $h_x \cong h_{x|cb}$ values as a function of quality X (see Fig. 18) for uniform temperature (or heat-flux) prescription at the wall over $0 \leq x \leq L$ (see Fig. 3a) and use such results to propose correlations (see Eq. (32) in Sect. 3).
(ii) Obtain key flow-physics details – such as film thickness versus distance variation (Fig. 19a), liquid-vapor velocity, temperature, pressure profiles (Fig. 19b-d), flow streamlines (Fig. 19e), etc.
(iii) Obtain and correlate, using nonlinear stability approach (see Naik and Narain 2016; Naik et al. 2016), the criteria for transition from non-annular to annular flow-regimes as applied to suppressed nucleation flow boiling (Ranga Prasad

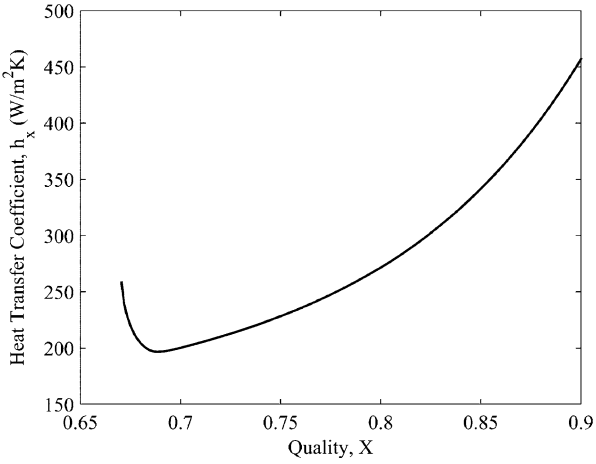

Fig. 18 Plot of $h_x = h_{x|cb}$ versus quality X as computationally obtained. The saturated annular flow boiling in Fig. 3a is for a channel geometry h = 2 mm, $\Delta T = 10\ ^\circ C$, fluid is FC-72, inlet quality $X_{in} \cong 0.65$, mass-flux $G = 13.98\ kg/m^2.s$, and $p_0 = 105.1\ kPa$

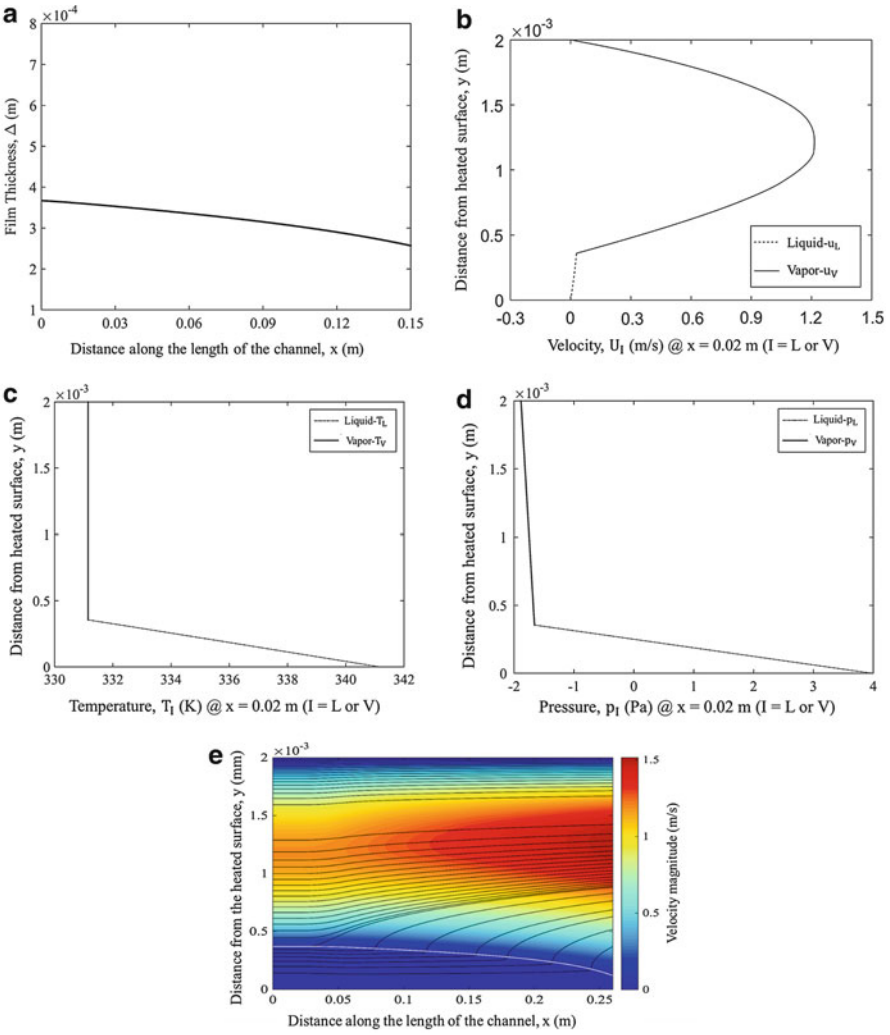

Fig. 19 Flow conditions are same as in Fig. 18. **(a)** Plot of film thickness versus distance. **(b)** Liquid and vapor velocity profiles are indicated at x = 0.02 m. **(c)** Plot of temperature profile at x = 0.02 m. **(d)** Plot of pressure profile at x = 0.02 m. **(e)** Streamline patterns. The mass flow rate between two adjacent (unequally spaced) streamlines is the same

et al. 2017) – and seek, in future, its appropriate modifications by comparing the results with experimental results for nucleate boiling dominant flows.

(iv) Compare $h_{x|nb}$ results with low heat-flux and low mass-flux annular boiling experiments (Gorgitrattanagul 2017; Narain et al. 2012) to obtain and correlate the estimates for locating the "points/zones" of onset of growing, diminishing, and suppressed nucleation annular flows. These are likely to occur (as in

regions III–V in Fig. 1b), for a given fluid across a certain surface in the parameter space of confinement number $Co \equiv \sqrt{\sigma/\left(g(\rho_L - \rho_V)\Delta(x)^2\right)}$, liquid film Reynolds number $Re_L(x)$ ($\equiv G(1 - X(x))/\mu_L$), and, possibly, one or two other parameters.

(v) By obtaining experimental values of h_x for annular flow-regimes, along with theoretical/computational values of $h_x = h_{x|cb}$, propose more reliable decomposition of h_x in the form of Eq. (61).

(vi) Use laminar liquid/laminar vapor or laminar liquid/turbulent vapor simulations (discussed in the next section) to obtain better pressure-drop versus boiler length (L) curves; compare the results with experiments as well as with results from existing pressure-drop models (see Sects. 3 and 4) to improve and propose new more accurate pressure-drop correlations for annular boiling.

5.1.2 Moderate to High Heat-Flux and Mass-Flux Cases and $h_{x|Cb}$ Estimates

As per currently available estimates shown in Fig. 9a, b, the $h_{x|cb}$ estimates have additional uncertainty than those of h_x itself (Eq. (31)). The planned estimation of $h_{x|cb}$ by CFD, under the hypothetical assumptions of negligible/suppressed nucleation, laminar liquid, and turbulent vapor flows in the structure of Eq. (61) is feasible, though it is expected to be more approximate as compared to laminar/laminar approach described in Sect. 5.1.1. This is because of the need to use appropriate turbulence models for the vapor phase that is also consistent with the correct interfacial shear and vapor-side components of interfacial velocity – which can be inputted and indirectly assessed with the help of a synthesis between experiments (involving measured values of pressure-drop and exiting liquid flow rate) and simulations. Even for the hypothetical absence of nucleation, with vapor streamlines (see Fig. 19e) suggesting the existence of a thin "near interface" laminar layer in the vapor phase that will always be present adjacent to the thin laminar liquid flow, there is a possibility that – at high vapor-phase Reynolds numbers $Re_V(x)$ – there will be a more significant interaction between the typical indeterminate *interfacial* waves (or laminar turbulence; see Naik and Narain 2016; Naik et al. 2016; Narain et al. 2015) and *vapor-phase turbulence*. This may change the interfacial shear values (from those obtained from laminar liquid flow and near-interface laminar vapor flow assumptions and new modeling and new synthesis with experiments will become quite important).

Therefore, for accurate estimation of $h_{x|cb}$ for such flows, it is proposed that, to start simulations, it would be appropriate to use initial interfacial shear estimates (e.g., values obtained from the laminar/laminar algorithm in Ranga Prasad et al. (2017)) with an appropriate adjustable scalar multiple, and then one should obtain the scalar multiple in a way that one obtains agreement with experimentally measured values of pressure-drop with experimentally measured boiling surface temperature values as thermal boundary condition. Note that the *ad hoc* factor adjusted in the laminar liquid and turbulent vapor simulations – with vapor turbulence modeled

by an appropriate Reynolds-averaged Navier-Stokes (RANS) or large eddy simulation (LES) approach, with user-provided and iteratively improved values of interfacial shear – involves an effectively steady interface assumption. The adjusted values of the *ad hoc* factor – once they produce consistent agreement with corresponding measurements/estimates of expected pressure-drop, an interfacial shear estimating modeling approximation – can be correlated under proper nondimensional structure.

Besides the computational estimate for $h_{x|cb}$, recall that results from experiments continue to yield total HTC h_x values through $q''_{w|Expt}(x) \equiv h_x * \Delta T(x)$, where $\Delta T(x) \equiv T_w(x) - T_{sat}(p_{in})$ and boiling surface temperature $T_w(x)$, like wall heat-flux $q''_{w|Expt}(x)$, is also an experimentally measured value. With h_x and $h_{x|cb}$ known, $h_{x|nb\ -\ micro}$ can be estimated – though more approximately than in Sect. 5.1.1 – through the defining relationship given in Eq. (61).

Also note that actual experimental values of film thickness $\Delta_{Expt}(x)$ in the presence of nucleation are likely to be somewhat different than the CFD predicted values of film thickness $\Delta_{CFD}(x)$, obtained under the assumption of no nucleating bubbles.

Pressure-drop predictions from above-described modeling efforts, in conjunction with experimental measurements and existing pressure-drop correlations (see Sects. 3 and 4), can also improve the existing pressure-drop correlations.

The above-described approach for $h_{x|cb}$ estimates/correlations, along with further refined estimates for total h_x obtained through proposed new experiments (along with existing ones, as used in Kim and Mudawar 2013c), would again help elucidate heat transfer mechanisms through the simple, but approximate, model: $h_x = h_{x|nb} + h_{x|cb}$ – which is an $n = 1$ version of Eq. (33).

The proposed CFD would also help in providing improved understanding of the laminar liquid/turbulent vapor flow physics such as the ones shown in the Sect. 5.1.1 for laminar liquid and laminar vapor flows.

5.2 Annular Flow Condensation

As discussed in Sects. 3 and 4, there are several empirical correlations for heat transfer coefficient h_x as well as annular to non-annular flow-regime transition criteria. For the proposed innovative condenser and its design discussed in Sect. 4, motion of the liquid film on a wetting (or hydrophilic) condensing surface avoids the complexities of dropwise condensation. Despite this, correlation for h_x and transition criteria from annular to non-annular flow-regimes are currently lacking in quality and accuracy and, therefore, need to be made much more accurate for effective design calculations (such as the ones used in Sect. 4). Again, as discussed earlier through Fig. 17, such improvements can be accomplished through CFD-and-experiment synthesis approach for improvements in h_x and flow-regime maps. The status and need for such improvements are discussed next.

5.2.1 Low Heat-Flux and Low Mass-Flux Annular Cases

First principles CFD-based accurate estimates (e.g., DNS for laminar condensate/laminar vapor cases in Fig. 3b) is now possible (Naik and Narain 2016; Naik et al. 2016; Narain et al. 2015) – at least for common refrigerants operating at $G < 20$ kg/m^2 s and $\overline{q}''_w < 0.3$ W/m^2. The CFD/DNS for these laminar/laminar cases can accomplish the following:

(i) Obtain h_x values as a function of distance x and quality X (see Fig. 20a, b).
(ii) Besides film thickness versus distance variation with x (Fig. 21a), they can obtain key flow-physics details for velocity, pressure, and temperature profiles (y-variation) of liquid and vapor phases at a representative x-location (Fig. 21b), annular to non-annular transition criteria by nonlinear stability analysis (see Fig. 22 and Naik et al. 2016), streamline patterns for shear-driven flow versus gravity-driven flow (Fig. 23), etc.
(iii) Use laminar liquid/laminar vapor flow assumptions based on pressure-drop predictions to improve existing pressure-drop correlations – by comparison-based modification of the predicted results toward agreement with reliable experimental data – or propose new pressure-drop correlations.

5.2.2 Moderate to High Heat-Flux and Mass-Flux Annular Flow Cases

The CFD support for laminar liquid turbulent vapor annular condensing flow predictions in Sect. 4 is complicated for reasons similar to convective flow-boiling cases discussed in Sect. 5.1.2.

For approximate estimation of h_x for such flows, it would again be helpful to model interfacial shear, to begin with, by some scaling factor multiple of the values that are associated with some suitable initial estimates (e.g., those obtained from laminar liquid and laminar vapor simulations-experiments synthesis-based correlations). The assumed factor could subsequently be computationally adjusted in a way

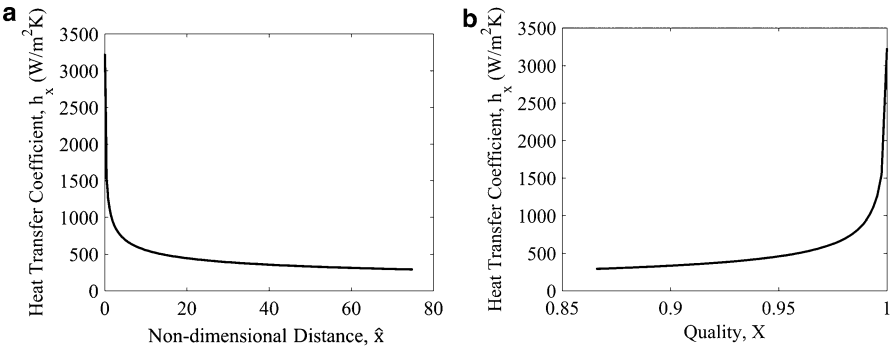

Fig. 20 **(a)** Plot of the heat transfer coefficient vs nondimensional distance. **(b)** Plot of heat transfer coefficient vs quality (run parameters: fluid – FC-72, U = 1 m/s or G = 13.98 kg/m^2.s, $p_0 = 105.1$ kPa, $\Delta T = 5$ °C, channel height = 2 mm)

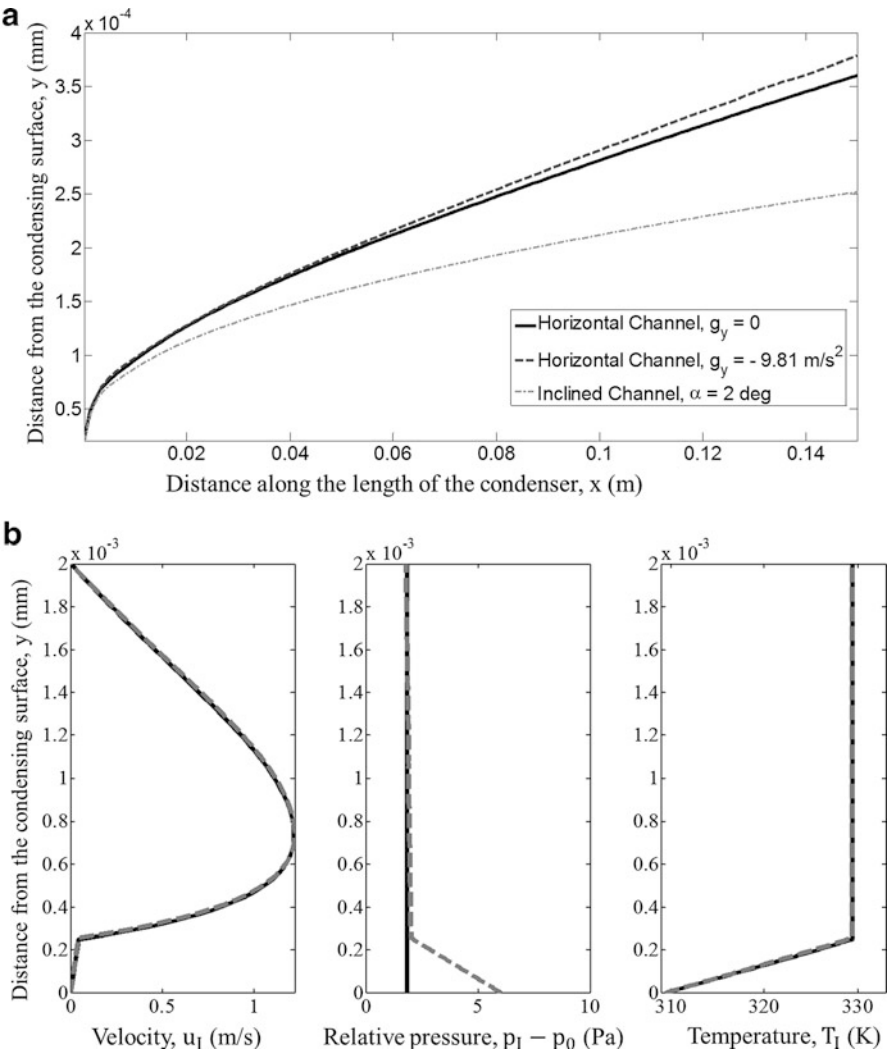

Fig. 21 **(a)** Plot of the two steady film thickness profiles shows negligible effects of transverse gravity. **(b)** Cross-sectional profiles for x-component of velocity (U_I), relative pressure "$p_I - p_0$," and physical temperature T_I at $x^p = 0.08$ m location in Fig. 3a. The solid black line curve is for the absence of transverse gravity, whereas the dashed gray line curve represents the presence of transverse gravity. (Run parameters: fluid – FC-72, U = 1 m/s or G = 13.15 kg/m^2.s, p_0 = 101 kPa, $\Delta T = 20$ °C, channel height, h = 2 mm)

that computational predictions of condensing surface's wall heat-fluxes (in case of temperature prescription) or wall temperatures (in case of heat-flux prescriptions) and pressure-drop predictions are in approximate agreement with experimental results for the flow-condenser – assuming experimentally measured/assessed values for most of these variables will be available for corresponding experimental runs.

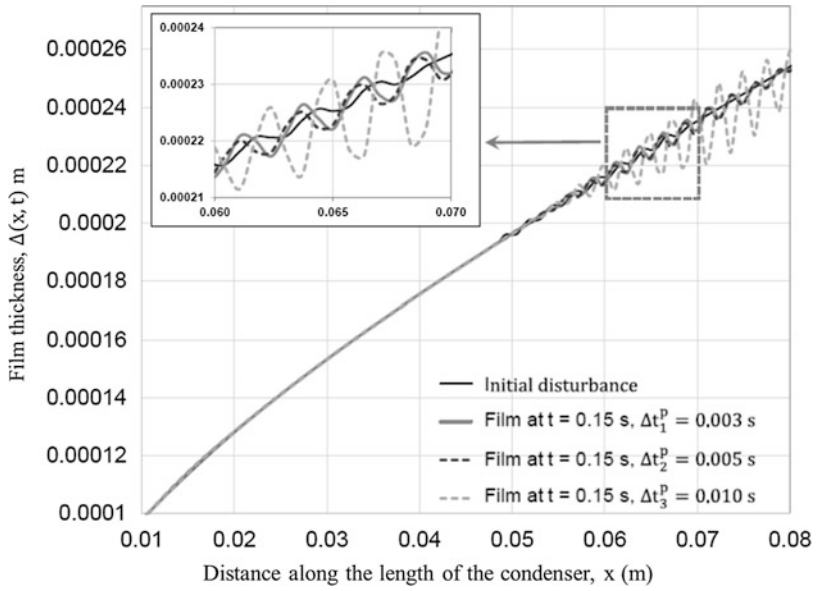

Fig. 22 The plots show $\Delta(x^p, t \cong T)$ values for an unsteady simulation for a condensing flow ($g_y = -9.81$ m/s^2) for which T = 0.15 s for an initial film $\Delta(x^p, 0) = \Delta_{steady}(x^p) + \Delta'(x^p, 0)$ with $\Delta'(x^p, 0) \neq 0$. The solutions are shown for three different time steps. The run parameters are same as in Fig. 21. The instability for $x^p > 0.06$ m corresponds to annular to non-annular transition and yields critical quality $X_{cr|A-NA}$ correlations as given in Sect. 3.2.2

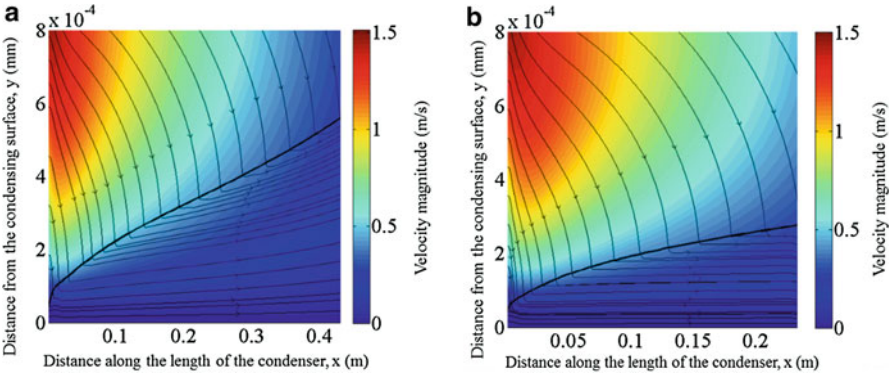

Fig. 23 Streamline patterns of a steady flow for **(a)** a horizontal channel and **(b)** a 2° downward inclined channel for annular condensation. The color map shows the velocity magnitude distributions. The run parameters are same as in Fig. 21

The above-described approach, if further developed, can be used to obtain improved h_x and pressure-drop correlations as well as improved understanding of the flow physics.

6 High Heat-Flux Advantages of Superposing High-Amplitude Standing Waves on the Interface for Steady-in-the-Mean Innovative Annular Flow-Boiling and Flow-Condensation Operations

In recent experimental works dealing with innovative operations of flow boiling and flow condensation (see Fig. 3 and Kivisalu et al. 2014) at low mass-flux and heat-flux values, the thinness of the liquid films (see Figs. 3 and 10) and their improved stability allowed superposition of large-amplitude standing waves on the interface (see Fig. 24c) created by acoustic standing-waves in the vapor-phase (of long wave-lengths relative to the device length) that, in turn, were created by pulsations introduced through oscillating flow rates (5-15 Hz) of the incoming vapor (and liquid, if needed) flows. There are other superior options for creating standing interfacial waves, but these are not discussed here. Such large amplitude standing wave realizations, as opposed to Fig. 24a, b realizations associated with steady non-pulsatile cases, are quite different in their micro-convection capabilities. The standing *interfacial* waves are formed over longer duration, as opposed to the short duration of forward moving interfacial traveling waves, as they result from the vapor-phase's long wave-length standing *acoustic* waves (and associated oscillatory interfacial shear) which, in turn, result from the fact that the flow-boiler exit is mostly obstructed in the predominant direction of vapor flow and pulsations-induced vapor-phase acoustic-waves, in the flow-direction, reflect from the exit (see Fig. 24c and Fig. 3a). As a result of superposition of such interfacial standing waves on a nearly steady interface location, as troughs got closer to the wetting surface under increasing amplitude of the waves, local time-varying heat-flux measurements indicated very high heat-fluxes (see Fig. 25 and Kivisalu et al. 2014). Consequently, both for annular flow condensation and annular flow boiling, the mean values of the measured heat-fluxes (at a representative location) increased significantly (see Fig. 26a, b). Note that experimentally attained local heat-flux enhancement (100-300%) for the flow-boiling case in Fig. 26a is much lower than the enhancements (up to 800%) observed for some comparable flow-condensation cases depicted in Fig. 26b.

The above-described pulsatile flow realization approach consists of:

(i) Selecting proper values of: inlet mass-flux, inlet quality, exit quality, film-thickness range, and length of the flow-boiler – as per design discussions in Section 4 – and attain a representative steady annular flow realization indicated by "point" A or "point B" in Fig. 1b, c.

(ii) Employing energy efficient ways to introduce suitable amplitudes of inlet pressure or flow-rate pulsations imposed on the incoming vapor flow (and liquid flow, if needed) – ensuring inlet flow rate value (which includes a selected range of recirculating vapor flow rates) always lies within a suitable range. In case of high heat-flux boiling, the extra mechanical power available at the exit of the boiler is used, in the arrangement of Fig. 3a, to maximize the use of by-pass valve and minimize the need for a recirculation-aiding compressor.

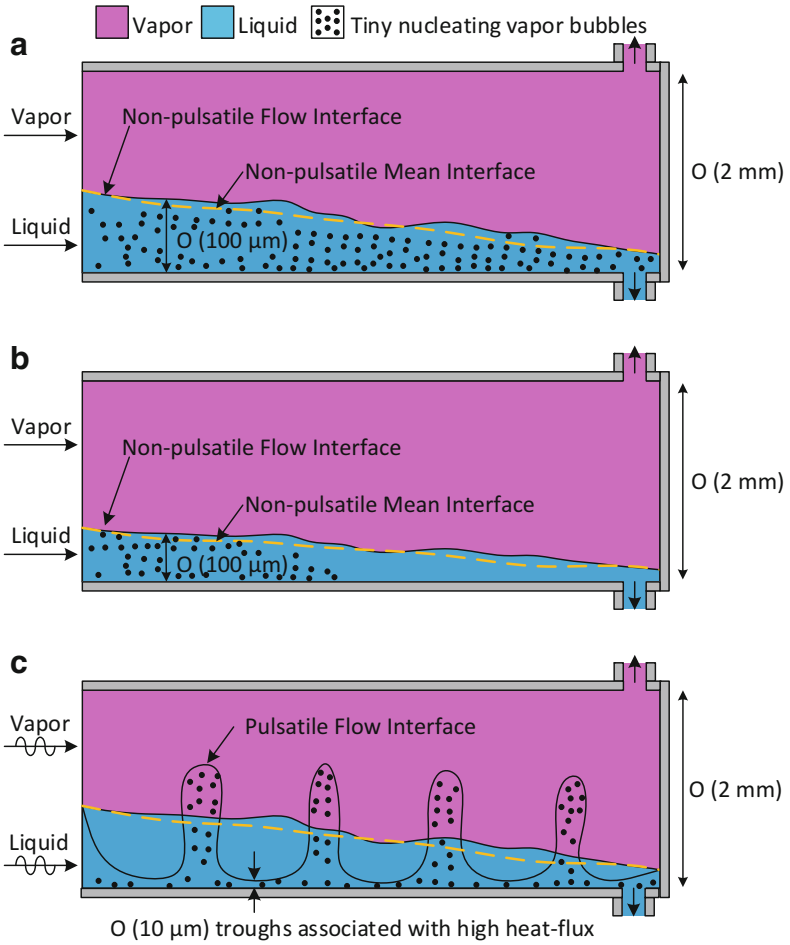

Fig. 24 **(a)** Non-pulsatile steady innovative annular flow-boiling operations (Fig. 3a) at high heat and mass fluxes (under use of common refrigerants) is dominated, as per Sect. 4 estimates, by tiny nucleating bubbles (of micron to sub-micron diameters, and represented by "dots") even for the steady annular regimes involving film thicknesses in the range of 50–300 μm. **(b)** Non-pulsatile steady annular flow boiling (arising from controlled recirculating vapor flow-rate at the inlet) at low mass and heat-fluxes may experience suppressed nucleation at sufficiently low film-thickness locations realized under conditions of low inlet film thickness $\Delta_0 \sim 100$–300 μm. **(c)** Depiction of long term and large amplitude standing interfacial waves. Large dynamic heat-flux enhancements are experienced at the "troughs," see Fig. 25

(iii) Using primarily closed end exit condition (Fig. 3a, b) for the axial direction of the vapor flow to reflect acoustic signals (associated with vapor flow pulsations) in the vapor phase to establish standing wave patterns. This is done to transform, over time, forward-moving short duration interfacial waves into standing

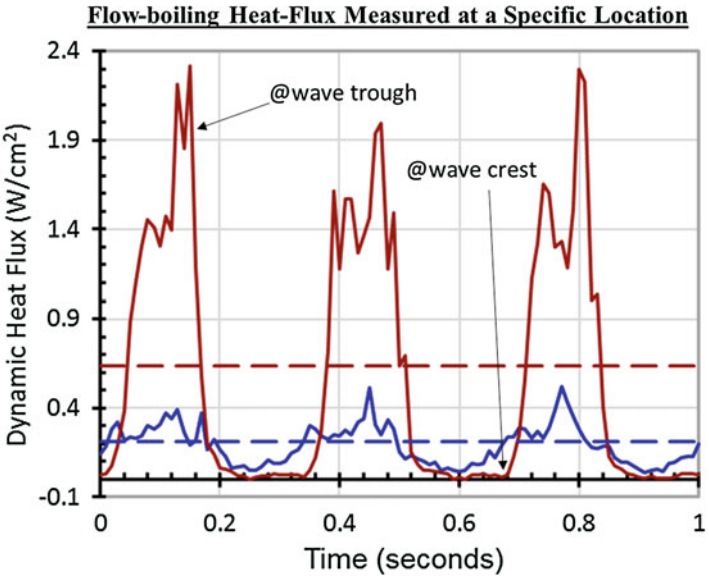

Fig. 25 Time-varying boiling heat-flux without (lower average) and with (higher average) imposed inlet liquid-vapor pulsations, measured by a flush-type heat-flux meter. The dashed lines represent long-term (~40 min) averages

interfacial wave patterns shown in Fig. 24c, and such realizations are observed in the experiments by Kivisalu et al. (2014). For creating large-amplitude standing waves, alternative and more technology-friendly approaches are possible and are being explored.

(iv) Using controlled thinness (50–300 μm) of the liquid film flow to stabilize the wavy film. This allows both large amplitude standing wave formation and, concurrently, reduced and insignificant chances of liquid entrainment (even for high mass-flux cases).

Under aforementioned conditions of steady-in-the-mean pulsatile flow realizations, the heat transfer enhancements shown in Fig. 26a, b are believed to result from the following hypotheses.

First, it is assumed that the flow-boiling enhancements in Fig. 26a may have, at higher heat-fluxes, more explosive nucleating micro-bubble (micron or sub-micron diameters) presence and more significant heat-transfer contributions through $h_{x|nb\text{-}micro}$, which is already (i.e., for low mass and heat-flux cases considered here) up to 80% of the total HTC given by Eq. (61) – representative calculations supportive this assertion are described in Gorgitrattanagul (2017). Furthermore, the 100-300% heat-flux enhancements shown by the solid-curve (for low heat-flux cases) in Fig. 26a may not be realized, as desired and indicated by the dashed curve in Fig. 26a (or the corresponding red curves in Figs. 1b-c), for cases involving higher heat-flux

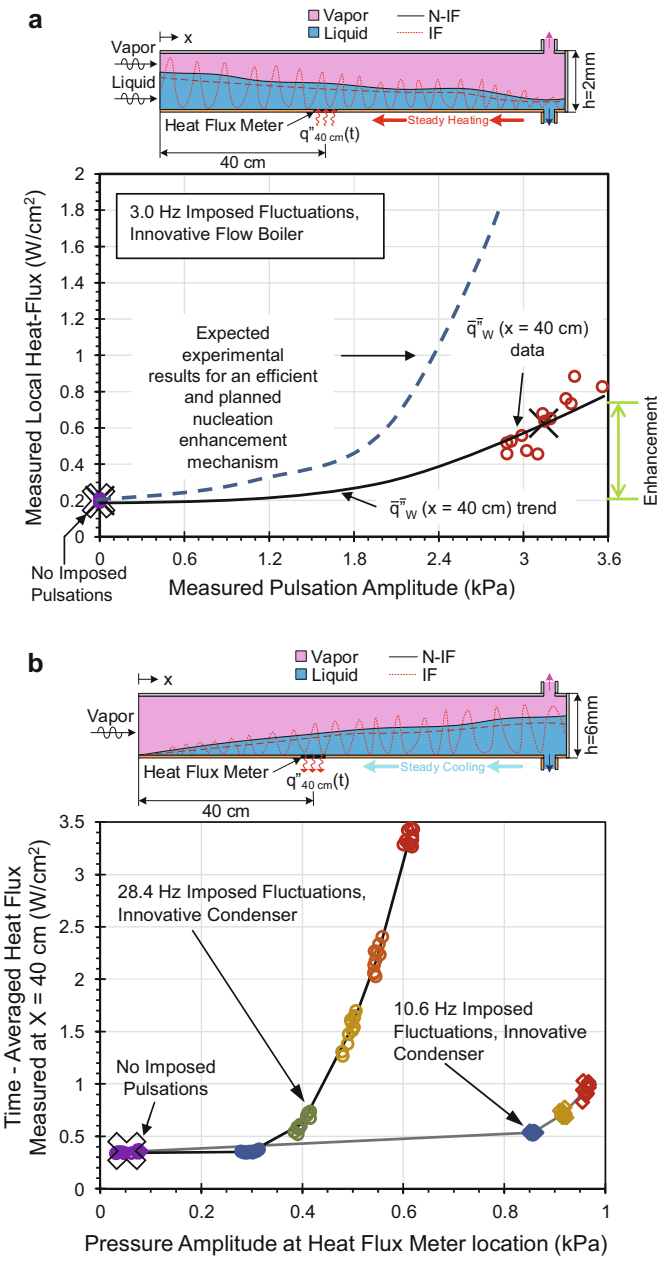

Fig. 26 **(a)** Increase of average heat-flux with amplitude of imposed vapor fluctuations for a representative low mass-flux annular flow-boiling situation (Kivisalu et al. 2014). **(b)** Increase of average heat-flux with amplitude of imposed vapor pulsations for a representative low mass-flux annular condensing flow situation (Kivisalu et al. 2014)

impositions. This is expected due to limitations in bubble-departure mechanisms available to the flow at the higher heat-flux imposition levels. Note that higher values of nucleation site densities, increased bubble generation frequencies, and limited ranges of bubble departure diameters are expected – and, as a result, the micro-bubbles may not be effectively carried away by the explosive levels of nucleation expected for heat-flux impositions in the range of 500-1000 W/cm^2. Despite this, the enhancement levels indicated by the dashed curve in Fig. 26a is realizable for high heat-flux cases by using additional supplementary approaches – which are to be described elsewhere.

However, at low heat-flux levels, there could be very significant enhancements, as shown in Figs. 26a and b. This is because classical convective contribution $h_{x|cb}$ significantly increases in Eq. (61) for flow boiling and for flow condensation (for which $h_x = h_{x|cb}$) considered here. The reason being convective heat-transfer mechanisms, associated with the thin film steady flow-physics of flow boiling (or flow-condensation sans nucleating bubbles) depicted in Figs. 24a-b, significantly changes to incorporate new mechanisms associated with the new bulk micro-convection shown in Fig. 24c. The mechanisms present for Fig. 24c are described here with the help of Figs. 27a-b (which exhibit presence of some of the known mechanisms present in pool-boiling, which is depicted in Fig. 28 and recalled here for relevant discussions). The proposed new bulk $h_{x|cb\text{-}micro}$ enhancement phenomena, as described below, is the sole contributor for the flow condensation (which has no nucleating bubbles) enhancement case in Fig. 26b. It is hypothesized that contact-line flow-physics of Fig. 28 (well known for macro-scale pool boiling) appears here – for the micro-scale thin liquid film's flow-physics – in a modified way to yield high heat-fluxes observed in Fig. 26.

For these micron-scale (O(100 μm)) thin liquid film flows, with superposed large amplitude standing waves (such that the liquid thickness at troughs are O(10 μm)), consider the following for Figs. 27a-b::

- The three intersecting circles represent effects of interaction zones of nm-scale, mm-scale, and macro- or mm-scale phenomena.
- Between the liquid-vapor interface (formed by the curve at the juncture of blue and pink zones) and the solid-like adsorbed liquid layer (marked yellow), the liquid flow at the troughs experience reduced pressure and slip-like reduced shear that allow enabling micro-convective motion upstream and downstream of the troughs – as well as the requisite through flow at the troughs. The low pressure at troughs is enabled both by the surface-tension and curvature effects near the vapor-liquid interface as well as by the liquid's interface with the adsorbed (marked yellow) layer through negative tensile stresses (disjoining pressure) between the lower solid-liquid interface and the liquid above. This low pressure at troughs, besides allowing forward liquid motion (straight arrow in Fig. 27a) between the upstream crest-region adjacent to the trough, also enables micro-circulation associated convective heat transfer enhancements within neighboring crests (recirculation arrows in Fig. 27a). The micro-circulation in the macro-region of Fig. 28 are also enabled by analogous phenomena. The expected and

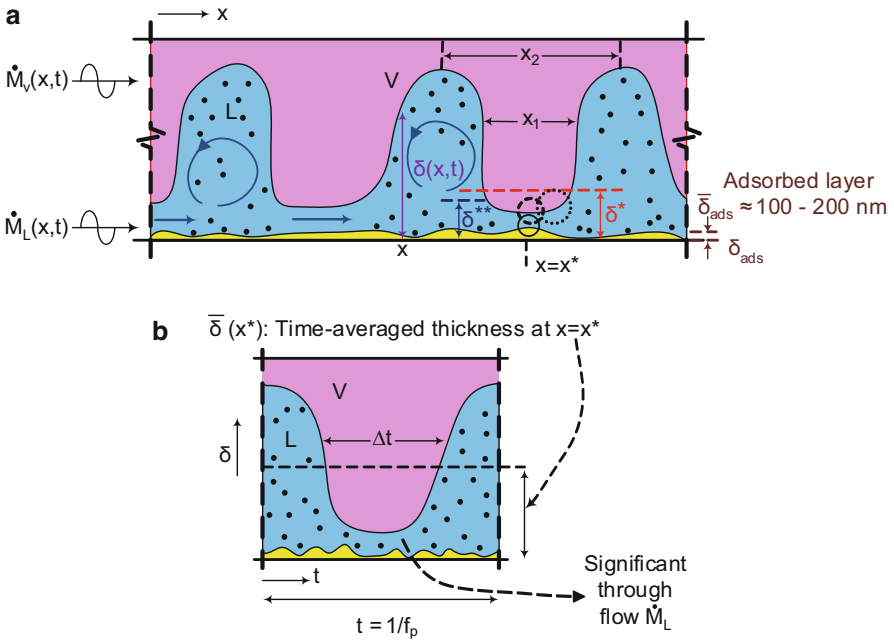

Fig. 27 **(a)** Near-interface schematic of dynamics of the instantaneous spatial nondimensional film thickness profile ($\delta \equiv \Delta/h$) associated with μm-scale wavy film flows (over a wetting surface) encountered in pulsatile flow boiling (or flow condensation). The three intersecting circles in the figure, respectively, represent zones where nm-scale, μm-scale, and mm-scale phenomena interact with one another. **(b)** Time-varying film thickness profile for location $x = x^*$ in Fig. 27a. The film thickness time history at a trough location ($x = x^*$) over an imposed time $t_P = 1/f_p$, where, f_p is the imposed vapor-phase pulsation frequency, is such that the crests and troughs "dwell" times weighted by instantaneous heat-flux values, are dominated by the contributions of the troughs to the local time-averaged heat-flux (Fig. 25)

requisite low shear at the troughs in Fig. 27 is also hypothesized here to arise from mechanisms similar to the low shear (rather stick-slip behavior) expected near the contact-line rim of the pool-boiling bubbles in Fig. 28. For the pool-boiling case in Fig. 28, low shear at the contact-line rim possibly arises from the fact that the micro-region liquid film in Fig. 28b has intermediate slip enabling solid-like behavior adjacent to the adsorbed liquid region (or, macroscopically, the dry region) and fluid-like no-slip behavior adjacent to the macro-region. This lubricated slip-like behavior (perhaps assisted by temperatures and phase-change in a way that is not completely understood) is a key phenomenon that enables realization of such large bubble departure frequencies (5 – 500 Hz) in the pool-boiling case of Fig. 28, where the surrounding stagnant liquid pool's inertia is large and yet the frequencies keep increasing with increasing heat-flux.

- Micro-scale nucleation (of bubbles) in the flows of Fig. 24 and Fig. 27 can be encouraged, diminished, or suppressed over a range of thicknesses for thin film

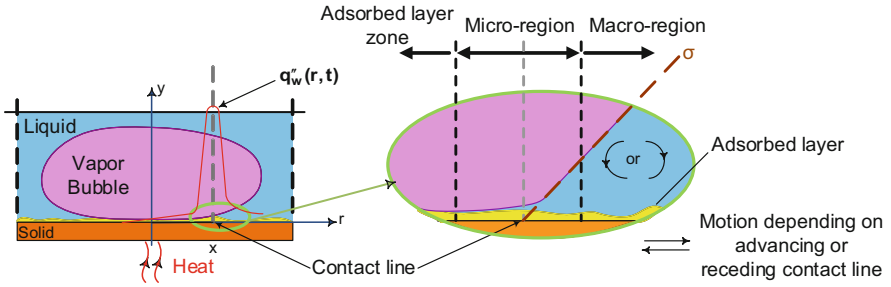

Fig. 28 Reduced pressure (disjoining pressure effects) and reduced shear (slip-like conditions) at the contact line of nucleating bubbles enable high heat-flux values at the contact line. This is due to alternating and vigorous recirculating motion – at reasonably high frequency, typically at about 5-500 Hz – of the liquid near the nano-micro-macro layer thick contact-line zone in the presence of phase-change and solid-liquid and liquid-vapor interfaces. Left and right figures are views obtained for the same contact-line zone when the smallest resolvable length scales are, respectively, approximately O(100 μm) and O (100 nm)

annular flow boiling on wetting surfaces (or super-hydrophilic surfaces with nucleation sites) – see regions III-V in Figs. 1b-c. And yet the aforementioned contact-line physics assisted micro-convection advantages in Fig. 27, as in the micro-region of Fig. 28 for mm-scale nucleating bubbles, is approximately retained with the following differences: (i) the wetting surface in Fig. 27 is always wet (except downstream of stable dry-out points, not shown) with an O(10 μm) micro-layer of liquid at the trough (which is absent in Fig. 28 where the vapor is in contact with solid-like adsorbed layer), and (ii) there is continued forward flow through the "tens of microns" thick "layer" formed at the wave-troughs.

The above-described flow physics for pulsatile operations of annular flow-boilers and flow-condensers – along with suitable design modifications for the non-pulsatile flows in Sect. 4 and some hardware modifications for the flow-loop design (see Kivisalu et al. 2014 and Gorgitrattanagul 2017) – enable development of high heat-flux devices embedded in proper flow loops that are equipped with suitable flow controls (see, e.g., Fig. 29 for a flow loop being used for science experiments and Sepahyar 2018) that are capable of removing heat from the boiling surface at the desired 500–1000 W/cm^2 levels.

7 Summary

This review article accomplishes the following purposes:

- The Introduction (Sect. 1) and the subsection "Flow and CHF-Related Instabilities" of Sect. 2.2 provide a coherent and clarifying review of traditional in-duct flow-boiling processes (with some emphasis on flow condensation). These cover

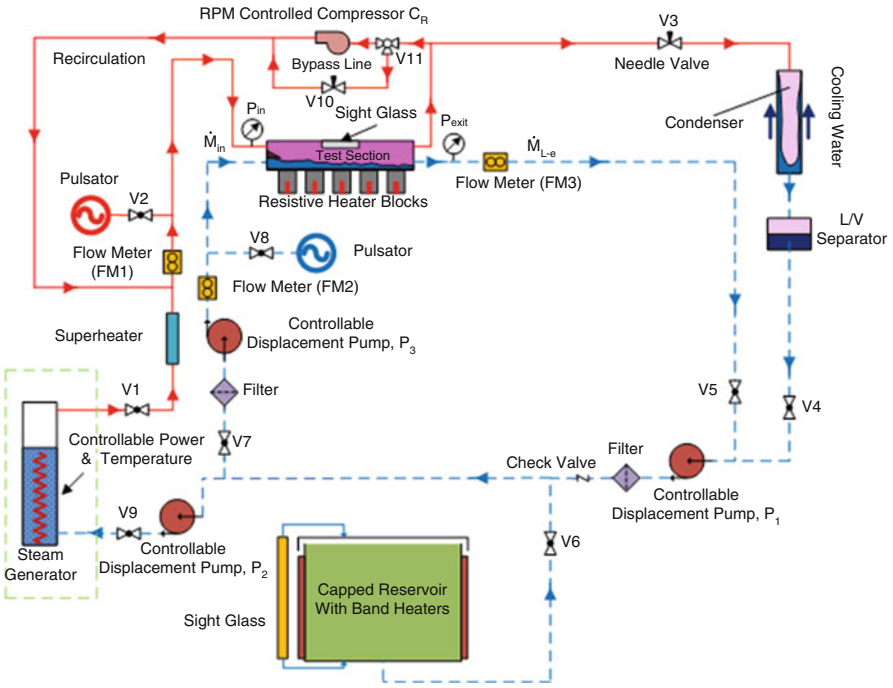

Fig. 29 The broad new flow-loop structure for innovative flow-boiling experiments using water

the more complex issues and physics associated with realization of different flow-regimes, local heat transfer coefficient variations, various instabilities, CHF, etc.

- The review maintains a direction for readers interested in developing science and technology of high heat-flux thin film (or annular) flow boiling – and flow condensation – that employ innovative millimeter-scale hydraulic diameter devices of suitable lengths and stacking arrangements. This is facilitated by introducing the operating principle of high heat removal innovative devices early on in the article (Fig. 3) and then selecting the review of pertinent items (from the broader subject area of boiling/condensing flows) that are relevant to the physics, modeling, simulations, and experimental issues for such devices. This review also addresses the narrow "window of opportunity" that exists (as discussed through performance curves of typical millimeter-scale devices in Figs. 1, 3, 4, and 5 along with hypotheses and related physics given in Sect. 6), as discussed in recently published literature, for further development of this approach.
- Besides the focus indicated above, the other primary purpose of the review was to elucidate existing knowledge base of correlations, and their relevance to the proposed innovations. Toward this, Sect. 2 presents the framework within which current and future knowledge dealing with empirical correlations for heat transfer coefficient, pressure-drop, void fraction, flow-regime transition, etc.,

should be structured. Sect. 3 attempts to review and summarize the specifics of some of the relevant, better established (including latest and accurate) knowledge that are available in this area.

- Sect. 4 makes the review of some apparently scattered topics reviewed in Sects. 2 and 3 more coherent. This is done by showing how all these approximate, quantitative, and correlation-based knowledge in Sects. 2 and 3 become useful when they come together in a design tool for new experiments and new systems that involve innovative flow-boiler and flow-condenser operations, as introduced earlier.
- Even as successful new designs and experimental flow loops can be initiated and completed with the help of existing knowledge described in Sects. 1, 2, and 4 and the newer knowledge described in Sect. 6, there remains an ongoing need – both for *steady* and *steady-in-the-mean* (with *superposed large-amplitude interfacial standing waves*) cases – for more refined correlations as tools for assisting more accurate design of innovative systems (such as the one in Fig. 29 or its miniaturized versions) and their flow-and-heating control techniques. The principles and samples for developing such refined correlations are discussed in Section 5. When the innovative devices shift their *steady* operations to the mode of operation with *superposed large-amplitude interfacial standing waves or other enhancement approaches* (to secure operational benefits as indicated by curves $I_{1-(ii)}$ and $I_{2-(ii)}$ in Fig. 1b, c), the preliminary experimental design approach for realizing the underlying steady flows are covered by this review and cited references. Development of correlations and discussion of system design and flow-control issues for developing *a priori* design and assessment tools for this promising operation mode involving *superposed large-amplitude interfacial standing waves or other approaches* are not part of this review – these constitute an active and developing area of research.

8 Cross-References

- ▶ Boiling and Two-Phase Flow in Narrow Channels
- ▶ Boiling on Enhanced Surfaces
- ▶ Film and Dropwise Condensation
- ▶ Flow Boiling in Tubes
- ▶ Heat Pipes and Thermosyphons
- ▶ Mixture Boiling
- ▶ Nucleate Pool Boiling
- ▶ Numerical Methods for Conduction-Type Phenomena
- ▶ Single- and Multiphase Flow for Electronic Cooling

Acknowledgment This work was supported by NSF grant CBET-1402702. All figures, which are schematics in their nature, are contributions of Mr. Patcharapol Gorgitrattanagul, a graduate student at MTU.

References

Agostini B, Bontemps A (2005) Vertical flow boiling of refrigerant R134a in small channels. Int J Heat Fluid Flow 26(2):296–306

Agostini B, Fabbri M, Park JE, Wojtan L, Thome JR, Michel B (2007) State of the art of high heat flux cooling technologies. Heat Transf Eng 28(4):258–281

Akers W, Rosson H (1960) Condensation inside a horizontal tube. Chem Eng Prog Symp Ser 56(30):145–150

Avedisian CT (1985) The homogeneous nucleation limits of liquids. J Phys Chem Ref Data Monogr 14(3):695–729

Baker O (1953) Design of pipelines for the simultaneous flow of oil and gas. Fall Meeting of the Petroleum Branch of AIME. Society of Petroleum Engineers

Ball P (2012) Computer engineering: feeling the heat. Nature 492(7428):174–176

Basu S, Ndao S, Michna GJ, Peles Y, Jensen MK (2011) Flow boiling of R134a in circular microtubes—part II: study of critical heat flux condition. J Heat Transf 133(5):051503

Bergles A (1988) Fundamentals of boiling and evaporation. Two-phase flow heat exchangers. Springer, Dordrecht, The Netherlands

Bergman TL, Incropera FP, Dewitt DP, Lavine AS (2011) Fundamentals of heat and mass transfer. John Wiley & Sons, New York

Bertsch SS, Groll EA, Garimella SV (2009) A composite heat transfer correlation for saturated flow boiling in small channels. Int J Heat Mass Transf 52(7–8):2110–2118

Bohdal T, Charun H, Sikora M (2011) Comparative investigations of the condensation of R134a and R404A refrigerants in pipe minichannels. Int J Heat Mass Transf 54 (9–10):1963–1974

Bowring R (1972) Simple but accurate round tube, uniform heat flux, dryout correlation over the pressure range 0.7 TO 17 MN/m $ sup 2$(100 TO 2500 PSIA). Atomic Energy Establishment, Winfrith (England)

Carey VP (1992) Liquid-vapor phase-change phenomena. Series in chemical and mechanical engineering. Hemisphere Publishing Corporation, New York

Cavallini A, Zecchin R (1974) A dimensionless correlation for heat transfer in forced convection condensation. In: Proceedings of the sixth international heat transfer conference, pp 309–313

Cavallini A, Del Col D, Doretti L, Matkovic M, Rossetto L, Zilio C, Censi G (2006) Condensation in horizontal smooth tubes: a new heat transfer model for heat exchanger design. Heat Transf Eng 27(8):31–38

Chen JC (1966) Correlation for boiling heat transfer to saturated fluids in convective flow. Ind Eng Chem Process Des Dev 5(3):322–329

Cole R (1960) A photographic study of pool boiling in the region of the critical heat flux. AICHE J 6(4):533–538

Coleman JW, Garimella S (2003) Two-phase flow regimes in round, square and rectangular tubes during condensation of refrigerant R134a. Int J Refrig Rev Int Du Froid 26(1):117–128

Collier JG, Thome JR (1994) Convective boiling and condensation. Oxford University Press, Oxford

Cooper M (1984a) Heat flow rates in saturated nucleate pool boiling-a wide-ranging examination using reduced properties. Adv Heat Transf 16:157–239

Cooper M (1984b) Saturation nucleate pool boiling—a simple correlation. Inst Chem Eng Symp Ser 86(2):785–793

Cooper M (1989) Flow boiling—the 'apparently nucleate'regime. Int J Heat Mass Transf 32(3):459–464

Dalkilic AS, Wongwises S (2009) Intensive literature review of condensation inside smooth and enhanced tubes. Int J Heat Mass Transf 52(15–16):3409–3426

Das PK, Chakraborty S, Bhaduri S (2012) Critical heat flux during flow boiling in mini and microchannel-a state of the art review. Front Heat Mass Transf 3(1)

Dhillon NS, Buongiorno J (2017) Effect of surface roughness on the behavior of bubbles growing and departing from a heated surface. In: Summer heat transfer conference SHTC, Bellevue, 9–14 July 2017
Dhir V (1998) Boiling heat transfer. Annu Rev Fluid Mech 30(1):365–401
Dhir V, Liaw S (1989) Framework for a unified model for nucleate and transition pool boiling. J Heat Transf 111(3):739–746
Dobson MK, Chato JC (1998) Condensation in smooth horizontal tubes. J Heat Transf Trans ASME 120(1):193–213
Ducoulombier M, Colasson S, Bonjour J, Haberschill P (2011) Carbon dioxide flow boiling in a single microchannel–part II: heat transfer. Exp Thermal Fluid Sci 35(4):597–611
Egorov Y, Menter F (2004) Experimental implementation of the RPI wall boiling model in CFX-5.6. Staudenfeldweg 12:83624
Faghri A (1995) Heat pipe science and technology. Taylor and Francis, Washington DC
Fluent (2015) Version 16.2. Theory guide. ANSYS Inc., Canonsburg
Forster HK, Zuber N (1954) Growth of a vapor bubble in a superheated liquid. J Appl Phys 25(4):474–478
Forster H, Zuber N (1955) Dynamics of vapor bubbles and boiling heat transfer. AICHE J 1(4):531–535
Friedel L (1979) Improved friction pressure drop correlations for horizontal and vertical two-phase pipe flow. European two-phase flow group meeting, Paper E
Gerardi C, Buongiorno J, Hu L-W, Mckrell T (2009) Measurement of nucleation site density, bubble departure diameter and frequency in pool boiling of water using high-speed infrared and optical cameras. In: ECI International conference on boiling heat transfer, Florianópolis
Gerardi C, Buongiorno J, Hu L-W, Mckrell T (2010) Study of bubble growth in water pool boiling through synchronized, infrared thermometry and high-speed video. Int J Heat Mass Transf 53(19–20):4185–4192
Ghiaasiaan SM (2007) Two-phase flow, boiling, and condensation: in conventional and miniature systems. Cambridge University Press, Cambridge
Gorenflo D (1993) Pool boiling, VDI–heat atlas. VDI–Verlag, Düsseldorf. (English version)
Gorgitrattanagul P (2017) Temperature controlled flow-boiling of FC-72 under innovative operations that lead to experimental realization of annular flows in millimeter scale ducts – investigation of steady and pulsatile cases. Ph. D, Michigan Technological University
Grönnerud R (1972) Investigation of liquid hold-up, flow-resistance and heat transfer in circulation type evaporators, part IV: two-phase flow resistance in boiling refrigerants. Bull De l'Inst Du Froid, Annexe 1 533–542
Gungor KE, Winterton R (1986) A general correlation for flow boiling in tubes and annuli. Int J Heat Mass Transf 29(3):351–358
Haraguchi H, Koyama S, Fujii T (1994) Condensation of refrigerants HCFC22, HFC134a and HCFC123 in a horizontal smooth tube (2nd report). Trans JSME (B) 60(574):245–252
Haramura Y, Katto Y (1983) A new hydrodynamic model of critical heat flux, applicable widely to both pool and forced convection boiling on submerged bodies in saturated liquids. Int J Heat Mass Transf 26(3):389–399
Harirchian T, Garimella SV (2012) Flow regime-based modeling of heat transfer and pressure drop in microchannel flow boiling. Int J Heat Mass Transf 55(4):1246–1260
Hewitt GF, Roberts D (1969) Studies of two-phase flow patterns by simultaneous X-ray and flash photography. Atomic Energy Research Establishment, Harwell
Huang X, Ding G, Hu H, Zhu Y, Peng H, Gao Y, Deng B (2010) Influence of oil on flow condensation heat transfer of R410A inside 4.18 mm and 1.6 mm inner diameter horizontal smooth tubes. Int J Refrig 33(1):158–169
Jones BJ, Mchale JP, Garimella SV (2009) The influence of surface roughness on nucleate pool boiling heat transfer. J Heat Transf 131(12):121009
Kandlikar SG, Grande WJ (2003) Evolution of microchannel flow passages–thermohydraulic performance and fabrication technology. Heat Transf Eng 24(1):3–17
Kandlikar SG, Hayner CN (2009) Liquid cooled cold plates for industrial high-power electronic devices—thermal design and manufacturing considerations. Heat Transf Eng 30(12):918–930

Katto Y (1994) Critical heat flux. Int J Multiphase Flow 20:53–90
Katto Y, Ohno H (1984) An improved version of the generalized correlation of critical heat flux for the forced convective boiling in uniformly heated vertical tubes. Int J Heat Mass Transf 27(9):1641–1648
Kenning D, Cooper M (1989) Saturated flow boiling of water in vertical tubes. Int J Heat Mass Transf 32(3):445–458
Kim S-M, Mudawar I (2013a) Universal approach to predicting heat transfer coefficient for condensing mini/micro-channel flow. Int J Heat Mass Transf 56(1–2):238–250
Kim S-M, Mudawar I (2013b) Universal approach to predicting saturated flow boiling heat transfer in mini/micro-channels – part I. Dryout incipience quality. Int J Heat Mass Transf 64:1226–1238
Kim S-M, Mudawar I (2013c) Universal approach to predicting saturated flow boiling heat transfer in mini/micro-channels – part II. Two-phase heat transfer coefficient. Int J Heat Mass Transf 64:1239–1256
Kim S-M, Mudawar I (2013d) Universal approach to predicting two-phase frictional pressure drop for mini/micro-channel saturated flow boiling. Int J Heat Mass Transf 58(1–2):718–734
Kim S-M, Mudawar I (2014) Review of databases and predictive methods for pressure drop in adiabatic, condensing and boiling mini/micro-channel flows. Int J Heat Mass Transf 77:74–97
Kim SJ, Bang IC, Buongiorno J, Hu LW (2006) Effects of nanoparticle deposition on surface wettability influencing boiling heat transfer in nanofluids. Appl Phys Lett 89(15):153107
Kim S, Bang IC, Buongiorno J, Hu L (2007) Surface wettability change during pool boiling of nanofluids and its effect on critical heat flux. Int J Heat Mass Transf 50(19):4105–4116
Kivisalu MT (2015) Experimental investigation of certain internal condensing and boiling flows: their sensitivity to pressure fluctuations and heat transfer enhancements. Ph. D, Michigan Technological University
Kivisalu MT, Gorgitrattanagul P, Narain A (2014) Results for high heat-flux flow realizations in innovative operations of milli-meter scale condensers and boilers. Int J Heat Mass Transf 75:381–398
Kosky PG, Staub FW (1971) Local condensing heat transfer coefficients in the annular flow regime. AICHE J 17(5):1037–1043
Koyama S, Kuwahara K, Nakashita K, Yamamoto K (2003) An experimental study on condensation of refrigerant R134a in a multi-port extruded tube. Int J Refrig 26(4):425–432
Kumar R, Kadam ST (2016) Development of new critical heat flux correlation for microchannel using energy-based bubble growth model. J Heat Transf 138(6):061502
Kunkelmann C, Ibrahem K, Schweizer N, Herbert S, Stephan P, Gambaryan-Roisman T (2012) The effect of three-phase contact line speed on local evaporative heat transfer: experimental and numerical investigations. Int J Heat Mass Transf 55(7–8):1896–1904
Kuo C-J, Peles Y (2009) Flow boiling of coolant (HFE-7000) inside structured and plain wall microchannels. J Heat Transf 131(12):121011
Kurul N, Podowski M (1991) On the modeling of multidimensional effects in boiling channels. In: ANS proceeding of the 27th national heat transfer conference. American Society of Mechanical Engineers, New York
Lavieville J, Quemerais E, Mimouni S, Boucker M, Mechitoua N (2006) NEPTUNE CFD V1. 0 theory manual. NEPTUNE report Nept_2004_L1, 2 (3).
Lazarek G, Black S (1982) Evaporative heat transfer, pressure drop and critical heat flux in a small vertical tube with R-113. Int J Heat Mass Transf 25(7):945–960
Ledinegg M (1938) Instability of flow during natural and forced circulation. Die Warme 61(8):891–898
Lee J, Mudawar I (2009) Critical heat flux for subcooled flow boiling in micro-channel heat sinks. Int J Heat Mass Transf 52(13–14):3341–3352
Lemmert M, Chawla J (1977) Influence of flow velocity on surface boiling heat transfer coefficient. Heat Transf Boil 237:247
Li W, Wu Z (2010) A general correlation for evaporative heat transfer in micro/mini-channels. Int J Heat Mass Transf 53(9–10):1778–1787

Li W, Qu X, Alam T, Yang F, Chang W, Khan J, Li C (2017) Enhanced flow boiling in microchannels through integrating multiple micro-nozzles and reentry microcavities. Appl Phys Lett 110(1):014104

Linehard J, Dhir VK (1973) Extended hydrodynamic theory of the peak and minimum pool boiling heat fluxes. National Aeronautics and Space Administration, Washington, DC

Liu Z, Winterton R (1991) A general correlation for saturated and subcooled flow boiling in tubes and annuli, based on a nucleate pool boiling equation. Int J Heat Mass Transf 34(11):2759–2766

Lockhart R, Martinelli R (1949) Proposed correlation of data for isothermal two-phase, two-component flow in pipes. Chem Eng Prog 45(1):39–48

Mandhane J, Gregory G, Aziz K (1974) A flow pattern map for gas—liquid flow in horizontal pipes. Int J Multiphase Flow 1(4):537–553

Manglik RM (2006) On the advancements in boiling, two-phase flow heat transfer, and interfacial phenomena. J Heat Transf 128(12):1237–1242

Mchale JP, Garimella SV (2010) Bubble nucleation characteristics in pool boiling of a wetting liquid on smooth and rough surfaces. Int J Multiphase Flow 36(4):249–260

Mehendale S, Jacobi A, Shah R (2000) Fluid flow and heat transfer at micro-and meso-scales with application to heat exchanger design. Appl Mech Rev 53(7):175–193

Mogaji TS, Kanizawa FT, Bandarra Filho EP, Ribatski G (2013) Experimental study of the effect of twisted-tape inserts on flow boiling heat transfer enhancement and pressure drop penalty. Int J Refrig 36(2):504–515

Moser K, Webb R, Na B (1998) A new equivalent Reynolds number model for condensation in smooth tubes. J Heat Transf 120(2):410–417

Naik RR, Narain A (2016) Steady and unsteady simulations for annular internal condensing flows, part II: instability and flow regime transitions. Numer Heat Transf Part B Fundam:1–16

Naik RR, Narain A, Mitra S (2016) Steady and unsteady simulations for annular internal condensing flows, part I: algorithm and its accuracy. Numer Heat Transf Part B Fundam:1–22

Narain A, Kivisalu M, Naik R, Gorgitrattanagul N, Mitra S, Hasan MM (2012) Comparative experimental and computational studies for annular condensing and boiling flows in millimeter scale horizontal ducts. In: Proceedings of ASME 2012 summer heat transfer conference, Rio Grande, Puerto Rico. ASME

Narain A, Naik RR, Ravikumar S, Bhasme SS (2015) Fundamental assessments and new enabling proposals for heat transfer correlations and flow regime maps for shear driven condensers in the annular/stratified regime. J Therm Eng 1(4):307–321

Oh H-K, Son C-H (2011) Evaporation flow pattern and heat transfer of R-22 and R-134a in small diameter tubes. Heat Mass Transf 47(6):703–717

Park JE, Vakili-Farahani F, Consolini L, Thome JR (2011) Experimental study on condensation heat transfer in vertical minichannels for new refrigerant R1234ze (E) versus R134a and R236fa. Exp Thermal Fluid Sci 35(3):442–454

Phan HT, Caney N, Marty P, Colasson S, Gavillet J (2009) Surface wettability control by nanocoating: the effects on pool boiling heat transfer and nucleation mechanism. Int J Heat Mass Transf 52(23–24):5459–5471

Plesset M, Zwick SA (1954) The growth of vapor bubbles in superheated liquids. J Appl Phys 25(4):493–500

Prosperetti A, Plesset MS (1978) Vapour-bubble growth in a superheated liquid. J Fluid Mech 85(02):349–368

Qu W, Mudawar I (2004) Measurement and correlation of critical heat flux in two-phase microchannel heat sinks. Int J Heat Mass Transf 47(10–11):2045–2059

Raghupathi PA, Kandlikar SG (2016) Contact line region heat transfer mechanisms for an evaporating interface. Int J Heat Mass Transf 95:296–306

Ranga Prasad H, Narain A, Bhasme SS, Naik RR (2017) Shear-driven annular flow-boiling in millimeter-scale channels: direct numerical simulations for convective component of the overall heat transfer coefficient. Int J Transp Phenom 15(1):1–35

Ross H, Radermacher R (1987) Suppression of nucleate boiling of pure and mixed refrigerants in turbulent annular flow. Int J Multiphase Flow 13(6):759–772
Rouhani SZ, Axelsson E (1970) Calculation of void volume fraction in the subcooled and quality boiling regions. Int J Heat Mass Transf 13(2):383–393
Rykaczewski K, Paxson AT, Anand S, Chen X, Wang Z, Varanasi KK (2013) Multimode multidrop serial coalescence effects during condensation on hierarchical superhydrophobic surfaces. Langmuir 29(3):881–891
Saha SK, Celata GP (2016) Instability in flow boiling in microchannels. Springer, Cham
Sepahyar S (2018) Flow-boiling of water under innovative operations that lead to experimental realization of annular flows in millimeter scale ducts. Ph.D, Michigan Technological University.
Shah MM (1982) Chart correlation for saturated boiling heat transfer: equations and further study. ASHRAE Trans; (United States) 88 (CONF-820112-) 185–196
Shah MM (2015a) A general correlation for critical heat flux in horizontal channels. Int J Refrig 59:37–52
Shah MM (2015b) A method for predicting heat transfer during boiling of mixtures in plain tubes. Appl Therm Eng 89:812–821
Steiner D (1993) Heat transfer to boiling saturated liquids VDI-Wärmeatlas (VDI heat atlas). VDI-Gesellschaft Verfahrenstechnik und Chemieingenieurswesen (GCV), Düsseldorf
Steiner D, Taborek J (1992) Flow boiling heat transfer in vertical tubes correlated by an asymptotic model. Heat Transf Eng 13(2):43–69
Thome JR (2004) Engineering data book III. Wolverine Tube Inc, Huntsville
Tibiriçá CB, Ribatski G, Thome JR (2012) Saturated flow boiling heat transfer and critical heat flux in small horizontal flattened tubes. Int J Heat Mass Transf 55(25–26):7873–7883
Tolubinsky V, Kostanchuk D (1970) Vapour bubbles growth rate and heat transfer intensity at subcooled water boiling. In: International heat transfer conference 4. Begel House Inc
Tran T, Wambsganss M, France D (1996) Small circular-and rectangular-channel boiling with two refrigerants. Int J Multiphase Flow 22(3):485–498
Wang W-WW, Radcliff TD, Christensen RN (2002) A condensation heat transfer correlation for millimeter-scale tubing with flow regime transition. Exp Thermal Fluid Sci 26(5):473–485
Warrier GR, Dhir VK, Momoda LA (2002) Heat transfer and pressure drop in narrow rectangular channels. Exp Thermal Fluid Sci 26(1):53–64
White FM (2003) Fluid mechanics. McGraw-Hill, Boston
Wojtan L, Revellin R, Thome JR (2006) Investigation of saturated critical heat flux in a single, uniformly heated microchannel. Exp Thermal Fluid Sci 30(8):765–774
Wu Z, Wu Y, Sundén B, Li W (2013) Convective vaporization in micro-fin tubes of different geometries. Exp Thermal Fluid Sci 44:398–408
Yu W, France D, Wambsganss M, Hull J (2002) Two-phase pressure drop, boiling heat transfer, and critical heat flux to water in a small-diameter horizontal tube. Int J Multiphase Flow 28(6):927–941
Zeng L, Klausner J, Bernhard D, Mei R (1993a) A unified model for the prediction of bubble detachment diameters in boiling systems—II. Flow boiling. Int J Heat Mass Transf 36(9):2271–2279
Zeng LZ, Klausner JF, Mei R (1993b) A unified model for the prediction of bubble detachment diameters in boiling systems— I. Pool boiling. Int J Heat Mass Transf 36(9):2261–2270
Zhang W, Hibiki T, Mishima K, Mi Y (2006) Correlation of critical heat flux for flow boiling of water in mini-channels. Int J Heat Mass Transf 49(5–6):1058–1072
Zhu Y, Antao DS, Chu K-H, Chen S, Hendricks TJ, Zhang T, Wang EN (2016) Surface structure enhanced microchannel flow boiling. J Heat Transf 138(9):091501
Zivi S (1964) Estimation of steady-state void fraction by means of principle of minimum energy production. ASME J Heat Transf 86(2):247–252
Zuber N (1959) Hydrodynamic aspects of boiling heat transfer (thesis). California University, Los Angeles/Ramo-Wooldridge Corp., Los Angeles